Die approbierte Originalversion dieser Diplom-/Masterarbeit ist in der Hauptbibliothek der Technischen Universität Wien aufgestellt und zugänglich.
http://www.ub.tuwien.ac.at

TU UB WIEN Universitätsbibliothek

The approved original version of this diploma or master thesis is available at the main library of the Vienna University of Technology.
http://www.ub.tuwien.ac.at/eng

TECHNISCHE UNIVERSITÄT WIEN

DIPLOMARBEIT

# Characterization and Physical Modeling of Degradation in $MoS_2$ Transistors

ausgeführt zum Zwecke der Erlangung des akademischen Grades eines Diplom-Ingenieurs unter der Leitung von

Ao.Univ.Prof. Dipl.-Ing. Dr.techn. Tibor Grasser

E360 - Institut für Mikroelektronik

und der Assistenz von

Dipl.-Ing. Gerhard Rzepa

E360 - Institut für Mikroelektronik

eingereicht an der Technischen Universität Wien

Fakultät für Elektrotechnik und Informationstechnik

von

Theresia Knobloch BSc.

1125050 / E 066 508

Altmannsdorferstraße 182/69/7, 1230 Wien

Wien, Oktober 2016

# Zusammenfassung

In den letzten Jahrzehnten wurde das Moore'sche Gesetz durch die Verkleinerung der Dimensionen von Siliziumtransistoren aufrechterhalten. Diese Skalierung führte zu Gatelängen, die einigen dutzend Atomlagen entsprechen. Die weitere Skalierbarkeit stößt hier an eine natürliche Grenze, weshalb nun Konzepte für neue Bauelemente evaluiert werden müssen. Ein neuartiges Konzept basiert auf der Verwendung von zweidimensionalen Kanalmaterialien. Angetrieben von den vielversprechenden Eigenschaften des zweidimensionalen Materials Graphen, werden derzeit viele neue zweidimensionale Materialien erforscht, welche im Gegensatz zu Graphen eine Bandlücke besitzen. Allerdings ist die Zuverlässigkeit der meisten bisher untersuchten Bauelemente eher schlecht. Nach dem derzeitigen Verständnis entstehen die Zuverlässigkeitsprobleme nicht ausschließlich durch unausgereifte Fertigungsprozesse, sondern sind eine unveränderliche Materialeigenschaft und werden somit über Erfolg oder Misserfolg des Transistorkonzepts entscheiden.

Um die Zuverlässigkeit von Transistoren vorhersagen zu können, müssen die neuartigen Bauelemente und die auf ihnen beobachteten Degradationseffekte unter Verwendung physikalischer Modelle simuliert werden. In meiner Arbeit wurden die Theorien zur physikalischen Beschreibung der Degradation auf Transistoren basierend auf zweidimensionalen Schichten von Molybdän Disulfid ($MoS_2$) angewendet.

Die Hauptursache der Degradation ist die Wechselwirkung von Ladungsträgern mit Defekten im darunterliegenden Siliziumdioxid ($SiO_2$), die sowohl die Hysterese in der Transferkennlinie wie auch die beobachteten temperatur- und gatespannungsabhängigen Instabilitäten (BTI) verursacht. Die Messungen, welche diese Phänomene charakterisieren, können unter Verwendung eines nichtstrahlenden Multiphononenmodells mit vier Zuständen, welches Ladungseinfangs- und Ladungsemissionsereignisse im Oxid beschreibt, simuliert werden. Im Rahmen dieses Modells wurde ein neues Defektband extrahiert, welches über dem Defektband liegt, das die Degradation in konventionellen Transistoren bestimmt. Die Anordnung dieses Defektbands zu den Bandkanten von $MoS_2$ führt zu dem Schluss, dass nMOSFETs, die eine Einzellage $MoS_2$ als Kanalmaterial und $SiO_2$ als Gatedielektrikum verwenden, vermutlich immer unter einer Hysterese und großem negativen BTI leiden werden.

Nichtsdestotrotz zeigt diese Arbeit, dass etablierte, physikalische Modelle auf die neue Bauteilklasse anwendbar sind. Dadurch wird der Weg für zukünftige Studien geebnet, die zuverlässige zweidimensionalen Materialien identifizieren sollen.

# Abstract

Over the last decades Moore's Law was mainly maintained by scaling the dimensions of silicon transistors. This scaling led to gate lenghts corresponding to a few dozen layers of silicon atoms, hence it is approaching a hard limit. Therefore, new device concepts have to be evaluated. One novel concept is based on two-dimensional channel materials. This idea was strongly promoted by the two-dimensional material graphene. However, the application of graphene is limited due to its lack of a band gap. Other two dimensional materials were investigated and while there are promising materials which have a band gap it turned out that many of these transistors suffer from severe reliability issues. To the current understanding, these problems do not arise merely out of immature processing conditions but are inherent to the materials and might determine the success or the failure of new transistor concepts.

In order to be able to predict viable transistor technologies, the physical modeling of novel devices and their degradation mechanisms is essential. In this work the theoretical framework enabling a physical description of degradation effects was applied to transistors based on two-dimensional layers of Molybdenum Disulfide ($MoS_2$).

The material properties of transition metal dichalcogenides, the material class to which $MoS_2$ belongs, have to be known for modeling the transistor's characteristics using drift diffusion equations. Therefore, these properties are discussed in detail. At the current stage of device development, where the drain current is governed by scattering events, quantum mechanical effects can be neglected.

As a main source of degradation the interaction of charge carriers with defects in the underlying Silicon Dioxide ($SiO_2$) is identified. This causes a hysteresis in the transfer characteristics of the devices as well as the observed Bias Temperature Instabilities (BTI). The measurements characterizing these effects can be successfully simulated using the four-state nonradiative multiphonon model which describes charge capture and emission events in the oxide. In the framework of this model a new defect band, situated above the defect band governing the degradation effects in conventional transistors, was extracted. The alignment of this defect band to the band edges of $MoS_2$ leads to the conclusion that nMOSFETs, using a single layer of $MoS_2$ as a channel material and $SiO_2$ as a gate dielectric, will probably always suffer from hysteresis and large negative BTI.

Nevertheless, this works proves the applicability of established physics-based degradation models to the new device class. Thereby, it paves the way for future studies targeting at identifing reliable two-dimensional materials.

# Acknowledgments

First of all I want to thank Tibor Grasser for inspiring me with his lectures that arose my curiosity for the simulation of reliability issues. Then I want to thank him for his confidence in my skills and for his guidance over the course of this work. The strong collaboration has broadened my horizons.

My special thanks go to Gerhard Rzepa. Thank you for patiently introducing me to the world of professional device simulation. During numerous discussions, indispensable for solving the various problems arising in the course of this work, he substantially expanded my knowledge. Without his help this work would not have been possible and never could have reached the present level of perfection. The section about the four-state NMP model using Morse potentials is based entirely on his ideas.

I want to thank Yury Illarionov for measuring the characteristics of all devices. Thank you for reproducing the exact measurement history, vital to the interpretation of simulation settings, one year after the measurements were done.

Next, my thanks go to Marco M. Furchi, who produced the devices and who was always ready to answer detailed questions about the production process.

I have to thank my colleagues at the Institute of Microelectronics who helped with advice and enriched my views in discussions. Here my thanks go to Lukas Gnam, Markus Jech, Markus Kampl, Bernhard Stampfer and Yannick Wimmer.

I want to thank as well all my colleagues at the Institute of Sensor and Actuator Systems, especially Manuel Gillinger, who guided me through my first steps in the scientific world. I have learned a lot during my time under his supervision.

Finally my thanks go to my boyfriend Gerald, to my parents, to my sister Anna and to my friends, especially Nina and Nikoletta.
Thank you for your support over so many years.

# Contents


**1 Introduction** **1**
1.1 Motivation . . . 1
1.2 The Structure of this Work . . . 3

**2 Transition Metal Dichalcogenides** **5**
2.1 Atomistic Structure . . . 5
2.2 Synthesis . . . 6
2.2.1 Top-Down Methods . . . 6
2.2.2 Bottom-Up Methods . . . 8
2.3 Band Structure . . . 9
2.3.1 Experimental Analysis . . . 9
2.3.2 Density Functional Theory Calculations . . . 15
2.4 Carrier Mobility . . . 25
2.4.1 Electrons . . . 26
2.4.2 Holes . . . 26
2.5 Contacts . . . 27
2.6 Devices . . . 29

**3 Oxide Degradation** **33**
3.1 Atomistic Defect Structures . . . 33
3.1.1 Characterization of Single Defects . . . 34
3.1.2 Hydrogen Bridge . . . 35
3.1.3 Hydroxyl E' Center . . . 36
3.2 Hysteresis of Transfer Characteristics . . . 36
3.2.1 Measurement Setup . . . 39
3.3 Bias Temperature Instabilities . . . 40
3.3.1 Measure-Stress-Measure Technique . . . 40
3.3.2 On-the-Fly Measurement . . . 41
3.3.3 Capture-Emission-Time Map . . . 41
3.3.4 Measurement Setup . . . 42

**4 Modeling** **43**
4.1 Drift-Diffusion-Model . . . 43
4.2 Quantum Mechanical Corrections . . . 45
4.3 Interface States . . . 47
4.4 Oxide Defects . . . 50
4.4.1 Configuration Coordinate Diagram . . . 50
4.4.2 Morse Potential . . . 51
4.4.3 Problem Specification . . . 53
4.4.4 Single State Transitions . . . 54
4.4.5 Transitions for a Continuous Band of States . . . 56
4.4.6 Electron-Phonon Coupling Regimes . . . 57
4.4.7 Thermal Barriers . . . 59
4.4.8 Four-State NMP Model . . . 60
4.4.9 Charge Sheet Approximation . . . 65

**5 Results** **67**
5.1 Measurements . . . 67
5.2 Modeling of Transfer Characteristics . . . 69
5.3 Modeling of Hysteresis Measurements . . . 75
5.3.1 Effect of Interface States . . . 80
5.3.2 Oxide Defect Type . . . 85
5.3.3 Hysteresis Width . . . 87
5.4 Modeling of BTI Measurements . . . 88

**6 Conclusions** **93**
6.1 Outlook . . . 94

**A Data** **97**
A.1 Experimental Band Gaps . . . 97
A.2 DFT Band Gaps . . . 100
A.3 Effective Masses . . . 102

**Bibliography** **103**

# CHAPTER 1 Introduction

## 1.1 Motivation

Over the last 40 years silicon CMOS technology has become the most mature and well established technology in microelectronics. The rapid progress in this field can be described by Moore's Law, which was first mentioned in the 1960s as an ambitious prediction and has been embraced by the industry later on as the ultimate goal in order to ensure economic growth.

This so-called law states that the number of transistors on a given chip area doubles about every 18 months. In order to be able to achieve such an aggressive shrinkage the International Technology Roadmap for Semiconductors (ITRS) was created. In this document the world's specialists from industry and research outline the next steps which will have to be taken to further push the device performance to its limits. This way Moore's Law remained valid until today, leading us to a minimal gate length of around 10 nm. But already at gate lengths of around 100 nm so called Short Channel Effects (SCE), like Drain Induced Barrier Lowering (DIBL) or an increase in the sub threshold slope, limit device performance. Additionally, at such small dimensions (e.g. gate oxide thicknesses of around 1 nm) quantum mechanical effects like tunnelling are relevant. Due to the small dimensions of the devices existing defects in the amorphous gate oxide or at the interface have an increasingly greater impact on the device characteristics. Namely the variations in the device's parameters (=variability) and the degradation of the device parameters over time (=reliability) are more pronounced when considering small scale devices.

It is widely agreed that using only established technologies, device designs and materials, Moore's Law is at its end. Hence a paradigm shift in microelectronics where many new technologies are being evaluated as to whether or not they could be the solution to the above described problems, is currently taking place.

One promising new technology are MOSFETs with a two-dimensional channel material. A monolayer with atomic scale smoothness has no dangling bonds, therefore reducing the effect of surface roughness scattering, leading to a higher carrier mobility. In addition, the lower in-plane dielectric constants of common 2D materials lead to significantly reduced short channel effects compared to silicon [1].

The research concerning two-dimensional materials has boomed in the last decade, triggered by the discovery of the electric field effect in graphene by Novoselov et al. in 2004 [2]. Graphene devices show extremely high carrier mobilities up to $2 \times 10^5\,\mathrm{cm^2V^{-1}s^{-1}}$ [3] and cut-off frequencies higher than 100 GHz [4]. However, Graphene lacks a band gap, which leads to a very low current on/off ratio, making the usage in digital circuits impossible. Despite numerous attempts to induce a band gap to graphene by cutting it into nano ribbons or applying an electric field over a top gate, these methods all lead to a substantial performance decrease in all other respects [5, 6].

Therefore, the attention gradually shifted to other 2D materials possessing a band gap like Molybdenum Disulphide ($MoS_2$) for example, a member of the large group of Transition Metal Dichalcogenides (TMDs), or Phosphorene, the monolayered form of black phosphorous. In comparison to Graphene FETs, $MoS_2$ FETs exhibit a very high current on/off ratio [7] and a large transconductance [8], but only a mobility of $1000\,\mathrm{cm^2V^{-1}s^{-1}}$ at maximum [9]. Phosphorene, being one of the youngest members in the 2D material group, shows a mobility of up to $2700\,\mathrm{cm^2V^{-1}s^{-1}}$ [10] and has a band gap, thereby combining some of the best properties of graphene with those of $MoS_2$.

When talking about a transistor with a two-dimensional channel material, one has to bear in mind that due to the large surface to volume ratio, interaction of charge carriers with the surrounding media greatly affects the device performance. It has been shown that dielectric encapsulation enhances the device's performance [7] and that exactly this dielectric, on the other hand, leads to a reduction of the band gap due to dielectric screening [11]. It therefore only seems logical that also the interaction of charge carriers with defects at the interface or near the surface of the dielectric is more important in these 2D-based transistors than in conventional silicon technologies.

This is why in this work a study on the impact of defects at the interface and in silicon dioxide on the device characteristics of $MoS_2$ shall be presented based field effect transistors. The defects lead to a degradation of the device characteristics, which were studied using $I_\mathrm{D}\,(V_\mathrm{G})$ curve measurements showing a hysteresis as well as special measurement techniques already established for determining the reliability of conventional silicon FETs (the so called Bias Temperature Instabilities (BTI) measurements). The device characteristics were simulated using the drift diffusion model, in order to get a better understanding of the defects' amount, distribution and energetic properties. The successful modeling of device characteristics is also an important step enabling Technology Computer Aided Design (TCAD), which is common standard in today's semiconductor technology.

At this point it shall be emphasized that even if transistors based on 2D materials are still in an early stage, investigations of the device's reliability are of utmost importance. The observed degradation effects do not arise from an immature fabrication process, but are inherent to a given material system. And what is more, the energetic alignment of the defect states determining the interaction of the charge carriers with the defects is given by the nature of these defects, being for example a vacancy at a certain lattice site. This makes the energetic alignment a fixed property of a certain combination channel material to dielectric.

However, by using a clever alignment of the respective energies it might be possible to

create a system, where the charge carriers do not interact with the surrounding defects, making this system nearly perfectly reliable. Pursuing such a high goal, this work wants to make a small step towards a better understanding of the interaction of defects in the surroundings with the charge carriers in the two-dimensional channel and provide insights into how reliably this special system of an $MoS_2$ channel on a $SiO_2$ dielectric can perform.

## 1.2 The Structure of this Work

In the second chapter the general material properties of TMDs are discussed with a focus on $MoS_2$. Additionally, the device geometry used for the present study is described in detail.

In the third chapter atomistic defect models for defects in silicon dioxide are presented and the measurement procedures used for analysing degradation processes are introduced. This chapter is followed by a discussion of the simulation methodology in chapter four. In this chapter the applicability of the drift diffusion model to two dimensional devices is considered and then models, necessary to describe the degradation of such devices due to defects at the interface and in the dielectric, are introduced.

Chapter five starts with a description of the measurements which were carried out on the devices. Then the simulation results for simple $I_{\mathrm{D}}\left(V_{\mathrm{G}}\right)$ characteristics are given and are followed by detailed simulation results of degradational effects observed on $MoS_2$ transistors. The work is concluded by a short reflection on the implications of this work as well as an outlook to further investigations.

# CHAPTER 2 Transition Metal Dichalcogenides

TMDs are a class of materials with the chemical formula $MX_2$, where M is a transition metal element and X a chalcogen (S, Se, Te). Usually the transition metal elements are located either in side group IV (Ti, Zr, Hf), V (V, Nb, Ta) or VI (Cr, Mo, W). Here the material properties of TMDs are discussed with a special focus on two-dimensional phases. The fabrication of 2D layers uses special techniques which will be introduced. When reducing the thickness of a material in one dimension substantially, the quantum confinement and the increased surface- to volume ratio lead to completely different material properties than observed in the well- known bulk forms. Therefore, a detailed study concerning the emerging variations in material properties due to the lower dimensionality is necessary. What is more, a precise knowledge about these properties will prove essential for a correct modeling of the devices. At the end of this chapter the most common transistor geometries will be discussed, together with recent results from other groups, and finally the production process and exact measures of the devices, which were analyzed by experiment and simulation in this work, will be given.

## 2.1 Atomistic Structure

TMDs show layered structures, where two planes of chalcogen atoms are separated by one plane of metal atoms, as it is illustrated in Figure 2.1. The bonds within every layer are covalent. In the bulk form adjacent layers are weakly held together by Van der Waals forces.

Different phases are distinguished depending on the stacking order and the symmetry of the monolayer, shown in Figures 2.2(a) and 2.2(b). In the 2H phase, the crystal possesses a hexagonal symmetry and the metal atoms have a trigonal prismatic coordination, whereas in the 1T phase, the crystal has only tetragonal symmetry and the metal atoms show an octahedral coordination. In order to better understand the difference between hexagonal and tetragonal symmetry in a monolayer the top view on monolayers with different symmetry is given in Figure 2.2(c) [12].

At room temperature only the 2H phase is thermodynamically stable [13]. Only this phase exhibits good optoelectronic properties such as semiconducting behaviour or photoluminescence [14].

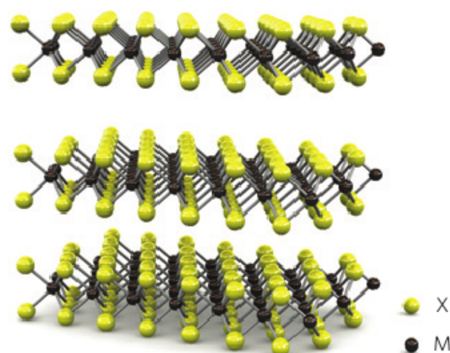


Figure 2.1: The layered structure of TMDs. Yellow dots represent chalcogen atoms and black dots metal atoms. [12]

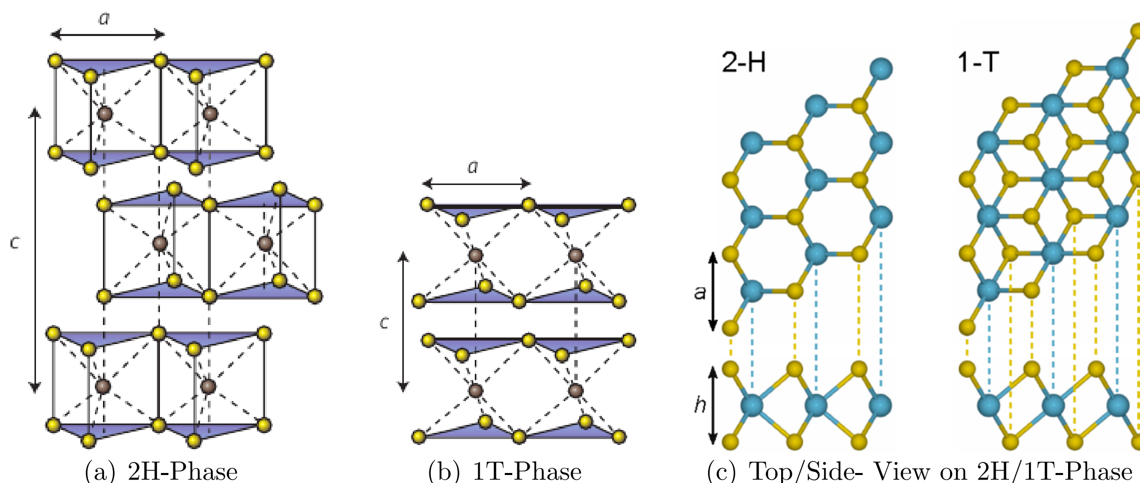


(a) 2H-Phase (b) 1T-Phase (c) Top/Side- View on 2H/1T-Phase

Figure 2.2: Structural Polytypes. Yellow dots represent chalcogen atoms and black/blue dots metal atoms. The letters a and c denote the lattice constants of the crystal and h the thickness of a monolayer. [12, 13]

## 2.2 Synthesis

### 2.2.1 Top-Down Methods

The most common deposition technique for two-dimensional layers is mechanical exfoliation, which has been developed for graphene. Here atomically thin flakes are micromechanically cleaved from their parent bulk crystal using adhesive tape. In the next step

these flakes are applied to substrates and are optically identified using light interference. Benameur et al. [15] showed that for the system of a $MoS_2$ monolayer on a $SiO_2$ layer grown on a silicon wafer, a silicon oxide thickness of 90 nm or 270 nm is necessary to obtain a good optical contrast in the light microscope. In Figure 2.3 a microscope image of an $MoS_2$ monolayer on $SiO_2$ is given.

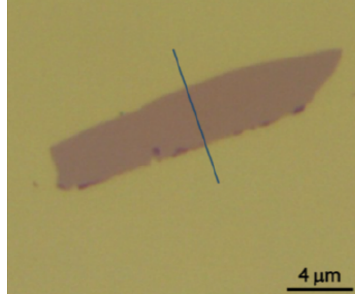


Figure 2.3: Optical microscope image of a single layer $MoS_2$. [15]

Mechanical exfoliation produces very clean and pure monolayers, which are suitable for characterization of fundamental material properties and for fabrication of single devices. Using this method only flakes of a limited size in the micrometer range can be obtained, which are distributed arbitrarily and have to be qualified one by one. Furthermore, this method suffers from a low yield and is thus not suitable for batch processing.

In liquid exfoliation, being quite similar to mechanical exfoliation, two main process types are distinguished. The first one is the so called ionic intercalation, where a powder of the bulk material is dispersed in a solvent containing a suitable intercalant, for example n-butyllithium. In this case lithium atoms are included into the crystalline structure between the layers which decrease the interlayer binding firstly by an increase of the layer spacing and secondly by a transfer of charges onto the layers. The delamination process is finished either by a $H_2$ gas forming reaction of lithium with water, thermal shock or ultrasonication [12, 16].

Using this process one obtains gram quantities of few-layered flakes dispersed in liquid, the monolayer gain for this special technique is as high as 92% [17]. Lithium intercalation changes the electronic structure of the monolayers from the semiconducting 2H-phase to the metallic 1T-phase. Therefore, a thermally induced phase transition from 1T to 2H-phase is necessary in order to restore the optoelectronic properties [14].

The second type of liquid exfoliation uses ultrasonication in a suitable solvent, which has a surface energy similar to that of the layered material. In this case the energy difference between exfoliated and re-aggregated layers is minimized, removing the driving force for re-aggregation [12, 16]. With this technique an even higher concentration of few-layered flakes dispersed in liquids is obtained, but the monolayer gain is substantially lower.

The main drawbacks for all top-down methods are that before device fabrication can start an optical qualification of the produced layers is necessary and that the available flake size is limited. Therefore, for industrial production of devices on a large scale with high yield, the development of bottom-up methods is indispensable.

### 2.2.2 Bottom-Up Methods

Using bottom-up technologies in principle arbitrarily large samples can be produced, but contrary to top down methods the obtained samples are usually not monocrystalline but possess grain boundaries, limiting carrier transport through scattering. Thus in evaluating bottom up methods one has to keep the focus on the obtained crystal quality and grain size.

At present the most common bottom-up method is chemical vapour deposition (CVD). The trioxide of the transition metal (for example $MoO_3$) in powder form or as a nanoribbon and sulphur powder placed upstream in the CVD reactor are used as precursors. Then, under pure nitrogen flow at ambient pressure the reactor is heated up to processing temperature and the sulphur sublimates. The processing temperature varies in literature between 650 °C[18] and 850 °C[19]. The sulphur vapour reduces the $MoO_3$ powder to the off-stoichiometric compound $MoO_{3-x}$ which is volatile and diffuses towards the substrate where it reacts with sulphur to form $MoS_2$ crystals. Usually an $SiO_2$ layer on a silicon wafer is used as a substrate . The nucleation starts at arbitrarily distributed sites and continues in triangular shaped form. These triangles are single crystalline monolayers.

The number of nucleation sites and the size of the triangles depend critically on the processing conditions. The nucleation can be guided to specified locations by prepatterning of the $SiO_2$ surface[19] or by using special seed molecules [18]. Both methods lead to a decreased grain size but guiding the nucleation will probably be necessary for industrial-scale device fabrication. Van der Zande et al. [20] showed that under ideal processing conditions, triangles with side lengths of up to 123 µm can be obtained. The optical micrograph and the transmission electron microscope (TEM) image, together with the diffraction pattern proving the single crystallinity of a flake, are shown in Figure 2.4. The overall amount of deposited $MoS_2$ is controlled by the amount of $MoO_3$ available, which acts as a limiting reagent. Transistors have been fabricated by patterning of obtained triangular monolayers by Amani et al. [21] demonstrating a mobility of $\mu = 6\,\mathrm{cm^2/Vs}$ in a back-gate architecture using Ti/Au contacts.

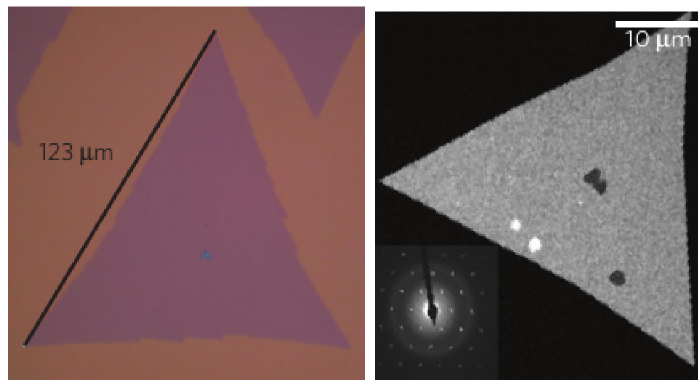


(a) Optical microscope image. (b) TEM image.

Figure 2.4: Triangular single crystalline $MoS_2$ monolayers grown with CVD. [20]

Another promising bottom up technology is the sulphurization of metal films. An extremely thin metal film (for example Mo), with thicknesses varying between 0.2 nm and 0.5 nm[22], is evaporated onto the $SiO_2$ layer on silicon. In the next step the samples are annealed in a furnace at 800 °C under $H_2S$ gas flow, where the metal films react and form a layered TMD. The resulting thickness of the TMD depends on the initial thickness of the metal film. The above-given range of metal layer thicknesses correspond to 2-4 monolayers in the final crystal. The biggest problem with this technique is the reported small grain size of a few tens of nanometers [23]. The grain size can be increased by performing a second annealing step under a $H_2S$ atmosphere at 1000 °C leading to a grain size of 100 nm. A back-gated transistor with Mo/Au contacts fabricated from these layers obtained a mobility of $\mu = 3\,\mathrm{cm}^2/\mathrm{Vs}$ [22].

## 2.3 Band Structure

The band structure is one of the most important properties of a solid material. It is the electronic structure of the crystal, which defines the interaction with photons as well as the interaction with defects in surrounding materials. A detailed study of the band structure is necessary in order to interpret and simulate measurements. Several experiments can reveal parts of the electronic structure, like band gaps or band alignments between different materials, but only ab initio calculations using density functional theory (DFT) can give the whole picture. Even if the focus lies on single-layer $MoS_2$, data will be given for different TMDs for varying numbers of layers to illustrate the most important trends and to obtain reference values after which DFT results can be judged.

### 2.3.1 Experimental Analysis

Due to the reduced screening in two-dimensional materials, electron-electron interactions are much stronger than in bulk materials, leading to the existence of tightly bound excitons and trions. [24, 25, 11, 26, 27] Excitons are neutral quasiparticles consisting of an electron and a hole bound together and trions consist of two holes and one electron or two electrons and one hole therefore being charged quasiparticles.

When performing for example a photoluminescence (PL) measurement one excites an electron by interaction with photons. The electron is removed from its place in the crystal lattice, leaving behind a positively charged hole. Due to the reduced dielectric screening in a two-dimensional structure, the electron is not yet completely free, but remains over the Coulomb interaction bound to its respective hole. To separate the electron completely from its former lattice site more energy has to be provided, namely the excitonic binding energy $E_{\mathrm{EXC}}$. However, in a PL experiment no more energy is available after the first excitation with a laser pulse. Therefore, in such experiments the electrons will never separate completely from the holes, but remain in the excitonic state until this state decays under radiation of light. The wavelength of the emitted light corresponds to the optical band gap $E_{\mathrm{OPT}}$.

These simple considerations give a first hint, what has to be taken into account when comparing experimental results from different groups.

It is clear that different band gaps will be measured for different TMDs, but one also has to distinguish between measurements for different numbers of layers. In monolayers the described excitonic effects are very strong, when regarding bilayers, trilayers or multilayers in general, the excitonic binding energy gradually declines with increasing number of layers until it becomes negligible in bulk material [28, 29].

Therefore, when regarding a nearly two-dimensional structure, one has to differentiate which quantity is being measured. PL measurements for example give the value of the optical band gap $E_{\mathrm{OPT}}$. Scanning tunneling spectroscopy (STS) measurements can be used to determine the electronic band gap $E_{\mathrm{G}}$. The electronic band gap corresponds to the energy needed to separate an electron completely from a hole. Only if the bias voltage provides enough energy to separately tunnel an electron and a hole into the monolayer, there is a substantial tunneling current [11]. The excitonic binding energy $E_{\mathrm{EXC}}$ is given by the difference of the optical and the electronic band gap,

$$E_{\mathrm{EXC}} = E_{\mathrm{G}} - E_{\mathrm{OPT}}. \tag{2.1}$$

It has been shown that by increasing the number of layers, the electronic band gap and the excitonic binding energy gradually decreases, whereas the optical band gap roughly remains the same [28]. The excitonic binding energy decreases due to the enhanced dielectric screening by the surrounding material and the electronic band gap decreases due to the reduced interaction of free electrons and holes with surface charges [30, 28]. As these two effects have the same root cause, namely the dimensionality of the system, they cancel each other out when increasing the number of layers, leading to a constant optical band gap.

Another possibility to enhance dielectric screening and to reduce the interaction of electrons with the surface polarization is to change the dielectric environment of the sample. A monolayer which is not suspended but which lies on top of a dielectric, like for example $SiO_2$, does not behave like a monolayer in vacuum but has a reduced band gap, as the dielectric environment provides additional screening. The dielectric constant can be used to roughly estimate whether the influence of the dielectric on the band structure of the monolayer is large (in case of a large dielectric constant) or small. Therefore, when comparing band gap measurements for different two-dimensional materials, one always has to take the dielectric surroundings of the sample into account [28, 11].

In Figure 2.5 the different alignments of the excitonic state A to the ground state and the conduction band are shown schematically for the system of a $MoSe_2$ monolayer on a bilayer graphene substrate. The results for DFT calculations, with and without the inclusion of the graphene substrate, are shown together with experimental results from PL and STS measurements [11].

Furthermore, the four most common TMDs, $MoS_2$, $MoSe_2$, $WS_2$ and $WSe_2$, show a transition from a direct to an indirect semiconductor when more than one layer of the material is stacked over each other, obtaining a multilayer structure [31, 32, 33]. This is

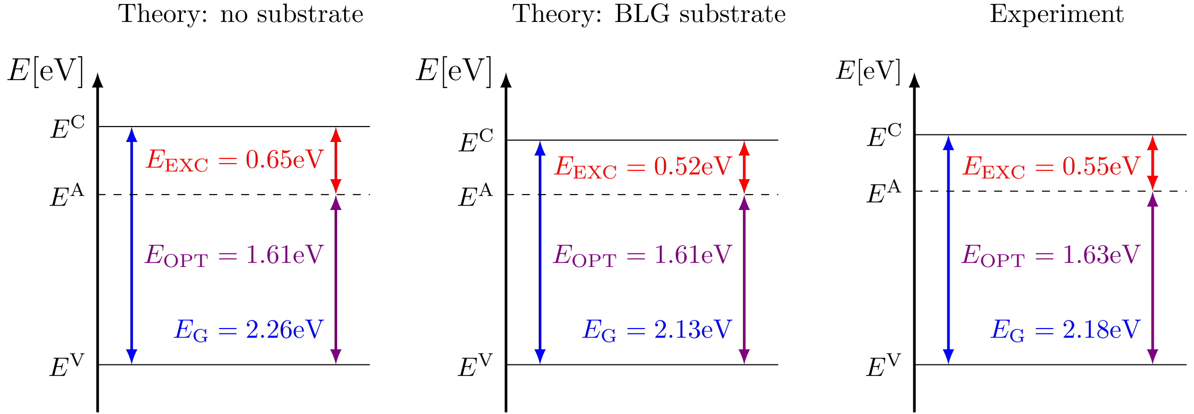


Figure 2.5: Schematic drawing of the band gap of monolayer $MoSe_2$ on Bilayer Graphene (BLG). $E_A$ denotes the excitonic state. (adapted from [11])

why the intensity of the PL peak in monolayer $MoS_2$ is by several decades larger than in multilayer $MoS_2$ [31]. The indirect to direct semiconductor transition was attributed by Han et al. [34] to Van der Waals interactions between adjacent layers, suggesting that such a transition can also result from combining a monolayer with another material in a heterostructure. The band structures of heterobilayers, consisting of two different TMD monolayers stacked on each other, were studied by Debbichi et al. [35] proving that direct as well as indirect semiconductors can be formed depending on the participating materials. For multilayer TMDs one has to distinguish between measurements of the direct and of the indirect band gap.

Additionally, when analysing the band structure of multilayer TMDs, different stacking orders of subsequent layers lead to different band gaps [36].

As for all semiconductors, also for TMDs the band gaps are temperature dependent. The temperature dependence of the optical band gap in monolayer $MoS_2$ as well as $MoSe_2$ was studied using PL measurements [37, 32]. The dependence was then fitted to the semi-empirical formula of O'Donnel [38] (Equation (2.2)). Here ${E_{\mathrm{OPT}}}^0$ stands for the optical band gap at 0 K, $\langle\hbar\omega\rangle$ for the average acoustic phonon energy and $S$ is an electron-phonon coupling parameter.

$$E_{\mathrm{OPT}} = E^0_{\mathrm{OPT}} - S\langle\hbar\omega\rangle\left[\coth\left(\langle\hbar\omega\rangle/2k_BT\right) - 1\right] \tag{2.2}$$

It is well known that strain can be used to tune the electric properties of materials. This is especially important for two-dimensional materials, which can sustain large tensile strain. By applying strain, the in-plane orbital interactions are changed, which leads to a transition from a direct to an indirect semiconductor for monolayer TMDs and to large changes in the band gap for multilayer TMDs [39, 40].

Before thoroughly analysing the available experimental data for the band structure of TMDs, in Figure 2.6 a schematic shall illustrate the factors influencing the value of the band gap. For a specific material with a defined number of layers $N$ at a given

temperature $T$, one obtains an indirect semiconductor if $N > 1$ and a direct semiconductor otherwise. For multilayer TMDs with $N > 1$ additionally the stacking order of subsequent layers affects the band gap. If $N \lesssim 10$ one can say that the material shows a significantly smaller extension in one dimension and can therefore be termed two-dimensional material. In this case there will be strongly bound excitons, and the dielectric environment of the sample will influence the band gap just as any applied strain, which can be especially large for two-dimensional materials.

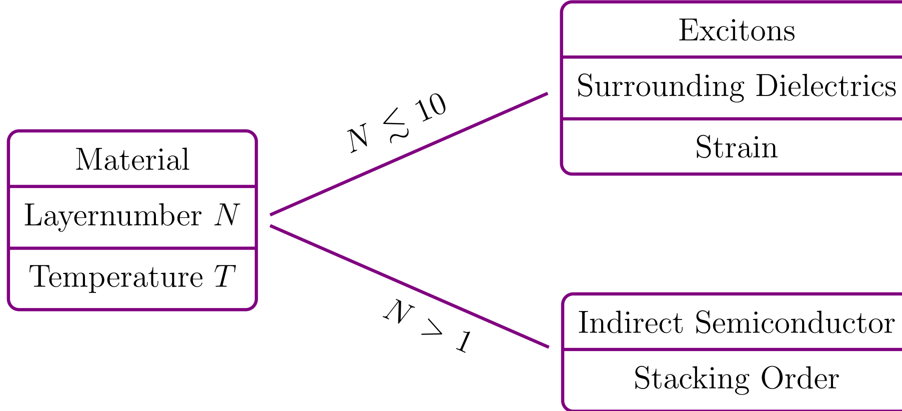


Figure 2.6: Schematic illustrating the dependencies of the band gap. In any case the band gap depends on the material, the number of layers $N$ and on the temperature $T$. To decide which additional dependencies add to these three obvious ones, the number of layer serves as a criterion. If the number of layers $N$ is larger than one, the semiconductor becomes indirect, hence it becomes necessary to distinguish between the values for the direct and the indirect bandgap and the stacking order influences the band gap as well. For systems consisting of only few layers the excitonic effects are strong, thereby one has to distinguish between the electronic and excitonic band gap and the band gaps can be influenced by surrounding dielectrics and strain.

Thus when considering a monolayer, the band gap depends on the respective material and the temperature. Additionally, one has to consider excitonic effects, the surrounding dielectrics and an eventual strain inside the layer. On the other hand when considering bulk material, the band gap depends on the material, the temperature and the stacking order. Additionally, one has to distinguish between direct and indirect band gap. If regarding a bilayered material all dependencies become important - the material, the temperature, excitonic effects, surrounding dielectrics, strain, indirect/ direct band gap and the stacking order.

The Figure 2.6 can also be seen in a more general context as most of the given dependencies apply to all two-dimensional materials. The transition from an indirect to a direct semiconductor at $N = 1$ is a speciality of TMDs, but the dependency of the band structure on excitonic effects, surrounding dielectrics and strain, is the same for all two-dimensional materials and in multilayer stacks one always gets the stacking order as an additional parameter.

In Table 2.1 the available experimental data for the electronic band gap $E_\mathrm{G}$, the optical band gap $E_\mathrm{OPT}$ and the excitonic binding energy $E_\mathrm{EXC}$ for $MoS_2$ monolayers on different substrates are shown. The employed measurement technique is given in brackets behind the respective values. Hereby “Abs.” stands for absorption measurement and “PS” stands for photocurrent spectroscopy, where the current through the monolayer is measured as a function of the wavelength of the exciting laser light.

Looking at Table 2.1 it can be seen that the optical band gap is not affected by the substrate and lies at approximately 1.9 eV.

As expected the electronic band gap and the excitonic binding energy are influenced by the substrate. The similar values for the electronic gap on $SiO_2$ and highly oriented pyrolytic graphite (HOPG) are surprising, as the dielectric constants of the two materials are very different. Therefore, further verification of the measurement data of Hill et al. [41] is certainly needed. From their data it looks like monolayer $MoS_2$ on silicon has an electronic bandgap of around 2.2 eV leading to an excitonic binding energy of roughly 0.3 eV.

The data given in Table 2.1 is only valid at T = 77K. Tongay et al. [32] extracted the necessary fitting constants for the use of Equation (2.2) by analysing PL measurements at different temperatures and obtained $\langle \hbar\omega \rangle = 22.5\,\mathrm{meV}$ and $S = 1.82$. Using these parameters the optical band gaps at $T = 77\,\mathrm{K}$ and at $T = 293\,\mathrm{K}$ differ by 0.05 eV. This value is probably smaller than the actual measurement accuracy, as can be seen by the deviations in the optical band gap measured by different groups. For this reason and because there are, to my knowledge, no studies about the temperature dependence of the electronic band gap or the excitonic binding energy, the temperature dependence of the band gap is neglected further on.

Several groups [39, 42] studied the impact of strain on the band structure of monolayer $MoS_2$ and showed that per percent of applied strain the optical band gap is reduced by around 0.06 eV (0.07 eV [39], 0.05 eV [42]). After exfoliation the monolayer is usually not stressed which is why the impact of strain on the band gap shall be neglected.

Similar tables as Table 2.1 for monolayer $MoSe_2$ (Table A.1), $WS_2$ (Table A.2) and $WSe_2$ (Table A.3) can be found in Appendix A.1.

In Table 2.2 the direct and indirect optical band gaps for multilayer $MoS_2$ are given. Especially for bi- or trilayers, there probably is an excitonic state with non-negligible binding energy. Nevertheless, up to date there are, to my knowledge, no measurements of the electronic gap in multilayer $MoS_2$. Therefore, only the data for the optical band gap can be compared. Furthermore, the band gap depends on the stacking order of subsequent layers. In the references, where no information about the relative alignment of the two layers is given, it is assumed that the 2H-phase of bulk $MoS_2$ was investigated, as this is the most abundant form. From the work of Van der Zande et al. it can be seen that the direct band gap is not affected by changing the relative alignment of $MoS_2$ bilayers whereas the indirect band gap varies between 1.4 eV and 1.6 eV. In the table, the value corresponding to the 2H-phase is given to obtain comparability to the other values.

The direct optical band gap barely changes with an increasing number of layers. There seems to be a small decline from 1.9 eV for a monolayer to 1.85 eV for bulk material,

| Substrate | Source | $E_G$ | $E_{OPT}$ | $E_{EXC}$ |
|---|---|---|---|---|
| HOPG ($\epsilon_r \approx 11$ [43]) | [27] | 2.15(6) eV (STS) | 1.93 eV (PL) | 0.22(10) eV |
| | [44] | 2.15(10) eV (STS) | - | - |
| suspended ($\epsilon_r = 1$) | [26] | 2.5 eV (PS) | 1.9 eV (PS) | 0.6 eV |
| $SiO_2$ ($\epsilon_r \approx 3.9$) | [41] | 2.19(5) eV (STS) | - | - |
| | [31] | - | 1.88 eV$^\star$ (PL, Abs.) | - |
| | [45] | - | 1.85 eV$^\star$ (PL, Abs.) | - |
| | [32] | - | 1.86 eV (PL) | - |
| | [25] | - | 1.92 eV (Abs.) | - |
| SU8 ($\epsilon_r \approx 3.0$) | [42] | - | 1.82(2) eV$^\star$ (PL) | - |
| PMMA ($\epsilon_r \approx 3.6$) | [39] | - | 1.9 eV$^\star$ (PL) | - |

Table 2.1: Experimentally obtained values for the band gap in single layer $MoS_2$. (HOPG: highly oriented pyrolytic graphite, SU8: a photoresist, PMMA: polymethylmethacrylate) $T = 77$ K for all measurements except for those marked with $^\star$, where $T = 293$ K.

| $N$ | Substrate | Source | $E_{OPT}{}^{d}$ | $E_{OPT}{}^{i}$ |
|---|---|---|---|---|
| 2 | $SiO_2$ | [36] | 1.84 eV (PL) | 1.42 eV (PL) |
| | | [31] | 1.87 eV (PL) | 1.6 eV (PL) |
| 2 | suspended | [26] | 1.87 eV (PS) | - |
| 2 | SU8 | [42] | 1.81(2) eV (PL) | 1.53(3) eV (PL) |
| 2 | PMMA | [39] | 1.9 eV (PL) | 1.55 eV (PL) |
| 3 | $SiO_2$ | [31] | 1.87 eV (PL) | 1.45 eV (PL) |
| 6 | $SiO_2$ | [31] | 1.85 eV (PL) | 1.4 eV (PL) |
| 50 | glass | [26] | 1.85 eV (PS) | - |
| bulk | - | [46] | 1.74 eV (PS) | 1.23 eV (PS) |

Table 2.2: Experimentally obtained values for the band gap in multilayer $MoS_2$.

which is close to the measurement accuracy. The indirect optical band gap on the other hand, declines with an increasing number of layers.

Again, a similar table as Table 2.1 for multilayer $MoSe_2$ (Table A.4) can be found in Appendix A.1.

At least as important as the band gap is the relative alignment of bands between different materials. In general for a semiconductor this alignment is given by the electron affinity $\chi$, which is defined as the difference between the vacuum level $E_{\mathrm{VAC}}$ and the conduction band edge $E_{\mathrm{C}}$. This quantity is not directly accessible to measurements, only the relative alignment of bands of different materials can be measured.

In Table A.5 in the Appendix A.1 experimentally obtained band offsets for different material combinations are listed. Only a small fraction of the relative band alignments has been measured up to now. Still, this data can be used to assess the accuracy of a complete DFT calculation.

### 2.3.2 Density Functional Theory Calculations

DFT calculations are so called ab-initio calculations where several material properties like lattice constants, binding energies and band structures are obtained by an approximative solution of the Schrödinger equation for a system of atoms.

#### Theoretical Foundations

At first the Born-Oppenheimer approximation is applied, where one defines separate Schrödinger equations for electrons and for nuclei, assuming that electrons move so much faster than nuclei that they can adjust instantaneously to new core positions. The electrons move in a potential specified by the current location of all nuclei, whereas the movement of the nuclei evolves on a multidimensional potential energy surface defined by the average electron positions. As the band structure is defined by the electrons, one now focuses on the solution of the electronic Schrödinger equation (Equations (2.3), (2.4)). Here $\hat{T}_{\mathrm{el}}$ stands for the kinetic energy of the electrons, $\hat{V}_{\mathrm{el-el}}$ for the coulomb repulsion potential between electrons and $\hat{V}_{\mathrm{el-nuc}}$ for the coulomb attraction potential between electrons and nuclei [47].

$$\hat{H}_{\mathrm{el}}\, \psi_{\mathrm{el},i}\,(\mathbf{r},\mathbf{R}) = E_{\mathrm{el},i}(\mathbf{R})\, \psi_{\mathrm{el},i}\,(\mathbf{r},\mathbf{R}) \tag{2.3}$$

$$\hat{H}_{\mathrm{el}} = \hat{T}_{\mathrm{el}} + \hat{V}_{\mathrm{el-el}} + \hat{V}_{\mathrm{el-nuc}} \tag{2.4}$$

In a next step the Hohenberg-Kohn theorem is applied to separate the above equation for $N$ electrons into $N$ separate equations, one for each electron. The Hohenberg-Kohn theorem (Equation (2.5)) provides the foundation for DFT calculations, stating that the correct ground state electron density $n_0$ minimizes the energy functional $E[n]$, which gives the energy of the whole system as a function of the electron density. Thus one obtains the ground state energy $E_{tot}$ [48].

$$E_{\mathrm{tot}} = \min_{n(\mathbf{r})} E[n] = \min_{n(\mathbf{r})} \left(T[n] + V_{\mathrm{ext}}[n] + V_{\mathrm{H}}[n] + E_{\mathrm{xc}}[n]\right) \tag{2.5}$$

Here $T[n]$ stands for the total kinetic energy of the system, $V_{\mathrm{ext}}[n]$ stands for the external potential energy due to the Coulomb interaction of the electrons with the nuclei, $V_{\mathrm{H}}[n]$, the so called Hartree energy, gives the potential energy due to the Coulomb repulsion of all electrons and finally the exchange energy $E_{\mathrm{xc}}[n]$ accounts for all quantum- mechanical many body-effects. As some of the above given energy functionals are not well known, one applies a variational principle to obtain the single particle equations, the so called Kohn-Sham equations [49].

$$\left(-\frac{\hbar^2}{2m_0}\nabla^2 + v_{\mathrm{ext}}(\mathbf{r}) + v_{\mathrm{H}}(\mathbf{r}) + v_{\mathrm{xc}}(\mathbf{r})\right)\psi_i(\mathbf{r}) = \epsilon_i \psi_i(\mathbf{r}) \tag{2.6}$$

So, finally the problem reduces to correctly calculating the effective potential, consisting of external potential $v_{\mathrm{ext}}(\mathbf{r})$, Hartree potential $v_{\mathrm{H}}(\mathbf{r})$ and exchange potential $v_{\mathrm{xc}}(\mathbf{r})$. Here $q$ stands for the elementary charge, carried by one electron.

$$v_{\mathrm{ext}}(\mathbf{r}) = -\sum_{j=1}^{N_{\mathrm{K}}} \frac{q^2 Z_j}{|\mathbf{r} - \mathbf{R}_j|} \tag{2.7}$$

$$v_{\mathrm{H}}(\mathbf{r}) = \int \mathrm{d}^3 r'\, n(\mathbf{r}') \frac{q^2}{|\mathbf{r} - \mathbf{r}'|} \tag{2.8}$$

$$v_{\mathrm{xc}}(\mathbf{r}) = \frac{\delta E_{\mathrm{xc}}[n]}{\delta n} \tag{2.9}$$

Still, at this point the non-local exchange correlation functional $E_{\mathrm{xc}}[n]$ is unknown. Several approximations exist for calculating this functional. The easiest is the local density approximation (LDA), where the exchange correlation energy is calculated for a homogeneously distributed electron gas. Thus, the exchange correlation energy is assumed to be the same at every point in space [50]. LDA has been surprisingly successful but is also known to show over-binding, overestimating all binding energies. One step towards an improvement of this approximation is the generalized gradient approximation (GGA). In this approximation the exchange-correlation energy, does not only depend on the local electron density but also on the gradient of the electron density. This way some information about the surrounding of a point in space is included into the calculation of the exchange energy as well. The most common functional used in the GGA is the Perdew-Burke-Ernzerhof functional (PBE) [51].

When performing a DFT calculation, one either decides on the usage of a LDA or a PBE functional, solves in this way Equation (2.6) and, finally, obtains Kohn-Sham eigenvalues $\epsilon_i$, which give the ground state energy.

$$E_{\mathrm{tot}} = \sum_{i=1}^{N} \epsilon_i + E_{\mathrm{xc}}[n] - \int \mathrm{d}^3 r\, v_{\mathrm{xc}}(\mathbf{r}) n(\mathbf{r}) - V_H. \tag{2.10}$$

The second and the third summand of Equation (2.10) account for variations in the exchange correlation potential and the fourth term is the so called Hartree potential

(Equation (2.11)), which has to be subtracted so that no Coulomb interaction between the same electron is taken into account.

$$V_{\mathrm{H}} = \frac{1}{2}\int \mathrm{d}^3r\mathrm{d}^3r'\, n(\mathbf{r}')n(\mathbf{r})\frac{q^2}{|\mathbf{r}-\mathbf{r}'|} \tag{2.11}$$

One has to be extremely cautious, when interpreting the results of Equation (2.10). The ground state energy of the whole system $E_{\mathrm{tot}}$ is exactly calculated, but the Kohn-Sham eigenvalues $\epsilon_i$, even though often interpreted as single particle energies, actually have no physical meaning. So even if the eigenvalues $\epsilon_i$ can be used to obtain a good guess of the band gap and the band structure in some materials, they might give completely wrong results for others [47]. Especially for compounds of transition metals, which are studied here, the band gaps calculated using the Kohn-Sham eigenvalues underestimate the real band gap by approximately 30%[52].

A proper way for calculating quasiparticle energies is the Green function theory. In this theory it was shown that exact quasiparticle energies $E_i$ can be obtained by solving the quasiparticle equation. (Equation (2.12))[53]

$$\left(-\frac{\hbar^2}{2m_0}\nabla^2 + v_{\mathrm{ext}}(\mathbf{r}) + v_{\mathrm{H}}(\mathbf{r})\right)\psi_i(\mathbf{r}) + \int \mathrm{d}^3r'\,\Sigma(\mathbf{r},\mathbf{r}';E_i)\,\psi_i(\mathbf{r}') = E_i\psi_i(\mathbf{r}) \tag{2.12}$$

This equation is similar to Equation (2.6) with the exception that instead of the exchange potential one adds the integral over the non-local and energy-dependent potential $\Sigma$, usually called self-energy. The self-energy contains all exchange and correlation effects and is in general extremely complex. All the different single-particle theories finally amount to approximating the self-energy $\Sigma$.

The GW-approximation is a single particle theory, where the self-energy is expanded into a Taylor series after the single particle Green's function G and the screened Coulomb interaction W. This Taylor series is then truncated after the term of first order [53].

$$\Sigma \approx i\mathrm{GW} \tag{2.13}$$

It has been shown by Delerue et al. that the self-energy corrections made by the GW approximation to the single particle gap are especially important in 1D and 2D structures, due to the macroscopic surface polarization [30]. Thus, for monolayers of TMDs the corrections made by GW approximation are assumed to be particularly large.

So, finally, after having approximatively calculated the self-energy $\Sigma$ using Equation (2.13) and the single-particle energies $E_i$ from Equation (2.12) one obtains the electronic band gap $E_{\mathrm{G}}$ and the electronic band structure. Still, as previously described, the electronic band gap is sufficient only to explain photoemission processes or tunneling currents but not PL. To obtain the excitonic binding energies $E_{\mathrm{EXC}}$ and following from that the optical band gap $E_{\mathrm{OPT}}$, one more calculation step is necessary.

One possibility to calculate the excitonic binding energy is the two-dimensional Mott-Wannier model for excitons. In this model, the binding energies are obtained as eigenvalues to the two-dimensional one-particle Schrödinger equation in a Coulomb potential.

The excitonic binding energy is obtained as the ground state energy $E_{\mathrm{ex,n=0}} = E_{\mathrm{EXC}}$.

$$\left(-\frac{\hbar^2}{2\mu_{\mathrm{EXC}}}\nabla^2_{\mathrm{2D}} - \frac{1}{4\pi\epsilon_0\epsilon_{\mathrm{M}}^{\mathrm{2D}}(\mathbf{q}_{\parallel})}\frac{q^2}{|\mathbf{r}_{\mathrm{n}} - \mathbf{r}_{\mathrm{p}}|}\right)\psi\left(\mathbf{r}_{\mathrm{n}}\right) = E_{\mathrm{ex,n}}\,\psi\left(\mathbf{r}_{\mathrm{n}}\right) \tag{2.14}$$

This equation strongly resembles the classical Schrödinger equation for the hydrogen atom, with the only differences that it is reduced to two dimensions and contains the effective exciton mass $\mu_{\mathrm{EXC}}$ and the nonlocal quasi-2D dielectric function $\epsilon_{\mathrm{M}}^{\mathrm{2D}}(\mathbf{q}_{\parallel})$ to account for a screening of the Coulomb interaction between electrons (at location $\mathbf{r}_{\mathrm{n}}$) and holes (at location $\mathbf{r}_{\mathrm{p}}$) due to the crystalline environment. [13]

The effective exciton mass is given in Equation (2.15).

$$\frac{1}{\mu_{\mathrm{EXC}}} = \frac{1}{m^*_{\mathrm{n}}} + \frac{1}{m^*_{\mathrm{p}}} \tag{2.15}$$

The dielectric function relates the strength of an externally applied field to the screened electric field inside the material. It has been shown by Hüser et al. [54] that the common three dimensional definition of the dielectric constant is not suitable for application in 2D materials. According to the general definition the total potential inside the crystal is averaged over a unit cell and divided by the external potential to obtain the dielectric constant. As in a two-dimensional material the three dimensional unit cell contains a vacuum slab, the conventional calculation averages over the vacuum region as well, thereby leading to a strong dependence of the obtained value for the dielectric constant on the thickness $L$ of the vacuum range. In the limit of $L \to \infty$ the dielectric constant always converges to one which is exactly the value of the dielectric constant in vacuum. Therefore, to obtain a physically meaningful parameter, the averaging has to be limited to the region of the material, which results in Equation (2.16) [54].

$$\frac{1}{\epsilon_{\mathrm{M}}^{\mathrm{2D}}(\mathbf{q}_{\parallel})} = \frac{2}{d}\sum_{G_{\perp}} \exp^{iG_{\perp}z_0}\frac{\sin(G_{\perp}d/2)}{G_{\perp}}\epsilon^{-1}_{\mathbf{G0}}(\mathbf{q}_{\parallel}) \tag{2.16}$$

Here $d$ is the thickness of the material, $z_0$ is the middle of the two-dimensional layer, $G_{\perp}$ is the reciprocal lattice vector orthogonal to the plane and $\epsilon_{\mathbf{G0}}(\mathbf{q}_{\parallel})$ is the dielectric function of the material in the random phase approximation evaluated for a wave vector inside the first Brillouin zone parallel to the plane [54].

The Mott-Wannier model is rather simple but also has some limitations. It can only be applied as long as the exciton mass is isotropic, the band structures close to the fundamental gap are in a good approximation parabolic (in order that the effective masses of electrons and holes are well defined) and as long as the valence and conduction band wave functions are distributed uniformly across the two-dimensional plane, such that their expansion in z-direction can be approximated by a step function [13].

If one of the above requirements is not met one has to solve the Bethe-Salpeter equation (BSE) [55, 56, 57, 58]. This is the second possibility for calculating an excitonic spectrum, which is generally valid but computationally more intensive than the Mott-Wannier model. This equation is written in the basis of electron-hole pairs, which is

defined by a vertical excitation at a given wave vector $\mathbf{k}$ for a hole in valence band state $v$ and an electron in conduction band state $c$. (Equation (2.17))

$$(E_{c\mathbf{k}} - E_{v\mathbf{k}})\, A_{vc\mathbf{k}} + \sum_{\mathbf{k}'v'c'} \langle vc\mathbf{k}|K_{\mathrm{eh}}|v'c'\mathbf{k}'\rangle A_{v'c'\mathbf{k}'} = E_{\mathrm{ex,n}} A_{vc\mathbf{k}} \tag{2.17}$$

$A_{vc\mathbf{k}}$ are the expansion coefficient of the excitonic states in the given basis and $K_{eh}$ is the interaction kernel, which has to describe the screened Coulomb interaction between electron-hole pairs.

**Application to two-dimensional materials**

Now, having thoroughly studied the theoretical foundations of density functional theory, the steps to perform DFT calculations in practice shall be briefly outlined.

In a first step one solves the Kohn-Sham Equations (2.6) self-consistently for all atoms inside the basic cell of a crystal. As an input the crystal structure, depending on the lattice constants, has to be defined. Therefore, the wave functions are expanded into plane waves, or more precisely, Bloch waves, which are the common basis for describing periodic systems. The k-space inside the first Brillouin zone is discretely sampled.

The expansion into plane waves requires a three dimensional periodicity, which in the case of two-dimensional materials has to be established using supercells, containing, above the two-dimensional crystal sufficiently thick slabs of vacuum (thickness $L$) in order to ensure that there is no interaction between periodically repeated structures.

In the second step the obtained wave functions and eigenvalues from the converged solution of the Kohn-Sham Equations (2.6) are used to create a first guess of the Green's function $G_0$ and the screened Coulomb potential $W_0$. The self-energy $\Sigma = iG_0W_0$ (Equation (2.13)) can then be used to calculate a new Green's function in a Dyson equation, which serves again as an input for a new self-energy until self-consistency is reached. This process is called $\mathrm{GW}_0$ approximation and is computationally demanding. Therefore, the iteration is often stopped after the first or the second step, leading to the $\mathrm{G}_0\mathrm{W}_0$ or the $\mathrm{G}_1\mathrm{W}_0$ approximation.

At this stage of the calculations one knows the electronic gap $E_{\mathrm{G}}$. The electron affinity $\chi$ can be obtained by referring the band energies to the asymptotic value of the Hartree potential $v_{\mathrm{H}}(\mathbf{r})$ in the vacuum slab between the monolayers. This way one obtains the distance of the DFT band edges ($\epsilon_0$) to vacuum and the GW corrections are added symmetrically, to open up the band gap to the value which was obtained using the GW correction.

For a two-dimensional structure it is very important to use a truncated Coulomb potential $v_c(\mathbf{r})$ for the calculation of the screened Coulomb interaction $W_0$ instead of the classical long ranged $1/r$ Coulomb interaction [59, 54]. Otherwise, even for large vacuum slabs $L$ there is an interlayer screening between adjacent supercells, leading to a systematic underestimation of the band gap by roughly 0.2 eV [59]. The exact value of underestimation depends strongly on k-Point grid and the interlayer spacing $L$.

Additionally, to calculate the screened Coulomb interaction $W_0$, one has to use the quasi-2D dielectric function $\epsilon_{\mathrm{M}}^{\mathrm{2D}}(\mathbf{q}_{\parallel})$, which was described previously in Equation (2.16).

Due to the strong dependence of the 2D dielectric function on the wave vector **q** for small values of **q**, the convergence of the system with k-Points is very slow. The convergence gets much faster when using either a 3D dielectric function or a non-truncated Coulomb interaction, but in this case the calculations converge to a wrong value. In fact, it was shown that a too coarse k-Point grid leads to an overestimation of the band gap, partially compensating the underestimation due to interlayer screening when using the full Coulomb potential [54].

After having obtained correct values for $E_{\mathrm{G}}$ and $\chi$ as well as for the whole band structure $E(k)$ one can apply either Equation (2.14) on the electronic wave functions or Equation (2.17) on an electron- hole pair basis to obtain the excitonic binding energies, which lead to $E_{\mathrm{EXC}}$ and $E_{\mathrm{OPT}}$.

When discussing TMDs there is one more effect which has to be taken into account. Due to the lack of inversion symmetry in monolayers with the 2H structure (see Figure 2.2(c)) the spin- orbit interactions lead to a splitting of the valence band [25]. The spin orbit interactions or spin orbit coupling (SOC) can be included into the calculations either perturbatively [59, 13] or by using a full set of spinorial wave functions as input to the Kohn-Sham equations [58]. This issue arises only for TMDs, whereas all other points, which have been addressed up to now are valid for any two-dimensional semiconductor.

Finally, it shall be emphasized that calculations of the band structure not employing any GW correction might, per coincidence, lead to the right value of the optical band gap [45], but actually have no real physical meaning [53, 24].

In the following, the values for the band gap of monolayer $MoS_2$, as obtained by different groups using the GW approximation, are compared. In Table 2.3 all results are listed together with the most important criteria regarding the validity of the values. In the second column of this table the used functional, the level of accuracy in the GW approximation and the model used for calculating excitonic binding energies are given (HSE stands for the Heyd-Scuseria-Ernzerhof functional [60]). In the next column it is stated, whether or not this work accounted for spin-orbit coupling (SOC). The next two columns hold information about, whether Coulomb truncation and a two-dimensional form of the dielectric constant were used or not. Furthermore, the interlayer spacing $L$, the k-Point grid and the lattice constant $a$ used in the calculations are listed. The last four columns hold the obtained results, the electronic band gap $E_{\mathrm{G}}$, the optical band gap $E_{\mathrm{OPT}}$, the excitonic binding energy $E_{\mathrm{EXC}}$ and the electron affinity $\chi$.

The fact that these values vary substantially is not surprising since different models were used to obtain these values. Of course none of these values is exact, but still the accuracy can be judged according to the following points. (not sorted by relevance but by the order in which these criteria are listed in Table 2.3)

- Applying the BSE equation is more general than the MW-model which is why it should be preferred.
- SOC should be taken into account (only for TMDs).
- The Coulomb interaction should be truncated.

| Source | Method | SOC | Coulomb | $\epsilon_{\mathrm{M}}$ | $L$ | k-Point | $a$ | $E_{\mathrm{G}}$ | $E_{\mathrm{OPT}}$ | $E_{\mathrm{EXC}}$ | $\chi$ |
|---|---|---|---|---|---|---|---|---|---|---|---|
| [59] | LDA+$G_1W_0$+BSE | yes | truncated | 2D | 25 Å | 24x24x1 | 3.15 Å | 2.67 eV | 2.04 eV | 0.63 eV | - |
| [61] | PBE+$GW_0$ | no | truncated | 2D | 10 Å | 18x18x1* | 3.18 Å | 2.65 eV | - | - | - |
| [62] | PBE+$G_0W_0$+BSE | yes | truncated | 3D | 25 Å | 60x60x1 | 3.18 Å | 2.63 eV | 2.01 eV | 0.62 eV | - |
| [13] | LDA+$G_0W_0$+MW | yes | truncated | 2D | 20 Å | 30x30x1 | 3.18 Å | 2.48 eV | 2.01 eV | 0.47 eV | $-3.84$ eV |
| [63] | PBE+$G_0W_0$ | yes | truncated | 3D | 17 Å | 12x12x1 | 3.19 Å | 2.5 eV | - | - | $-3.75$ eV |
| [61] | PBE+$G_0W_0$ | no | truncated | 2D | 10 Å | 18x18x1* | 3.18 Å | 2.54 eV | - | - | - |
| [64] | PBE+$G_0W_0$ | no | truncated | 3D | 23 Å | 12x12x1 | 3.18 Å | 2.75 eV | - | - | $-3.74$ eV |
| [24] | LDA+$GW_0$+MW | yes | full | 3D | 19 Å | 8x8x2 | 3.16 Å | 2.76 eV | 1.86 eV | 0.9 eV | - |
| [28] | PBE+$G_0W_0$+BSE | yes | full | 3D | $\to \infty$ | 12x12x1 | 3.18 Å | 2.97 eV | 1.8 eV | 1.1 eV | - |
| [65] | HSE+$G_0W_0$+BSE | yes | full | 3D | 15 Å | 6x6x1 | 3.18 Å | 2.82 eV | 1.97 eV | 0.85 eV | - |
| [58] | LDA+$G_0W_0$ | yes | full | 3D | 22 Å | 18x18x1 | 3.15 Å | 2.41 eV | - | - | - |
| [42] | PBE+$GW_0$+BSE | yes | full | 3D | 9 Å | 9x9x1 | 3.18 Å | 2.4 eV | 1.84 eV | 0.56 eV | - |
| [66] | PBE+$G_0W_0$+BSE | no | full | 3D | 15 Å | 11x11x1 | 3.16 Å | 2.68 eV | 2.3 eV | 0.38 eV | $-3.89$ eV |
| [40] | PBE+$G_0W_0$+BSE | no | full | 3D | 19 Å | 15x15x1 | 3.16 Å | 2.76 eV | 2.22 eV | 0.54 eV | - |
| [67] | LDA+$GW_0$ | no | full | 3D | 15 Å | 12x12x1 | 3.11 Å | 2.57 eV | - | - | - |

Table 2.3: DFT results for the band structure of monolayer $MoS_2$. All results refer to vacuum environment, $T = 0\,\mathrm{K}$. The values marked with * have been calculated using an analytic integration for $\mathbf{q} \to 0$.

| Source | Substrate | $E_{\mathrm{G}}$ | $E_{\mathrm{OPT}}$ | $E_{\mathrm{EXC}}$ |
|---|---|---|---|---|
| [28] | 1L-hBN | 2.5 eV | 1.8 eV | 0.7 eV |
| [28] | 1L-Graphene | 2.0 eV | 1.8 eV | 0.2 eV |

Table 2.4: DFT results for the band structure of monolayer $MoS_2$ on different substrates. The DFT parameters are the same as given for reference [28] in Table 2.3.

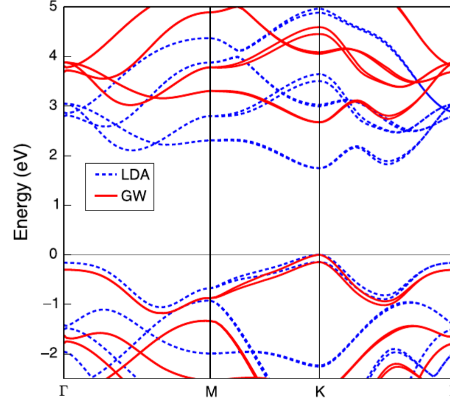


Figure 2.7: Band structure of monolayer $MoS_2$. [59]

- A useful two-dimensional definition for the dielectric constant should be used.
- The interlayer distance should be as large as possible, preferably larger than 20 Å.
- The k-Point grid should be as dense as possible, preferably denser than 20x20x1.
- The lattice constant should either be chosen as the experimental value of bulk $MoS_2$ [68], $a = 3.16$ Å, or the most common lattice constant as obtained by relaxing the structure in the framework of DFT, $a = 3.18$ Å.

Taking all these criteria into account, the values obtained by Qiu et al. [59] seem to be the most exact calculations available at this time. Also the band gaps calculated by Qiu et al. come very close to the experimentally obtained values for a suspended $MoS_2$ layer of Klots et al. [26] (see Table 2.1). Unfortunately, Qiu et al. did not provide the electron affinity, which is therefore taken from Rasmussen et al. [13]. These values can certainly still be improved, and what is even more important is that all these values describe the artificial case of a suspended monolayer in vacuum at 0 K. Only Komsa et. al.[28] calculated the effect of a substrate on the band structure by including a single layer of either graphene or hexagonal boron nitride (hBN) into the superlattice basic cell. These materials were, for simplicity, assumed to be lattice matched with monolayer $MoS_2$. Thus the values, which are given in Table 2.4, are only a rough estimate. Still, they demonstrate that the electronic band gaps can be reduced substantially due to dielectric screening of other adjacent materials. Similar tables as Table 2.3 for $MoSe_2$ (Table A.6), $WS_2$ (Table A.7) and $WSe_2$ (Table A.8) can be found in Appendix A.2. The band structure of a single layer $MoS_2$, as it was calculated by Qiu et al. is given in Figure 2.7.

Having obtained a band structure, the effective masses at the minima of the bands can be calculated using Equation

$$\frac{1}{m^*} = \frac{1}{\hbar^2} \frac{\partial^2 E(k)}{\partial k}\bigg|_{\min} . \tag{2.18}$$

The concept of the effective mass relies on the fact that usually a harmonic approximation of the band structure in the relevant minima is sufficient for describing transport phenomena. The band structure of single layer $MoS_2$ is anisotropic. Therefore, one distinguishes a longitudinal effective mass, which is calculated in the direction from the minimum at the K-point to the middle of the Brillouin zone, the Γ-point, and a transversal effective mass, which is calculated orthogonal to that direction. Nevertheless, the anisotropy is rather small. Therefore, the geometric mean, which is common in this context since the density of states mass is defined via this mean, is used to average over the values for the effective mass in different directions. The effective masses from different sources at the K-point are given in Table 2.5 for comparison.

| Source | $m^*_\mathrm{n}/m_0$ | $m^*_\mathrm{p}/m_0$ |
|---|---|---|
| [13] | 0.55 | 0.56 |
| [24] | 0.34* | 0.44* |
| [65] | 0.6 | 0.54 |
| [40] | 0.36 | 0.39 |

Table 2.5: Effective masses for charge carriers in monolayer $MoS_2$.($m_0$ stands for the electron mass in vacuum) The values marked with "*" were obtained by taking the geometric mean over the values given in the reference.

Again the values for the effective masses, as obtained by different groups, are quite different. Following the same criteria as already employed when evaluating which of the band gap data is most valid, the values obtained by Rasmussen et al. [13] are found to be most reliable. A table containing the effective masses for $MoSe_2$, $WS_2$ and $WSe_2$ (Table A.11) is given in Appendix A.3.

When turning towards the calculation of the band structure of multilayer TMDs or even bulk material, Van der Waals (VDW) forces have to be included into the DFT calculations. VDW forces are the main bonding force between monolayers but since they are non-local effects, they are not part of the standard DFT. To account for these effects, several theories like DFT-D, DFT-TS, ACFDT or VDW-DF have been developed, which all add an energy correction term to the total energy of the system. These energy corrections have been described in detail elsewhere [47, 69].

In Table 2.6 the results obtained by different groups, for the band gaps in multilayer $MoS_2$, are given. The first column gives the number of layers, where B stands for bulk. The second column is used to distinguish between different structures of the crystal (see also Figures 2.2(a), 2.2(b)). As there is a transition from a direct to an indirect semiconductor when increasing the number of layers, the direct and indirect gaps are

| N | St. | Source | Method | $L$[Å] | k-Point | $a/c$[Å] | $E_{\mathrm{G}}{}^{\mathrm{d}}/{}^{\mathrm{i}}$[eV] | $E_{\mathrm{OPT}}{}^{\mathrm{d}}/{}^{\mathrm{i}}$[eV] | $E_{\mathrm{EXC}}{}^{\mathrm{d}}$[eV] | $\chi$[eV] |
|---|---|---|---|---|---|---|---|---|---|---|
| 2 | 2H | [70] | ACFDT+$G_0W_0$+BSE | 20 | 16x16x2 | 3.14/12.29 | 2.41/1.96 | 2.08/- | 0.33 | - |
| 2 | 2H | [42] | PBE-D+$GW_0$+BSE | 9 | 9x9x1 | 3.18/- | -/1.96 | 1.82/1.5 | - | - |
| 2 | 2H | [24] | LDA+$GW_0$+MW (!) | 19 | 8x8x2 | 3.16/- | 2.43/1.88 | 2.01/1.34 | 0.42 | - |
| 2 | 2H | [28] | PBE-D+$G_0W_0$+BSE | $\rightarrow\infty$ | 12x12x1 | 3.18/12.34 | 2.4/2.0 | 2.0/- | 0.4 | - |
| 2 | 2H | [58] | LDA+$G_0W_0$ (!) | 27 | 18x18x1 | 3.15/12.3 | 2.32/- | -/- | - | - |
| 2 | 1T | [70] | ACFDT+$G_0W_0$+BSE | 20 | 16x16x2 | 3.14/12.29 | 2.29/1.82 | 2.06/- | 0.23 | - |
| 2 | 1T | [35] | PBE-TS+$G_0W_0$ | 20 | 12x12x1 | 3.16/- | -/1.83 | -/- | - | - |
| 3 | 2H | [28] | PBE-D+$G_0W_0$+BSE | $\rightarrow\infty$ | 12x12x2 | 3.18/12.34 | 2.1/1.6 | 1.95/- | 0.15 | - |
| B | 2H | [52] | PBE+$GW_0$ (!) | 15 | 12x12x2 | 3.17/12.32 | 2.07/1.23 | -/- | - | -4.22 |
| B | 2H | [24] | LDA+$GW_0$+MW (!) | - | 8x8x2 | 3.16/- | 2.01/1.29 | -/- | - | - |
| B | 2H | [28] | PBE-D+$G_0W_0$+BSE | - | 12x12x3 | 3.18/12.34 | 2.0/1.3 | 1.87/- | 0.13 | - |
| B | 2H | [58] | LDA+$G_0W_0$ (!) | - | 18x18x3 | 3.15/12.3 | 2.23/- | -/- | - | - |

Table 2.6: DFT results for the band structure of multilayer $MoS_2$. Even though it might cause errors in case of two and three layers all calculations were performed using a full Coulomb interaction and the three dimensional form of the dielectric constant. Spin-orbit coupling is taken into account in all of the listed calculations. An exclamation mark (!) behind a method is used to underline that in these calculations VDW interactions were not accounted for.

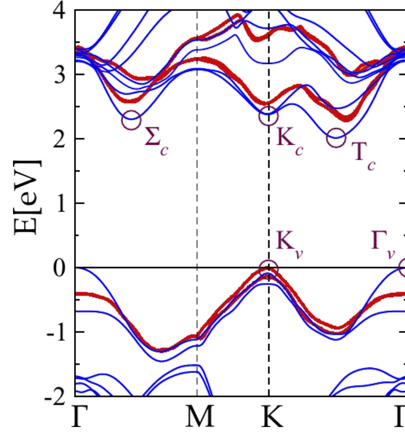


Figure 2.8: Band structure of bilayer $MoS_2$ in the 2H structure. Comparing the band structure for monolayer $MoS_2$ (red line), with the band structure of bilayer $MoS_2$ (blue line) illustrates the transition from direct semiconductor ($K_c \rightarrow K_v$) to an indirect semiconductor ($T_c \rightarrow \Gamma_v$). [70]

always given. The electron affinity $\chi$ refers to the distance of the indirect conduction band edge to vacuum.

The values match surprisingly well, even though some groups did not take VDW interactions into account at all. The results of He et al. [70] seem to be the most reliable, which is why the band structure for bilayer $MoS_2$ as calculated by He et al. [70] is shown in Figure 2.8. A similar table for multilayer $MoSe_2$ (Table A.9) is given in Appendix A.2, where data about the influence of a substrate on several layer $MoSe_2$ is listed as well (Table A.10).

## 2.4 Carrier Mobility

Carrier mobilities in semiconductors are influenced by a variety of physical mechanisms. In conventional bulk semiconductors, the standard values for the carrier mobility are well known. All main parameters which affect the mobilities have been thoroughly studied, and empirically fitted models exist to take the dependence of the mobility on temperature, doping density or surface to volume ratio into account [71, 72].

In Section 2.3 it was shown that the band structure of TMDs in their two-dimensional form depends on many more factors than the band structure of bulk silicon (compare Figure 2.6). Thus, it is expected that the mobility of the carriers will, additionally to the common dependencies such as temperature, depend as well on most of the factors discussed in Section 2.3 such as layer number or surrounding materials. For example, it is generally agreed that by increasing the number of layers or by using an encapsulation, the mobility is improved [7]. What is more, depending on the measurement process used to determine the mobility, the contacts to the channel can influence the numerical value of the mobility a lot. This issue will be addressed in Section 2.5. To the present day no detailed investigations or models about the dependence of the mobility of two-

dimensional materials on different parameters exist, but only exemplary values for the mobility are reported in literature. The mobility value can be easily obtained from measurements, which were performed as described in Section 3.2.1. Therefore, in this section only some reference values from literature together with a detailed description of the extraction technique will be presented.

### 2.4.1 Electrons

Due to the electron mobility's numerous dependencies, the mobility of $MoS_2$ as it is reported in literature varies over several decades ($0.1 - 34\,000\,\mathrm{cm^2/Vs}$).

The highest mobility value, which has been reported was measured by Cui et al. [9]. They performed Hall measurements obtaining $34\,000\,\mathrm{cm^2\ V^{-1}s^{-1}}$ on a completely encapsulated six-layer $MoS_2$ sample in hexagonal boron nitride at low temperature. For high quality $MoS_2$ monolayers on silicon dioxide after substantial annealing, intrinsic Hall mobilities of around $500\,\mathrm{cm^2\ V^{-1}s^{-1}}$ were measured at low temperature [73].

Apart from this apparently high intrinsic mobility, for simulations the effective value of the mobility at room temperature, is of interest. The reduced value of the mobility due to contact resistance is termed "effective electron mobility" $\mu_\mathrm{n}^\mathrm{eff}$. In the present work, back gated devices consisting of monolayer $MoS_2$ samples, produced by mechanical exfoliation and deposited on silicon dioxide are studied. The devices were contacted using Ti/Au contacts (see Section 2.6). For similar devices literature agrees on values of the effective mobility in the range of $\mu_\mathrm{n}^\mathrm{eff} \approx 0.1 - 10\,\mathrm{cm^2/Vs}$, [74, 7, 75], (compare Table 2.7).

The effective mobility of our samples was extracted from the $I_\mathrm{D}\,(V_\mathrm{G})$ characteristics using the Formula (2.19). [76, 7, 77] Commonly the maximum value of the numerically calculated derivative is taken [76].

$$\mu_\mathrm{n}^\mathrm{eff} = \frac{\partial I_\mathrm{D}}{\partial V_\mathrm{G}} \cdot \frac{L}{W C_\mathrm{ox}^* V_\mathrm{D}} \tag{2.19}$$

This expression is the first derivative of the analytic approximation for the output characteristic $I_\mathrm{D}\,(V_\mathrm{D})$ (Equation (2.20)) with respect to the gate voltage in the ohmic region. Thus a small drain voltage is a prerequisite for applying this equation. $C_\mathrm{ox}^*$ is the oxide capacitance per unit area $C_\mathrm{ox}^* = \epsilon_0 \epsilon_r / d_\mathrm{ox}$.

$$I_\mathrm{D} = \frac{W}{L} \mu_\mathrm{n}^\mathrm{eff} C_\mathrm{ox}^* \left[ (V_\mathrm{G} - V_\mathrm{th})\, V_\mathrm{D} - \frac{V_\mathrm{D}^2}{2} \right] \tag{2.20}$$

The effective mobilities of other TMDs are within the same range as those of $MoS_2$. For example a back-gated monolayer $WSe_2$ transistor on $SiO_2$ capped with aluminium dioxide shows a value of $\mu_\mathrm{n}^\mathrm{eff} = 202\,\mathrm{cm^2/Vs}$ [78], nearly the same value as Radisavljevic et al. [7] obtained for a back-gated monolayer $MoS_2$ transistor on $SiO_2$ capped with hafnium dioxide ($\mu_\mathrm{n}^\mathrm{eff} = 200\,\mathrm{cm^2/Vs}$).

### 2.4.2 Holes

The hole mobility in $MoS_2$ is measured more rarely than the electron mobility, since few-layer $MoS_2$ transistors exhibit nMOS characteristics in most cases [7, 75, 73, 79]. pMOS

characteristics were obtained by using $MoO_x$ contacts and a mobility of $\mu_p \approx 90\,\mathrm{cm^2/Vs}$ was reported [80]. Thus, the hole mobility lies in the same range as the electron mobility.

## 2.5 Contacts

The performance of electronic devices based on two-dimensional crystals is strongly affected by the electrical contacts that connect the 2D material to the surrounding circuits. The quality of such contacts is quantified through the contact resistance, which will be discussed in this section.

When studying the interface between two-dimensional and bulk material, two basic geometries are possible. Either a top contact, where the metal is attached to the 2D semiconductor only at the top of the 2D layer, or an edge contact, where the contact is established only at the edge of the layer. In reality contacts are usually a mixture of both types. The contact area is a lot larger for the top contact, which makes this contact more important than the edge contact [81].

In general, the top contact suffers from a VDW gap between the metal and the 2D material, because the pristine surfaces of two-dimensional materials do not tend to form covalent bonds. This gap acts as an additional tunnel barrier for charge carriers before the Schottky barrier, which is inherent to all metal-semiconductor contacts. At an edge contact there is no VDW gap but the contact area is extremely small, hence strongly limiting the current. Therefore, it is desirable to reduce the tunnel barrier at the top surface. Using DFT simulations, it was shown that some metals can form covalent bonds to the surfaces of 2D semiconductors by changing the hybridization state of the transition metal atoms at the surface. For example, Ti and Mo can bond covalently to the surface of $MoS_2$ and Pd and W can bond covalently to the surface of $WSe_2$ [82, 83, 84, 85]. What is more, these studies predict that hybridization creates non-localized states in the original band gap of $MoS_2$, which effectively turns $MoS_2$ under the contacts into a new metallic compound. Still, it has to be noted that the DFT predictions for strong hybridization are based on the assumption of perfect interfaces, which in reality has to be established by surface cleaning before contact deposition and an annealing step following the deposition process [81].

Even if the tunnel barrier at the top contact can be suppressed by strong hybridization using appropriate contact materials, the Schottky barrier remains. In earlier works several authors claimed to observe ohmic contacts, as the output characteristics $I_D(V_D)$ of $MoS_2$ transistors are linear [7]. Still, Das et al. [76] showed that this linear relation is mainly due to large tunneling currents across the barriers above threshold. One has to distinguish two charge injection mechanisms across the Schottky barriers. One is thermionic emission, dominating the transistor behaviour for voltages below threshold and field-emission or tunneling, dominating above threshold.

As the Schottky barrier is always present, the correct measurement of this parameter is crucial. In the ideal case, the Schottky-Mott rule states that the Schottky barrier height $\phi_{\mathrm{B0}}$ is determined by the difference between the metal's work function $\phi_{\mathrm{M}}$ and the semiconductor's electron affinity $\chi$ [86]

$$\phi_{\mathrm{B0}} = \phi_{\mathrm{M}} - \chi. \tag{2.21}$$

In reality however, the Fermi level is often pinned. The Fermi level pinning can be quantified by looking at the dependence of the Schottky barrier height on the metal work function. The dependence parameter $S$ is defined as

$$S = \frac{\mathrm{d}\phi_{\mathrm{B0}}}{\mathrm{d}\phi_{\mathrm{M}}}. \tag{2.22}$$

$S = 1$ corresponds to the ideal case and $S = 0$ to complete Fermi level pinning. For $MoS_2$ the parameter $S$ was evaluated to 0.09, indicating strong Fermi level pinning [81]. The mechanism of this Fermi level pinning is twofold. On the one hand it is due to creation of interface dipoles, leading to significant band realignment, and on the other hand it is due to formation of energy gap states by a weakened Mo-S bond at the interface [87].

The exact measurement procedures for extracting the Schottky barrier heights have been discussed elsewhere [81, 76, 88]. For example, the Schottky barrier height for Ti contacts on $MoS_2$ amounts to $\phi_{\mathrm{B0}} = 50\,\mathrm{meV}$ [76] and the Schottky barrier height for Au contacts on $MoS_2$ was measured as $\phi_{\mathrm{B0}} = 126\,\mathrm{meV}$ [88] and as $\phi_{\mathrm{B0}} = 190\,\mathrm{meV}$ [89].

The reduction of the Fermi level pinning would be desirable, because the Fermi level pinning is one of the factors which make the production of pMOS transistors out of $MoS_2$ so difficult. Still, pMOS transistors are necessary building blocks for CMOS applications. Nearly all $MoS_2$-based FETs exhibit nMOS characteristics. On the one hand due to the natural n doping of $MoS_2$ and on the other hand due to pinning of the Fermi levels of all metals close to the conduction band edge. Only the very high work function material $MoO_x$ has been proven successful in injecting holes into the valence band [80]. $WSe_2$ is more versatile, having a reported nMOS behaviour when contacted with Al, Ti, In, or Ag[78] and a pMOS behaviour when contacted with Pd [90], or Ag[91]. One possibility for reducing Fermi level pinning is the decoupling of the metal from the TMD's surface by introducing an oxide or graphene interlayer [81].

Another very important parameter for characterizing the contact is the contact resistance. It depends on the resistivity of the metal to TMD interface $r_{\mathrm{C}}$ (measured in $\Omega\mathrm{m}^2$) and on the sheet resistance of the TMD $\rho^{\mathrm{2D}}$ (measured in $\Omega/\square$). If the contact is diffusive, meaning that charge carriers are scattered many times in the semiconductor before entering the metal, the transmission line model is valid. In TMDs the mean free path is small, therefore the transmission line model can be applied, resulting in the contact resistance $R_{\mathrm{C}}$ (in $\Omega\,\mathrm{m}$) [81].

$$R_{\mathrm{C}} = \sqrt{\rho^{\mathrm{2D}} r_{\mathrm{C}}} \coth\left(\frac{l}{L_{\mathrm{T}}}\right), \qquad L_{\mathrm{T}} = \sqrt{\frac{r_{\mathrm{C}}}{\rho^{\mathrm{2D}}}} \tag{2.23}$$

In this expression $l$ stands for the contact length and $L_{\mathrm{T}}$ is the so called transfer length. This is the average distance that a charge carrier travels in the semiconductor below the

contacts before it enters the contact. If the transfer length is a lot smaller than the contact length, the contact resistance becomes $R_C = \sqrt{\rho^{2D} r_C}$ [81]. The contact resistance of a Ti/Au contact on single layer $MoS_2$ is approximately $1 \times 10^5\,\Omega\,\mu m$ ($2.6 \times 10^4\,\Omega\,\mu m$[73], $4.2 \times 10^4\,\Omega\,\mu m$[88], $3.0 \times 10^5\,\Omega\,\mu m$[92]). The variation is not surprising as the contact resistance depends strongly on the processing of the contacts.

Liu et al. [92] studied the dependence of the contact resistance on the gate voltage and showed that there is a strong decline of the contact resistance with increasing gate voltage in nMOS single layer $MoS_2$ based transistors. This variation is rather unexpected. In conventional silicon technologies the resistivity of the interface as well as the sheet resistance are constant, whereas in few layered TMDs they are modulated with gate voltage. This is because above threshold voltage a higher electric field leads to an increased tunneling over the Schottky barrier, thereby increasing the carrier density $n$. The increased carrier density narrows the Schottky barrier, facilitating more tunneling. “In this case the semiconductor can be viewed as being electrostatically doped by gate biasing.”, as Liu et al. [92] put it.

Furthermore, Liu et al. [92] observed that the contact resistance actually depends stronger on the gate voltage than the sheet resistance, illustrating that it is rather the contact than the channel which is sensitive to changes in the gate voltage. Therefore, it is concluded that the on/off switching in few layered TMD - transistors is not primarily achieved by accumulating/depleting the carrier density in the channel but rather by tuning the Schottky barrier height for electrons. Therefore, the studied transistors are rather Schottky barrier transistors than depletion transistors like conventional silicon devices. Based on this knowledge Liu et al. [92] question the applicability of Equations (2.19) and (2.20) to such devices. Still,it is argued in this work that the conventional drift diffusion model can be applied when considering the extracted mobility (Equation (2.19)) not as a material property of the channel but as a property of the contacts, describing the extent of Schottky barrier height tuning by the applied voltage.

## 2.6 Devices

In a MOSFET the current through a channel is controlled by the voltage applied at the gate contact. The common transistor geometries for silicon technologies have to be adapted when using a 2D material as a channel. At the current stage of research two main transistor geometries are being studied, the top-gate geometry and the back-gate geometry (see Figure 2.9).

The typical production flow for two-dimensional devices always follows the same steps. As a substrate a silicon wafer is used, which at the same time can be used as a back-gate. On the entire wafer a dielectric is deposited in the next step. On the dielectric, flakes of the respective 2D material are isolated using various exfoliation or deposition techniques, which have been described in Section 2.1. In the next step metallic contacts are patterned on top of a suitable flake. This is done using either direct writing technologies like electron beam lithography followed by an evaporation step or alternatively using electron beam induced deposition to fabricate the contacts in one step. With patterning the

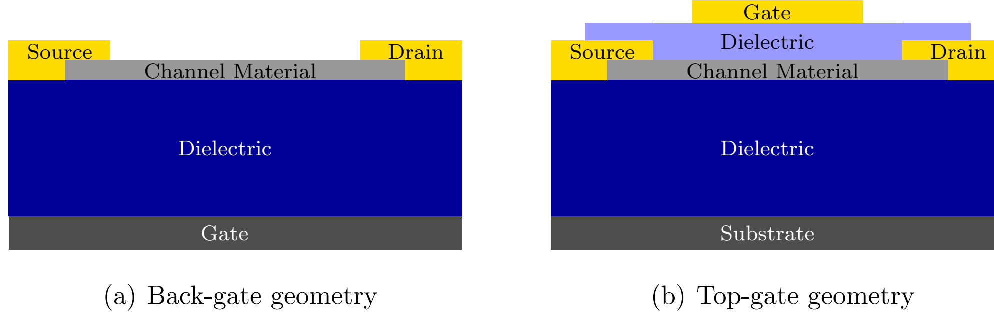


(a) Back-gate geometry (b) Top-gate geometry

Figure 2.9: Schematic drawing of transistor geometries used with 2D channel materials.

contacts, width ($W$) and length ($L$) of the channel are defined and a common back-gate transistor is already finished. If the channel shall be controlled via a top gate or an encapsulation of the 2D material is desired, an additional dielectric layer is deposited using for example atomic layer deposition (ALD). The top-gate transistor is finished after the final patterning of the metallic gate contact.

The devices studied in this work use back-gate geometry. They were fabricated on double-side polished and thermally oxidized silicon substrates with a resistivity of 1-5 Ω cm. $MoS_2$ flakes were exfoliated from a natural bulk crystal on top of the silicon dioxide layer ($d_{SiO_2} = 90\,\mathrm{nm}$). In the next step a monolayer flake was identified using optical microscopy, its thickness being verified using Raman spectroscopy ($d_{MoS_2} = 0.65\,\mathrm{nm}$). Four devices were patterned next to each other on this flake by depositing Ti/Au contacts using electron beam lithography and evaporation ($d_{Au} = 120\,\mathrm{nm}$, $d_{Ti} = 9.5\,\mathrm{nm}$). The contact length $L_C$ of the contacts was about 2.0 µm and the channel length $L = 1\,\mu\mathrm{m}$ for all devices. The contact width varied for different devices, $W_A = 6.8\,\mu\mathrm{m}$, $W_B = 8.0\,\mu\mathrm{m}$, $W_C = 6.4\,\mu\mathrm{m}$, $W_D = 4.8\,\mu\mathrm{m}$. Finally, the devices were annealed at 120 °C for twelve hours at a pressure of $< 6.0 \times 10^{-6}$ mbar. In Figure 2.10 an optical microscopy image of the devices is shown. In Figure 2.11 the measures of the devices are illustrated in a top view and a side view.

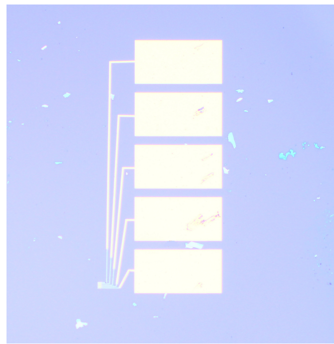

Figure 2.10: Optical microscopy image of the devices. The bottom contact is the source contact to all four devices (A-D), the four contacts above are the drain contacts, the drain contact to device D being located at the top.

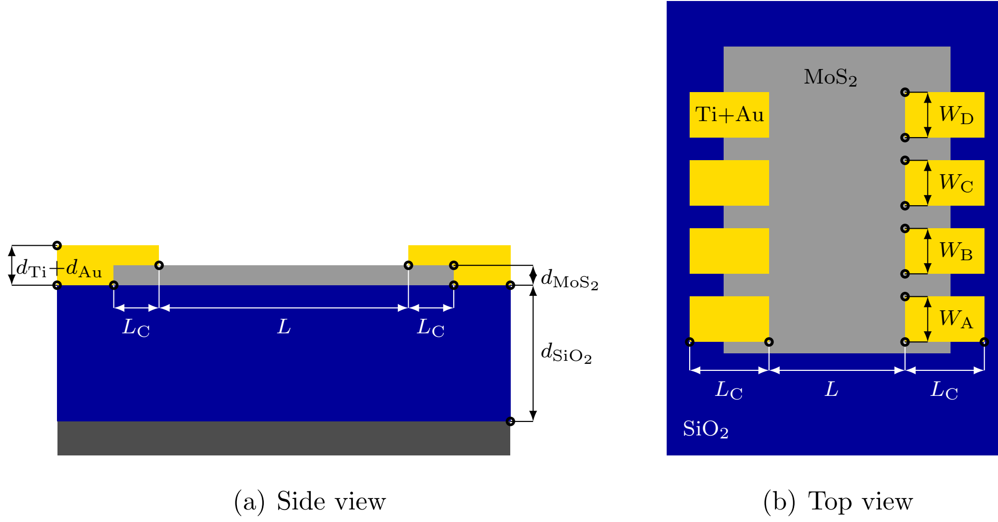


(a) Side view (b) Top view

Figure 2.11: Schematic drawing of the transistor geometry studied in this work including the dimensions.

A comparison of transistor parameters of our devices to those of other groups is given in Table 2.7. In the first section back-gated devices are compared. It can be seen that with the low work function material scandium the highest effective mobility could be measured. Also using more layers of $MoS_2$ as a channel increases the effective mobility. It can also be seen that the layer fabricated by Amani et al. using CVD can obtain as good results as the layers from conventional mechanical exfoliation. In the second section it is apparent that the mobility can be increased by encapsulating the layer. In the third section the data for transistors based on other TMDs than $MoS_2$ are given. In references [93, 94] they used a doping of the contacts with potassium or nitrogen dioxide to lower the Schottky barriers. In comparison, our devices exhibit a relatively low mobility. Nevertheless, this is of minor importance as the impact of defects on the device characteristics shall be studied.

| Source | Geometry | Channel | N | Polarity | Oxide | $d_{OX}$[nm] | Contacts | $L$[µm] | $\mu^{eff}$[cm$^2$/Vs] | $I_{on}/I_{off}$ |
|---|---|---|---|---|---|---|---|---|---|---|
| [7] | Back | $MoS_2$ | 1 | nMOS | $SiO_2$ | 270 | Au | 1.5 | 0.1-10 | - |
| [75] | Back | $MoS_2$ | 1 | nMOS | $SiO_2$ | 300 | Ti/Au | 1.0 | 1.1-10 | $1 \times 10^6$ |
| [95] | Back | $MoS_2$(CVD) | 1 | nMOS | $SiO_2$ | 285 | Ti/Au | 0.4 | 6 | $1 \times 10^7$ |
| [76] | Back | $MoS_2$ | 6 | nMOS | $SiO_2$ | 100 | Sc/Ni | 5.0 | 184 | - |
| [76] | Back | $MoS_2$ | 6 | nMOS | $SiO_2$ | 100 | Pt | 5.0 | 21 | - |
| [80] | Back | $MoS_2$ | 60 | pMOS | $SiO_2$ | 60 | $MoO_x$ | 7.0 | 90 | $1 \times 10^4$ |
| [7] | Top | $MoS_2$ | 1 | nMOS | $HfO_2$ | 30 | Au | 0.5 | 217 | $1 \times 10^6$ |
| [96] | Back | $MoS_2$ | 1 | nMOS | $Al_2O_3$ | 72 | Mo/Au | 2.0 | 13 | $1 \times 10^3$ |
| [79] | Back | $MoS_2$ | 60 | nMOS | $Al_2O_3$ | 50 | Ti/Au | 7.0 | 100 | $1 \times 10^6$ |
| [97] | Top | $MoS_2$ | 23 | nMOS | $Al_2O_3$ | 16 | Ni/Au | 3.0 | 517 | $1 \times 10^8$ |
| [98] | Top | $MoS_2$ | 15 | nMOS | hBN | 55 | Graphene | 3.0 | 26 | $1 \times 10^6$ |
| [99] | Back | $MoSe_2$ | 8 | nMOS | $SiO_2$ | 285 | Ni | 1.8 | 50 | $1 \times 10^6$ |
| [78] | Back | $WSe_2$ | 1 | nMOS | $Al_2O_3$ | 72 | Ag/Au | 1.5 | 40 | $1 \times 10^8$ |
| [93] | Top | $WSe_2$ | 1 | pMOS | $ZrO_2$ | 17.5 | Pd+$NO_2$ | 1.0 | 250 | $1 \times 10^6$ |
| [94] | Top | $WSe_2$ | 3 | nMOS | $ZrO_2$ | 17.5 | Au+K | 6.2 | 110 | $1 \times 10^4$ |
| Own | Back | $MoS_2$ | 1 | nMOS | $SiO_2$ | 90 | Ti/Au | 1.0 | 0.07-0.2 | $1 \times 10^3$ |

Table 2.7: Comparison of transistor parameters for different transistors with a TMD as a channel.

# CHAPTER 3 Oxide Degradation

Degradation is defined as the variation of device parameters, like for example the threshold voltage, with time. In this work, the interaction of charge carriers with defects at the interface between TMD and dielectric and with defects inside the dielectric is identified as the main source of degradation effects.

At first, microscopic defects of silicon dioxide are analyzed based on DFT studies. Then, some measurement techniques for a systematic study of degradation effects will be described. Here on the one hand the hysteresis observed in $I_{\mathrm{D}}(V_{\mathrm{G}})$ characteristics will be discussed and possible reasons for the existence of a hysteresis will be reviewed. On the other hand, popular measurement techniques to evaluate the bias temperature instability will be presented and the measurement procedure applied in this work will be introduced.

## 3.1 Atomistic Defect Structures

Amorphous silicon dioxide is usually grown using thermal oxidation of pure silicon wafers. This general technology is widely used, which is why the microscopic nature of defects in such a thermal oxide is assumed to be independent of the channel material.

The nature of defects in amorphous silicon oxide is typically studied using electron spin resonance measurements (ESR) [100] or by an extensive analysis of measurement data available from modern silicon technology, which will be described in Section 3.1.1. The modeling of the microscopic nature of defects can be done using DFT calculations. In these calculations amorphous silicon dioxide including hydrogen atoms is simulated. Hydrogen atoms are always present in electronic devices, as hydrogen is the most abundant element in silicon device fabrication.[101] The atomistic defect models for the defects, which can explain the phenomena discussed in Section 3.1.1, will be presented in Sections 3.1.2 and 3.1.3, as these defects are the most likely candidates to explain the interaction of oxide defects with charge carriers.

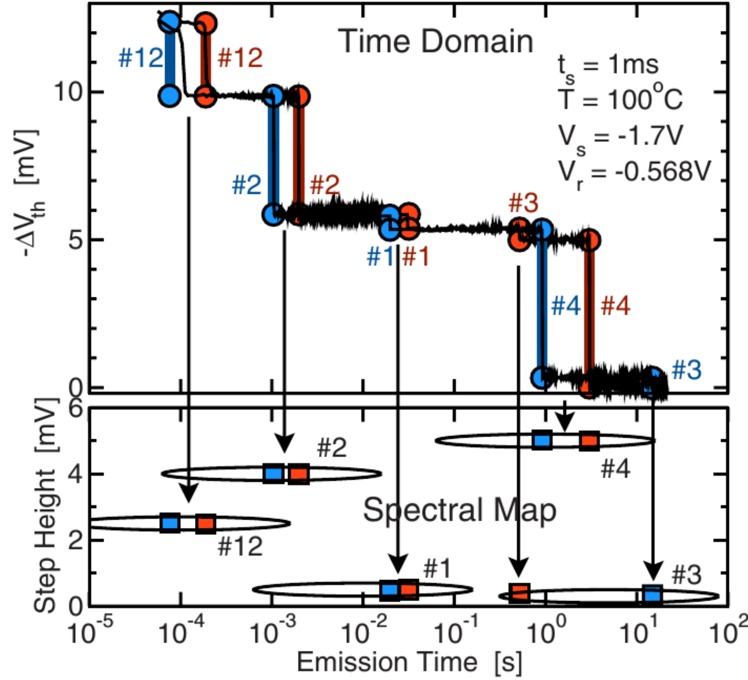


Figure 3.1: Two typical TDDS recovery traces measured on the same nanoscale pMOSFET. [102]

### 3.1.1 Characterization of Single Defects

The Time-dependent defect spectroscopy (TDDS) is one of the most versatile methods for characterising individual defects in nanoscale MOSFETs ($L$ and $W$ around 100 nm). In a typical TDDS measurement a nanoscale device is stressed at a high gate voltage and the shift of the threshold voltage during the subsequent recovery phase is observed. The recovery traces of such small devices show discrete steps. As the step heights are mainly governed by the position of the corresponding trap, the discrete steps can be linked to single hole emission/capture events from one defect. The emission times of the defect are stochastic quantities, this is why a number of recovery traces have to be recorded at the same measurement conditions. In Figure 3.1 at the top, two typical traces of a TDDS measurement are shown. From these traces the step heights and emission times of different defects can be collected and visualized in a spectral map which is shown at the bottom. The step heights and emission times are like unique fingerprints of each defect [102].

To get information about the corresponding capture time constants $\tau_c$ for each defect, the above measurement has to be repeated many times using continuously increasing stress times. If a defect cluster is not there for very short stress times and appears suddenly at one certain stress time, the capture time lies between this stress time and the previous one. In this way capture and emission time constants of single traps for different temperatures and gate voltages can be obtained [103].

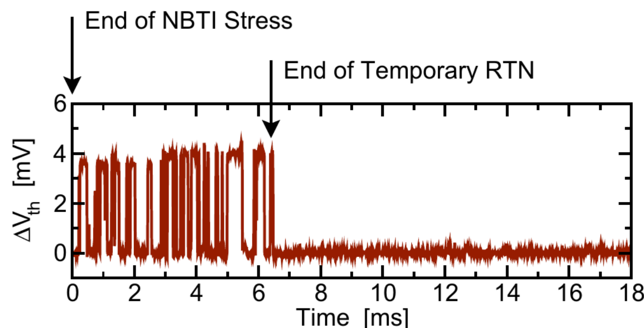


Figure 3.2: Typical measurement of temporary RTN on a pMOSFET. [105]

Sometimes the recovery traces show at some point a random switching between two voltage levels. This phenomenon is called random telegraph noise (RTN). Studies about RTN showed that there are defects, which repeatedly produce noise in the drain current for stochastic amounts of time. This was termed "anomalous RTN" [104]. A very similar phenomenon is the so called "temporary RTN" which is an RTN noise directly after a stress phase, which disappears after a stochastic amount of time. A typical temporary RTN trace can be seen in Figure 3.2 [105].

Any physical defect model has to be able to explain the large variation in capture and emission time pairs for single defects and it has to explain effects such as anomalous RTN. The most widely used defect model states that the trapping of holes is responsible for these effects [106]. In a hole trapping event an electron is injected into the channel from a neutral defect state in the oxide, which thereby becomes positively charged. An explanation of anomalous RTN and the widely distributed defect properties can only be given based on defects that can show metastability in both, the neutral and the positive charge state [101].

In a four-state model anomalous RTN for example can be explained easily. After many hole emission and hole capture events with small time constants, causing the RTN, the defect makes the transition into the positively charged stable state. This state has a higher time constant, therefore, the RTN remains switched off for a longer time until a transition from the stable into the metastable state takes place and the RTN is switched on again.

### 3.1.2 Hydrogen Bridge

In crystalline silicon dioxide all silicon atoms are surrounded by four oxygen atoms in a tetrahedral configuration. Two silicon atoms always bond via an oxygen atom in between. If the silicon atom is replaced by a hydrogen atom, this structure is called hydrogen bridge. The four states of the hydrogen bridge are shown in Figure 3.3.

In the first state a silicon atom has one dangling bond and the neighboring silicon atom has bonds to three oxygen atoms and one hydrogen atom. When a hole is captured, the hydrogen forms a bond, a "bridge" between the silicon atoms. This is the positively charged metastable configuration. In the positively charged stable configuration the

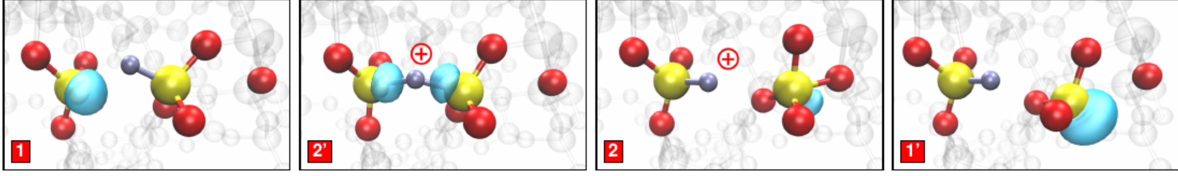


Figure 3.3: DFT results illustrating the four states of a hydrogen bridge. [101]

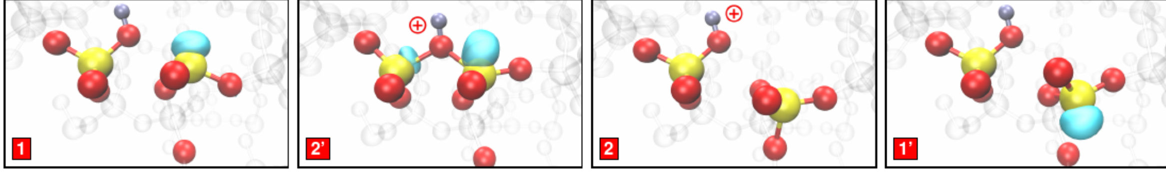


Figure 3.4: DFT results illustrating the four states of a hydroxyl E' center. [101]

silicon atom has moved through the plane of oxygen atoms and bonded to the oxygen atom at the back. The bonding to the silicon atom at the back is called puckering. If the bond at the back breaks and the silicon has instead a dangling bond, but is still in the puckered configuration, the metastable neutral state is reached [101].

### 3.1.3 Hydroxyl E' Center

The hydroxyl E' center shows a similar structure as the hydrogen bridge. The main difference is that the hydrogen atom is now bonded to an oxygen atom instead of silicon, forming a hydroxyl group. This defect type in all four states is shown in Figure 3.4.

In the stable neutral state one silicon atom carries the hydroxyl group and the other silicon atom has a dangling bond. In the metastable positive configuration, the silicon atoms bond via the oxygen atom. In states 2 and 1' the second silicon atom is again in a puckered configuration [101].

## 3.2 Hysteresis of Transfer Characteristics

Typically transfer characteristics ($I_D(V_G)$) of devices with a two-dimensional material as a channel, exhibit a hysteresis [107, 75, 108, 109, 110, 111, 112]. This means that the first sweep of the transfer characteristic, going for example from negative to positive voltages, reaches saturation current at a different voltage compared to the second sweep going from positive to negative voltages. Poission's equation relates any voltage shift, being basically a change in the effective potential($\varphi$), to a changed charge density($\rho$), (Equation (3.1)).

$$-\Delta\varphi(t) = \frac{\rho(t)}{\epsilon} \tag{3.1}$$

Therefore, if there was simply a stationary current flow through the channel of the device and a fixed amount of stationary charges distributed over the whole channel region, not

interacting with the channel at all, then no hysteresis could be observed. So, because we observe a hysteresis there has to be an interaction between charge traps in the channel region and the charge carriers moving along the channel. Namely, charges have to be injected into the channel or immobilized from the channel onto a fixed place, thereby leading to a creation or an annihilation of a fixed charge.

All regions in the vicinity of the channel can hold fixed charges. The region where the fixed charge is located defines the interaction mechanism of the charge with the current through the channel, thereby defining the time constants. In a back gated transistor, with silicon dioxide as a gate dielectric and an $MoS_2$ single layer as a channel (the devices studied in this work (see section 2.6)), there are four possible locations for trapped charges. Charges can be found in the oxide, at the interface between channel and oxide. Charges can accumulate at grain boundaries or other imperfections inside the channel material itself and charges can be located on molecules being adsorbed to the surface.

The question is, which of these charges are responsible for the hysteresis. In order to measure a hysteresis, the respective charge trapping/ de-trapping mechanism has to have a time constant in the order of the time needed for one complete up and down sweep of the transfer characteristic. The respective sites have to become charged/ discharged during the up sweep and have to remain in this state during the down sweep. If the charges become charged during the up sweep and discharge during the down sweep, there is no hysteresis. This is the case for a trapping mechanism with very short time constants. If, on the other hand, most sites do not change their charge state during one sweep, due to very long time constants, there is no hysteresis as well. The total sweep time $T$ was varied in this work between 20 ms and 400 s. The largest hysteresis was observed for the longest sweep time of 200 s.

I argue here in accordance with our previously published results [112], that the hysteresis is mainly due to the trapping and de-trapping of charges in the oxide and partially due to charge exchange with molecules adsorbed to the top of the $MoS_2$ single layer.

Some other groups attribute the hysteresis to interface traps [108, 110, 109]. Still, in the Shockley-Read-Hall model (see section 4.3), which is a common model to describe the effect of interface traps, the time constants for trapping events are in the order of microseconds. These time constants are too small to explain the existence of a hysteresis at a sweep time of 200 s.

The interaction with grain boundaries and other imperfections of the $MoS_2$ single layer is not thoroughly studied yet. Shu et al. [111] observed that these imperfections probably have an impact, but did not explain the mechanism of charge accumulation in the channel. What is more, Shu et al. [111] did not provide the pressure they term as vacuum, which is why there might still be some influence from adsorbed molecules which was not accounted for in their work. Therefore, they might have overestimated the influence of intrinsic defects. I believe that these defects have a rather small impact due to presumably small time constants.

The interaction with adsorbed molecules certainly has an impact on the hysteresis, as already observed by several groups [107, 75]. Late et al. [75] identified the charge exchange with adsorbed water molecules as one cause of the hysteresis. Therefore, it is

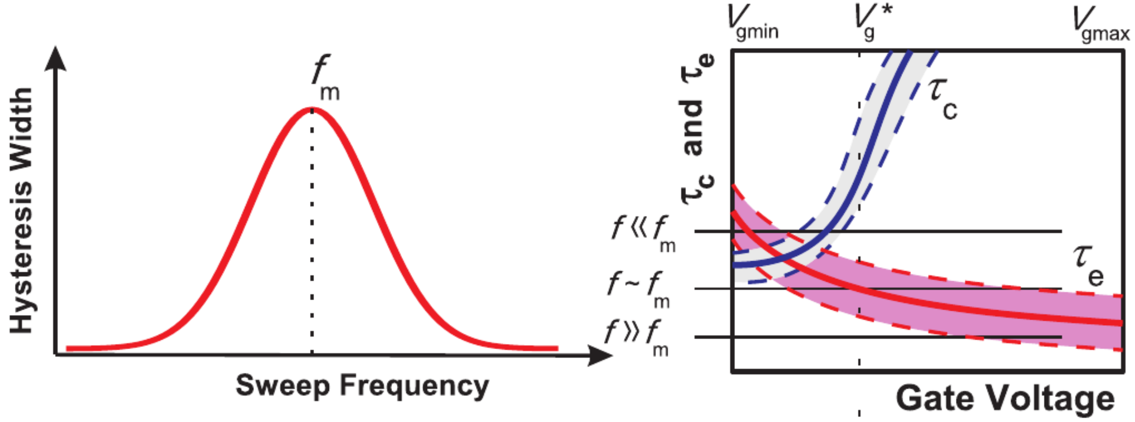


Figure 3.5: Schematic illustrating the frequency dependence of the hysteresis. $f_\mathrm{m}$ is the frequency, where the hysteresis width is the greatest. $V_\mathrm{gmin}, V_\mathrm{gmax}$ are the boundaries of the voltage sweep range and $V_\mathrm{g}^*$ denotes the threshold voltage. [112]

important to perform the measurements on back gated, not encapsulated $MoS_2$ transistors, under controlled conditions in vacuum. Still, even under controlled conditions in vacuum, at least a monolayer of molecules remains adsorbed to the surface and the behavior of our devices at higher temperatures points towards a partial annealing of the traps associated with the hysteresis, which could be explained by a partial desorption of molecules from the surface [112].

Finally, Illarionov et al. [112] showed that the trapping of charges in the oxide has exactly the right time constants to explain the phenomenon of hysteresis. The dependence of the hysteresis width on the sweep frequency shows a maximum at a certain frequency, with the frequency being defined as $1/T$. This maximum can be described naturally when relating the total sweep time $T$ to the voltage dependences of capture and emission times $\tau_\mathrm{c}$ and $\tau_\mathrm{e}$, which can be derived from the NMP model (see Section 4.4). The NMP model describes the interaction of charge carriers in the channel with the oxide defects described in Section 3.1. For very slow sweeps at low frequencies both capture and emission time constants are small, thus the traps become charged during one sweep and discharged during the other, leading in effect to no hysteresis. At moderate frequencies the emission time constants are small and get even smaller for increasing gate voltages. Thus, on the up sweep holes are emitted or electrons captured leading to a neutralization of defects, which have been charged in equilibrium. But the capture time constants are rather large, thus most traps remain neutral during the down sweep. A hysteresis will be observed accordingly. At very high frequencies both capture and emission time constants are large compared to the sweep times, essentially leading to no capture or emission events during sweeps and, consequently, to no hysteresis. This behavior is illustrated in Figure 3.5.

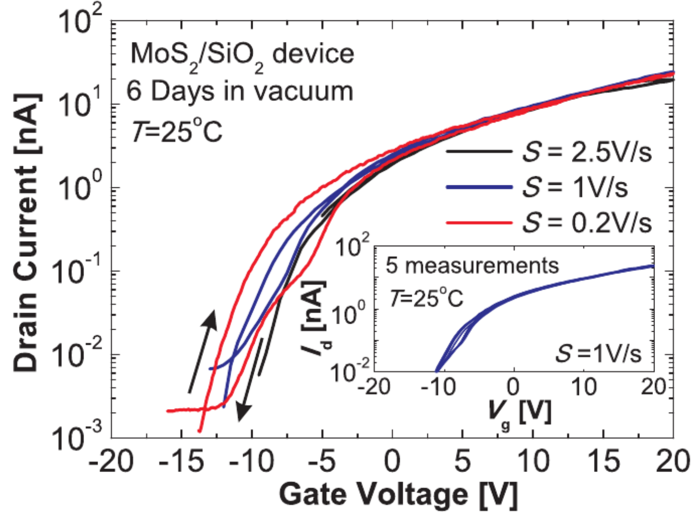


Figure 3.6: Hysteresis measurement data obtained for different sweep rates $S$ on our device (device A). The inset shows the stability of the measured hysteresis for a constant sweep rate. [112]

### 3.2.1 Measurement Setup

The measurements of the $I_\mathrm{D}(V_\mathrm{G})$ characteristics were carried out in vacuum ($5 \times 10^{-6}$ – $5 \times 10^{-5}$ torr). The sweep ranges spanned from $-20\,\mathrm{V}$ to $20\,\mathrm{V}$, at first always an up sweep from negative to positive voltages was performed, which was followed by a down sweep in the reverse direction. The sweep rate $S = V_\mathrm{step}/t_\mathrm{step}$ was varied from $0.2\,\mathrm{V/s}$ to $4000\,\mathrm{V/s}$ by changing the sampling time $t_\mathrm{step}$ and the step voltage $V_\mathrm{step}$. The total sweep time $T$ is given by multiplying the number of voltage step points $N = 2\left((V_\mathrm{gmax} - V_\mathrm{gmin})/V_\mathrm{step} + 1\right)$ with the sampling time $t_\mathrm{step}$. The hysteresis width in volt was extracted at the threshold voltage, which was defined via a constant current criterion. Typical hysteresis measurements can be seen in Figure 3.6.

Additionally, one distinguishes between PBTI- and NBTI-like hysteresis. An additional positive charge in the oxide decreases the flatband voltage and thereby the threshold voltage by an amount given in Equation (3.2), with $C^*_\mathrm{ox}$ being the capacitance per unit area and $d_\mathrm{ox}$ the total oxide thickness [109].

$$\Delta V_\mathrm{th} = -\frac{1}{C^*_\mathrm{ox}} \int_0^{d_\mathrm{ox}} \frac{x}{d_\mathrm{ox}} \rho(x)\,\mathrm{d}x \tag{3.2}$$

The variable $x$ in this integral runs from the channel interface to the gate of the device. In a PBTI-like hysteresis the down sweep is shifted towards higher voltages, corresponding to a neutralization of positive charges and in NBTI-like hysteresis the down sweep is shifted towards lower voltages corresponding to a creation of additional positive charges.

## 3.3 Bias Temperature Instabilities

Bias Temperature Instabilities (BTI) term the shift of transistor parameters due to higher gate voltages and higher transistor temperatures at low drain/source voltages [113]. The threshold voltage shift is used as a quantitative indicator for degradation and higher gate voltages and higher transistor temperatures serve the purpose of accelerating degradation, so that it becomes observable on reasonable time scales. Due to the low drain/source voltage, carriers are only moderately accelerated towards the drain, typically not acquiring enough energy to cause new defects. Degradation effects due to higher drain/source voltages are summarized under the term Hot Carrier Degradation (HCD).

The key characteristics of BTI can be described based on the phenomenologically classified border traps. Border traps are oxide traps, like those described in section 3.1, being situated close to the interface [114].

It is often observed that a device which was stressed using high biases or temperature, does not fully recover even after long measurement times. Some of the threshold voltage shift is permanent, which simply means that some of the degradation effects have much longer recovery times than any reasonable measurement time. This phenomenon is termed "permanent component" of BTI and the description of these effects is beyond the scope of this work [115].

In general, one distinguishes between negative bias temperature instabilities (NBTI), if the applied gate voltage is negative, and positive bias temperature instabilities (PBTI), if the applied gate voltage is positive. Naturally, NBTI is more important for p-MOSFETs and PBTI is more important for n-MOSFETs. Still, both stress types can be measured on both devices.

Contrary to the hysteresis, which is not observed on silicon devices, BTI has already been reported 50 years ago and has been thoroughly studied for standardized silicon technology [116, 117]. Therefore, measurement methods and theoretical description of BTI is quite mature in comparison to the description of hysteresis. In the following the most general techniques for measuring BTI are discussed and a short overview over some of the most popular visualisation methods like the captue-emission-time map is given, before the measurement procedure employed in this work is described.

### 3.3.1 Measure-Stress-Measure Technique

Using the measure-stress-measure (MSM) technique, the shift of the threshold voltage during stress and recovery $V_{\mathrm{th}}(t)$ can be obtained. First, the drain current at a specified reference voltage $V_{\mathrm{G}}^{\mathrm{L}}$ close to the threshold voltage $V_{\mathrm{th}}$ is measured. In the subsequent stress phase the gate voltage is set to $V_{\mathrm{G}}^{\mathrm{H}}$, but no measurements are carried out at this high gate voltage. During stress the gate voltage is switched to $V_{\mathrm{G}}^{\mathrm{L}}$ for short time intervals to measure $I_{\mathrm{D}}(V_{\mathrm{G}}^{\mathrm{L}})$. From the variations in the drain current at $V_{\mathrm{G}}^{\mathrm{L}}$ the threshold voltage shift is obtained. During the recovery cycle the gate contact can either be left floating or constantly pinned to $V_{\mathrm{G}}^{\mathrm{L}}$. In both cases again $V_{\mathrm{G}}^{\mathrm{L}}$ is applied during short time intervals for each measurement point [118].

Alternatively to measuring the drain current at a specified level $V_G^L$, a certain drain current $I_D$ can be enforced through the device, which enables a direct measurement of the threshold voltage shift $\Delta V_{th}$. Another possibility to extract the threshold voltage shift is to perform a whole $I_D(V_G)$ sweep at each measurement point and to obtain the respective threshold voltage by applying a constant current criterion, for example This last method can determine the threshold voltage most accurately but at the same time introduces the largest time delay $\Delta t_{delay}$ at each measurement point and additionally affects the degradation.

Even if the measurements are done with a minimum time delay $\Delta t_{delay}$, the part of $\Delta V_{th}$ with very short time constants already recovers during the interruptions of the stress period and, therefore, cannot be measured with this method.

### 3.3.2 On-the-Fly Measurement

In on-the-fly (OTF) measurements the problem encountered when using MSM technique (see Section 3.3.1) is avoided by measuring the drain current directly at high voltage level $V_G^H$ during stress. This requires a mapping of the drain current measured in the linear regime $I_D = I_D(V_G^H)$ to the drain current at the reference level $I_{D0} = I_D(V_G^L)$. Several methods have been developed for this mapping process, in the simplest form, this mapping can be done by applying Equation (3.3) to calculate the threshold voltage shift [118].

$$\Delta V_{th} \approx \frac{I_D - I_{D0}}{I_D}(V_G^H - V_G^L) \tag{3.3}$$

### 3.3.3 Capture-Emission-Time Map

The capture-emission-time (CET) map is a method for extracting and visualizing the distribution of the capture and emission time constants of defects in a device from the measured recovery curves $\Delta V_{th}(t_s, t_r)$ for different recovery and stress times. Contrary to TDDS, which is described in Section 3.1.1 and works only on small devices, a CET map can also be generated for large area devices, where the recovery curves contain information about a defect ensemble.

The CET map is the visual representation of the density $g({\tau_c}^H, {\tau_e}^L)$ of voltage step heights, corresponding to traps, with a certain capture time ${\tau_c}^H$ at high voltage level $V_G^H$ and a certain emission time ${\tau_e}^L$ at low voltage level $V_G^L$. To the total shift in the threshold voltage after a stress phase with stress time $t_s$ and a recovery phase with recovery time $t_r$, all traps contribute which have an emission time constant at low voltage level longer than the recovery time ${\tau_e}^L > t_r$ and a capture time constant at high level shorter than the stress time ${\tau_c}^H < t_s$. Briefly, only those traps can contribute, which have been charged by hole capture during the stress phase but not discharged during the recovery phase. This relation between the trap density $g$ and the total voltage shift $\Delta V_{th}$ is given in Equation (3.4) [105].

$$\Delta V_{th}(t_s, t_r) \approx \int_0^{t_s} d\tau_c \int_{t_r}^{\infty} d\tau_e g(\tau_c, \tau_e) \tag{3.4}$$

Inversely the trap density can be obtained from several measurements of the threshold voltage shift $\Delta V_{\mathrm{th}}(t_{\mathrm{s}}, t_{\mathrm{r}})$ over large intervals of stress and recovery times, by forming the second derivative (see Equation (3.5)) [105]. Here, for every different stress time $t_{\mathrm{s}}$ a new measurement has to be performed, where the recovery trace for the whole recovery time span is recorded.

$$g(\tau_{\mathrm{c}}, \tau_{\mathrm{e}}) \approx -\frac{\partial^2 \Delta V_{\mathrm{th}}(\tau_{\mathrm{c}}, \tau_{\mathrm{e}})}{\partial \tau_{\mathrm{c}} \partial \tau_{\mathrm{e}}} \tag{3.5}$$

In Figure 3.7 one can see typical recovery curves, as they were measured for different stress times $t_{\mathrm{s}}$ and the CET map, which was calculated from the recovery traces. The other way round, by integrating the CET map one could again obtain the measurement curves [105].

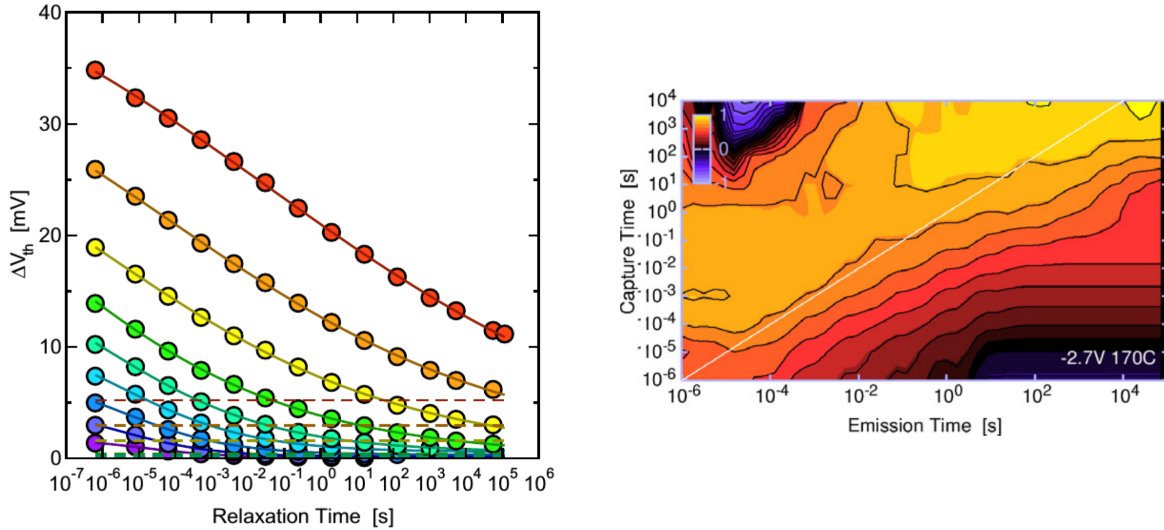


Figure 3.7: Typical measured threshold voltage shifts $\Delta V_{\mathrm{th}}(t_{\mathrm{s}}, t_{\mathrm{r}})$ and obtained CET Map. [105]

### 3.3.4 Measurement Setup

In this work a MSM technique was applied to measure BTI on the back-gated $MoS_2$ based transistors. The measurements were again performed in vacuum ($5 \times 10^{-6}$ – $5 \times 10^{-5}$ torr). The device was stressed by applying $V_{\mathrm{G}}^{\mathrm{H}} = \pm 20\,\mathrm{V}$ ($\pm 15\,\mathrm{V}/\pm 10\,\mathrm{V}/\pm 5\,\mathrm{V}$) for different time spans at different temperatures. Measurements were done only during the recovery cycles. At each measurement point the full $I_{\mathrm{D}}(V_{\mathrm{G}})$ characteristic was recorded, introducing a time delay of $\Delta t_{\mathrm{delay}} \approx 3\,\mathrm{s}$. Between the measurements the gate contact was left at a floating potential, to avoid additional stressing of the devices.

# CHAPTER 4 Modeling

The main part of this work was to model the characteristics of our $MoS_2$ devices, which were measured as described in Sections 3.2.1 and 3.3.4. The numerical simulations provide insights in the physical processes involved. This chapter is devoted to explain and justify the models which were used for these calculations.

At first, the common drift-diffusion-model will be explained and the applicability to transistors based on two-dimensional materials will be discussed. This model is classical, therefore, any quantum mechanical corrections, which have to be done due to lateral confinement, will be described in the following. The third section is devoted to describing the interaction of charges with interface traps using the Shockley-Read-Hall model and in the last part the nonradiative multiphonon (NMP) theory, necessary for modeling the interaction of charges with traps in the oxide, is outlined.

## 4.1 Drift-Diffusion-Model

The drift-diffusion-model consists of three coupled differential equations for the electrostatic potential $\varphi(\mathbf{r}, t)$, the electron density $n(\mathbf{r}, t)$ and the hole density $p(\mathbf{r}, t)$. The first equation is the Poisson equation (4.1) describing the electrostatics of the system. Here $C(\mathbf{r})$ stands for the concentration of dopants and ionized impurities. The second and the third equation are continuity equations for electrons and holes (Equations (4.2), (4.3)). These three equations are also often termed as basic semiconductor equations.

$$\Delta\varphi(\mathbf{r}, t) = q\left(n(\mathbf{r}, t) - p(\mathbf{r}, t) - C(\mathbf{r})\right)/\epsilon(\mathbf{r}) \tag{4.1}$$

$$\nabla \cdot \mathbf{J}_{\mathrm{n}}(\mathbf{r}, t) - q\frac{\partial n(\mathbf{r}, t)}{\partial t} = qR(n(\mathbf{r}, t), p(\mathbf{r}, t)) \tag{4.2}$$

$$\nabla \cdot \mathbf{J}_{\mathrm{p}}(\mathbf{r}, t) + q\frac{\partial p(\mathbf{r}, t)}{\partial t} = -qR(n(\mathbf{r}, t), p(\mathbf{r}, t)) \tag{4.3}$$

In these equations $\mathbf{J}_{\mathrm{n}}(\mathbf{r}, t)/\mathbf{J}_{\mathrm{p}}(\mathbf{r}, t)$ denotes the electron/hole current and $R(n(\mathbf{r}, t), p(\mathbf{r}, t))$ describes the generation and recombination of charge carriers. The currents are modeled using drift-diffusion relations (Equations (4.4), (4.5)). Here $V_{\mathrm{T}} = k_{\mathrm{B}}T/q$ denotes

the thermal voltage.

$$\mathbf{J}_\mathrm{n}(\mathbf{r},t) = -q\mu_\mathrm{n}^\mathrm{eff}\left(n(\mathbf{r},t)\nabla\varphi(\mathbf{r},t) - V_\mathrm{T}\nabla n(\mathbf{r},t)\right) \tag{4.4}$$

$$\mathbf{J}_\mathrm{p}(\mathbf{r},t) = -q\mu_\mathrm{p}^\mathrm{eff}\left(p(\mathbf{r},t)\nabla\varphi(\mathbf{r},t) + V_\mathrm{T}\nabla p(\mathbf{r},t)\right) \tag{4.5}$$

The first term is the drift term or simply Ohm's law, stating that the current is proportional to the local electric field and the second term is the diffusion term, stating that the current compensates local gradients in the charge carrier density. For the diffusion coefficients the Einstein relation was used (Equation (4.6)).

$$D_{n/p} = \frac{k_\mathrm{B}T}{q}\mu_{n/p}^\mathrm{eff} = V_\mathrm{T}\mu_{n/p}^\mathrm{eff} \tag{4.6}$$

In these equations the effective mobilities $\mu_n^\mathrm{eff}/p$ have been used, which in two-dimensional materials are in general not the same as the intrinsic mobilities, as described in sections 2.4 and 2.5. These equations were formulated 60 years ago [119]. They can be either derived from simple classical considerations or by calculating the first moment of the Boltzmann Transport Equation. What made these equations so successful when it comes to the modeling of semiconductor devices, is the computationally very efficient and numerically extremely stable discretization method of Scharfetter and Gummel [120].

Using the discretization scheme of Scharfetter-Gummel, together with a box-integration method and a backward Euler-scheme on a two-dimensional grid, leads to the following set of equations (Equations (4.7) - (4.11)). The index i refers to the current box, the index j is the summation index, with the sums running over all adjacent boxes and finally the index k gives the time step. $d_{ij}$ is the distance between adjacent points of the grid and $A_{ij}$ is the boundary length between adjacent boxes, while $V_i$ is the area of the current box. $\Delta t$ is the length of one time step and $\Delta_{ijk} = (\varphi_{jk} - \varphi_{ik})/V_\mathrm{T}$ gives the potential difference between neighbouring points. $\mathcal{B}(x) = x/(\mathrm{e}^x - 1)$ is the Bernoulli function.

$$-\sum_{j\in N_i}\epsilon_{ij}\frac{\Delta_{ijk}V_\mathrm{T}}{d_{ij}}A_{ij} = q(n_{ik} - p_{ik} - C_i)V_i \tag{4.7}$$

$$\sum_{j\in N_i} J_{\mathrm{n}ijk}A_{ij} - q\frac{n_{ik} - n_{ik-1}}{\Delta t}V_i = qR_{ik}V_i \tag{4.8}$$

$$\sum_{j\in N_i} J_{\mathrm{p}ijk}A_{ij} + q\frac{p_{ik} - p_{ik-1}}{\Delta t}V_i = -qR_{ik}V_i \tag{4.9}$$

$$J_{\mathrm{n}ijk} = \frac{q\mu_\mathrm{n}^\mathrm{eff}V_\mathrm{T}}{d_{ij}}\left(n_{jk}\mathcal{B}(\Delta_{ijk}) - n_{ik}\mathcal{B}(-\Delta_{ijk})\right) \tag{4.10}$$

$$J_{\mathrm{p}ijk} = -\frac{q\mu_\mathrm{p}^\mathrm{eff}V_\mathrm{T}}{d_{ij}}\left(p_{jk}\mathcal{B}(-\Delta_{ijk}) - p_{ik}\mathcal{B}(\Delta_{ijk})\right) \tag{4.11}$$

This set of equations is explicitly non-linear due to the Bernoulli function and implicitly non-linear as the carrier densities depend on the local potential via a Boltzmann factor.

It is solved by the simulator in each step on all grid points using a Newton iteration. In this way this set of equations is implemented in Minimos-NT, the simulator used for all simulations in this work [121]. For simulations a cut along the channel of the devices was made, assuming that the device is completely uniform in the width direction. In this cut the device looks like Figure 2.11(a). The dimensions given in Section 2.6 were used for modeling and an orthogonal grid on the sections of $MoS_2$ and $SiO_2$ was chosen for simplicity. The metal contacts were modeled as Ohmic contacts (see Section 2.5) and therefore can be implemented using Dirichlet boundary conditions.

The question remains whether this classical, macroscopic model can be applied for describing transistors with 2D channels. In principle the Drift-Diffusion model or, more general, the Boltzmann Transport Equation remains valid as long as the mean free carrier path is very small compared to the typical dimensions of the transistor (width $W$ and length $L$). In this case charge transport is dominated by scattering mechanisms. In our case this condition is fulfilled as the dimensions are on the micrometer range and assuming average quality of the channel material, scattering events take place every few tens of nanometers. If, on the other hand, the dimensions of the devices become very small, if there are nearly no defects in the channel region and if the transistor operates at low temperatures, strongly reducing the amount of phonon scattering, ballistic transport models have to be used.

There are various works demonstrating that the drift diffusion model can be successfully applied to low dimensional structures in the scattering limit in general [122, 123], or to two-dimensional layers of $MoS_2$ [77, 124]. Some of them [123, 77] however discuss that the drift-diffusion-model neglects quantum mechanical effects completely. Still, there certainly is a considerable quantum confinement along the z-direction in a monolayer Therefore, some corrections, which might be introduced to account for this confinement, shall be discussed in the next section.

## 4.2 Quantum Mechanical Corrections

The effect of quantum confinement is that the three dimensional density of states (DOS) has to be replaced by its two-dimensional counterpart. When solving the Boltzmann Transport Equation in the stationary case ($\Delta t \to \infty$) one obtains the following expression for the electron density

$$n_{\mathrm{3D}} = \sum_i \int_{E_{\mathrm{C}}}^{\infty} g^i_{\mathrm{3D,n}}(E) f_{\mathrm{n}}(E + E_i) \mathrm{d}E. \tag{4.12}$$

Here $f(E)$ is the Fermi-Dirac Distribution (Equation (4.13)) and $g_{\mathrm{3D}}(E)$ the three dimensional density of states.

$$f_{\mathrm{n}}(E) = \frac{1}{1 + \exp\left(\frac{E - E_{\mathrm{F}}}{k_{\mathrm{B}}T}\right)} \tag{4.13}$$

If one approximates the minimum of the conduction band with a parabola, one obtains the effective mass $m^*_{\mathrm{e}}$ according to Equation (2.18) and a quadratic dispersion relation

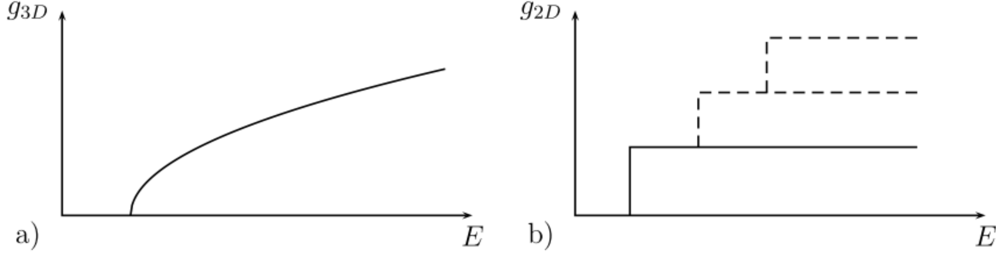


Figure 4.1: Comparison of 3D and 2D density of states. Higher energy bands are indicated by dashed lines. [77]

$E = (\hbar^2 k^2)/(2m_e^*)$. Using this dispersion relation the three dimensional density of states can be obtained as

$$g^i_{3\mathrm{D,n}}(E) = \frac{\nu^i (m_e^*)^i \sqrt{2(m_e^*)^i E}}{\pi^2 \hbar^3}. \tag{4.14}$$

In this expression $\nu$ stands for the degree of degeneration of the band.

In analogy to these expressions in two dimensions the electron density per area (surface electron density $n^S$) is given by Equation (4.15).

$$n^S_{2\mathrm{D}} = \sum_i \int_{E_\mathrm{C}}^{\infty} g^i_{2\mathrm{D,n}}(E) f(E + E_i) \mathrm{d}E \tag{4.15}$$

Here the outer sum runs over all bands contributing to the total carrier density with $E_i$ denoting the band edges of the respective bands. As the band structure of a monolayer $MoS_2$ is in principle similar to the band structure of classical three dimensional semiconductors like GaAs, the band structure can again be approximated by a parabola in the minimum. Using this quadratic dispersion, expression (4.16) for the two-dimensional density of states follows.

$$g^i_{2\mathrm{D,n}} = \frac{\nu^i (m_e^*)^i}{\pi \hbar^2} \tag{4.16}$$

In Figure 4.1 a comparison between the three dimensional and the two-dimensional density of states is given. Considering the capacitance at the gate $C_\mathrm{G}$, not only the capacitance of the oxide $C_\mathrm{ox}$ but also an additional contribution due to quantum confinement has to be considered, the so called quantum capacitance $C_\mathrm{q}$. [77]

$$\frac{1}{C_\mathrm{G}} = \frac{1}{C_\mathrm{ox}} + \frac{1}{C_\mathrm{q}} \tag{4.17}$$

$$C_\mathrm{q} = q^2 \frac{\partial n^S}{\partial E_\mathrm{F}} \tag{4.18}$$

Thiele [77] studied the impact of the two-dimensional density of states on the charge carrier density $n$ and on the quantum capacitance $C_\mathrm{q}$. He showed that the differences in the charge carrier density are in general small, and, to account for the discrepancies

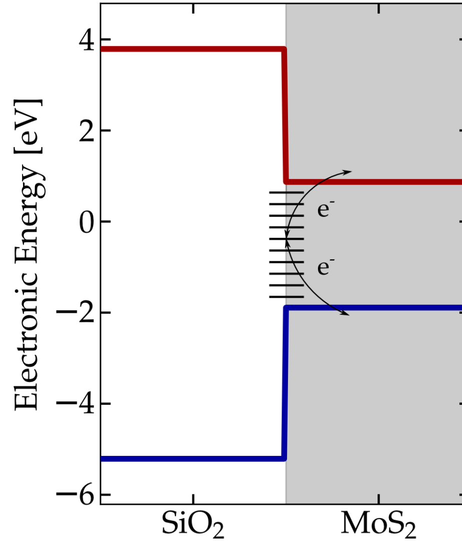


Figure 4.2: Schematic Drawing illustrating recombination via interface traps.

in the quantum capacitance, he proposed to multiply the effective mass $m_e^*$ with a correction factor of 3.0. In my work the capacitance is not explicitly studied, only the charge densities are important for simulating current-voltage characteristics. Therefore, the impact of the quantum mechanical correction factor of 3.0 is very small and is neglected.

Ancona [123] reported also a large impact of the modified density of states in Graphene transistors. However, this is mainly due to the change in the dispersion relation, which is linear in the case of Graphene and therefore completely different from any conventional semiconductor.

The correction due to a two-dimensional density of states is probably negligible when simulating current voltage characteristics. For modern devices in silicon technology the localization of charges in the inversion layer is very high, such that in this case as well the usage of a two-dimensional density of states is more reasonable [125]. Still simulations with the drift diffusion model and a three dimensional density of states give good results.

## 4.3 Interface States

In general, defects are assumed to be located at interfaces between semiconductors and oxides, creating energy states inside the band gap [126]. These states act as recombination centers for charge carriers as illustrated in Figure 4.2. In this work I model the recombination processes via defect states at the interface using the Shockley-Read-Hall (SRH) expression describing phonon assisted recombination.

In a non-degenerate semiconductor at thermal equilibrium the Fermi-Dirac distribution for electrons and holes can be approximated using Boltzmann statistics, obtaining

the following equilibrium concentrations for electrons $n_0$ (4.19) and holes $p_0$ (4.20).

$$n_0 = N_\mathrm{c}(T)\exp\left(\frac{E_\mathrm{F} - E_\mathrm{C}}{k_\mathrm{B}T}\right) \tag{4.19}$$

$$p_0 = N_\mathrm{v}(T)\exp\left(\frac{E_\mathrm{V} - E_\mathrm{F}}{k_\mathrm{B}T}\right) \tag{4.20}$$

In these expressions $N_\mathrm{c}$ and $N_\mathrm{v}$ are the effective densities of states which have been obtained by integrating Equation 4.12 using the three dimensional density of states. The effective densities of states are given in Equations (4.21) and (4.22) with $N_0$ summarizing all physical constants and the degree of degeneration of the conduction band $M_\mathrm{C}$.

$$N_\mathrm{C} = 2\left(\frac{2\pi m_\mathrm{n}^* k_\mathrm{B}T}{\hbar^2}\right)^{\frac{3}{2}} M_\mathrm{C} = N_0 M_\mathrm{C}\left(\frac{m_\mathrm{n}^*}{m_0}\cdot\frac{T}{300K}\right) \tag{4.21}$$

$$N_\mathrm{V} = 2\left(\frac{2\pi m_\mathrm{p}^* k_\mathrm{B}T}{\hbar^2}\right)^{\frac{3}{2}} = N_0\left(\frac{m_\mathrm{p}^*}{m_0}\cdot\frac{T}{300K}\right) \tag{4.22}$$

By multiplying the equilibrium concentrations for electrons and holes one obtains the intrinsic carrier concentration $n_\mathrm{i}$,

$$n_\mathrm{i} = n_0 p_0 = \sqrt{N_\mathrm{C}N_\mathrm{V}}\exp\left(-\frac{E_\mathrm{G}}{2k_\mathrm{B}T}\right). \tag{4.23}$$

Phonon assisted generation and recombination processes always work towards establishing a thermal equilibrium. Thus, if the product of carrier densities is larger than the intrinsic carrier concentration recombination dominates while if it is the other way around generation dominates. Generation and recombination are two sides of the same phenomenon. From now on I will stick to the term recombination which can always be replaced by generation, only that charge is in one case created and in the other one annihilated, leading to different signs of the rate, when inserted into Equations (4.2) and (4.3).

The SRH recombination rate is derived by writing down balance equations for electron/hole capture and emission processes in the presence of a defect state with energy $E_\mathrm{t}$. The SRH rate is given by [127]

$$R^\mathrm{SRH} = \frac{np - n_\mathrm{i}}{(n + n_1)/S_\mathrm{p} + (p + p_1)/S_\mathrm{n}}. \tag{4.24}$$

This recombination rate is inserted into the continuity equations (4.2) and (4.3). $n_1$ and $p_1$ are auxiliary electron and hole densities. They are defined such that for a defect level in the mid gap, it holds that $n_1 = p_1 = n_\mathrm{i}$ and Equation (4.24) reaches its maximum.

$$n_1 = N_\mathrm{c}(T)\exp\left(\frac{E_\mathrm{t} - E_\mathrm{C}}{k_\mathrm{B}T}\right) \tag{4.25}$$

$$p_1 = N_\mathrm{v}(T)\exp\left(\frac{E_\mathrm{V} - E_\mathrm{t}}{k_\mathrm{B}T}\right) \tag{4.26}$$

The variables $S_\mathrm{p}$ and $S_\mathrm{n}$ are the recombination velocities of electrons and holes. They depend on the trap capture cross sections for electrons and holes $\sigma_\mathrm{n}$, $\sigma_\mathrm{p}$, the interface trap density $N_\mathrm{it}$ and the thermal velocities of electrons and holes $v_\mathrm{n}$, $v_\mathrm{p}$. As a reference temperature 300 K is used in Minimos-NT, therefore the thermal velocities are [121]

$$v_\mathrm{th,n,p} = \sqrt{\frac{3k_\mathrm{B}300\,\mathrm{K}}{m^*_\mathrm{n,p}}}. \tag{4.27}$$

The recombination velocities for electrons and holes are given in Equations (4.28), (4.29).

$$S_\mathrm{n} = \left(\frac{T}{300\,\mathrm{K}}\right)^{3/2} \sigma_\mathrm{n} N_\mathrm{it} v_\mathrm{n} \tag{4.28}$$

$$S_\mathrm{p} = \left(\frac{T}{300\,\mathrm{K}}\right)^{3/2} \sigma_\mathrm{p} N_\mathrm{it} v_\mathrm{p} \tag{4.29}$$

The carrier recombination via trap centers at the interface does not only have an impact on the charge carrier densities. Due to the recombination process a certain occupancy of the trap levels establishes. This occupancy corresponds to an effective charge located at the interface, which has to be included in the Poisson equation. In this respect one distinguishes between acceptor like traps and donor like traps. Donor like traps are neutral if an electron is located at the defect site, but are positively charged if there is no electron. Thus these defects are also called hole-traps. Acceptor like traps are negatively charged if an electron is located at the defect site, but neutral if there is no electron and are therefore also called electron-traps. This nomenclature also applies to defects in the oxide.

The occupancy function $f$ gives the probability for an electron to be located at the defect site. In the SRH model it has the form [127]

$$f = \frac{n/S_\mathrm{p} + p_1/S_\mathrm{n}}{(n+n_1)/S_\mathrm{p} + (p+p_1)/S_\mathrm{n}}. \tag{4.30}$$

The charge $Q$ of the traps at the interface for acceptor like traps is given in Equation (4.31) and for donor like traps in Equation (4.32).

$$Q = -fN_\mathrm{it}q \tag{4.31}$$

$$Q = (1-f)N_\mathrm{it}q \tag{4.32}$$

This charge enters the Poisson equation (Equation 4.7)) as an additional contribution to the constant $C_i$ in the respective box. The interface defects in our devices are donor like traps.

In this work the distribution of traps is modeled using a Gaussian distribution. Of this distribution one can specify the mean of the defect level $\overline{E_\mathrm{t}}$, the width of the distribution of defect levels $\sigma_\mathrm{t}$ and a cut-off of the distribution at the top and at the bottom ${E_\mathrm{t}}^\mathrm{max}$ and ${E_\mathrm{t}}^\mathrm{min}$. The defect levels are sampled on a discrete grid in the energy interval defined by ${E_\mathrm{t}}^\mathrm{max}$ and ${E_\mathrm{t}}^\mathrm{min}$.

In Table 4.1 the model parameters of the SRH model for interface states are summarized. The distribution of the trap levels and the interface trap density vary in the course of the simulations, but the capture cross section for electrons and holes remains always at the standard value of $\sigma_n = \sigma_p = 1 \times 10^{-15}\,\mathrm{cm}^2$.

| Model Parameter | Symbol | Unit/Standard Value |
|---|---|---|
| Trap Density | $N_{\mathrm{it}}$ | [cm$^{-2}$] |
| Mean Defect Level | $\overline{E_{\mathrm{t}}}$ | [eV] |
| Std. Deviation of Defect Levels | $\sigma_{\mathrm{t}}$ | [eV] |
| Maximum Defect Level | $E_{\mathrm{t}}{}^{\mathrm{max}}$ | [eV] |
| Minimum Defect Level | $E_{\mathrm{t}}{}^{\mathrm{min}}$ | [eV] |
| Electron Capture Cross Section | $\sigma_n$ | $1 \times 10^{-15}\,\mathrm{cm}^2$ |
| Hole Capture Cross Section | $\sigma_p$ | $1 \times 10^{-15}\,\mathrm{cm}^2$ |

Table 4.1: Model parameters for the modeling of interface traps using the SRH model.

# 4.4 Oxide Defects

In this work I use a nonradiative multi phonon (NMP) model involving four states to describe the interaction of charge carriers with defects in the oxide. In Section 3.1 it is explained how the nature of defects in the amorphous silicon dioxide can be analyzed using TDDS. It is also argued that the observed phenomena can only be properly described in the framework of a four-state model. The effects of charge exchange between the defects (described in Sections 3.1.2 and 3.1.3) and conduction and valence band of the semiconducting channel are accurately explained using the four-state NMP model. This model is therefore the bridging element between the microscopic nature of defects as given in Section 3.1 and macroscopic measurements like hysteresis or BTI analysis (see Sections 3.2 and 3.3).

Only recently there were indications that the bias dependence of the conventional NMP model, which has been described in various publications ([103, 105, 125]), does not suffice to explain measurement data from recent BTI measurements on small devices [128]. This is probably due to very high electric fields in thin oxides of modern devices. In the devices studied in this work the maximum electric field in the oxide during hysteresis and BTI measurements amounts to $F_{\mathrm{OX}} \approx 2\,\mathrm{MV/cm}$. Even though this value is not that high, accurate modeling of the bias dependence is very important for the description of BTI and hysteresis effects. Therefore, an NMP model was used in this work which covers effects at elevated oxide fields as described in the following.

## 4.4.1 Configuration Coordinate Diagram

If an electron is captured in the oxide this process affects all surrounding electrons and nuclei. The movement of these particles is described by a Schrödinger equation, which is approximated using the Born-Oppenheimer approximation. This approximation separates the movement of the nuclei and of the electrons but in contrast to Section 2.3.2, where the movement of the electrons is of interest, in the NMP model, the movement of the nuclei on the multi-dimensional potential energy surface, defined by the average potential of the electrons, is important. The Schrödinger equation for the movement of nuclei on this 3N dimensional surface, with $N$ being the number of atoms, is given in

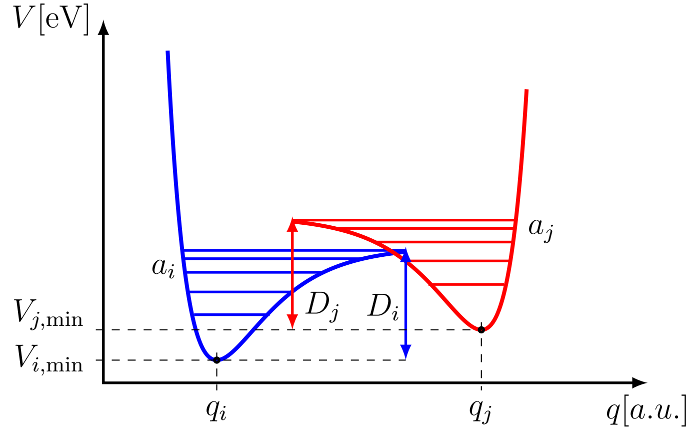


Figure 4.3: The system energy along the configuration coordinate is approximated by two Morse potentials.

Equation (4.33).

$$\left(\hat{T}_\mathrm{n} + E_{\mathrm{el},i}(\mathbf{R})\right) \psi_{n,j}(\mathbf{R}) = E_{n,i,j}\, \psi_{n,j}(\mathbf{R}) \tag{4.33}$$

The stable configuration of the whole system is given by the global energy minimum $V_{i,\min}$ of the potential energy surface described by $E_{\mathrm{el},i}(\mathbf{R})$. For a transition from this state to another state at the local energy minimum $V_{j,\min}$, only the path $q$ along the potential energy surface is of importance. This reaction path is called "reaction coordinate" $q$ and is used as x-axis in the so called configuration coordinate diagram. The total system energy $V(q)$ along the configuration coordinate can have an arbitrarily complex shape in general. Therefore, an approximation of this surface in vicinity to the minima is necessary. For sufficiently small displacements from the equilibrium position the potential energy can be approximated by a harmonic oscillator. However, for larger displacements there has to be an anharmonic contribution in the approximation to obtain good results. One possible method for approximating the potential energy in this case is by using a Morse potential. An exemplary configuration coordinate diagram is shown in Figure 4.3.

### 4.4.2 Morse Potential

Initially the Morse potential was developed by Philip Morse to describe the motions of the nuclei in a diatomic molecule [129]. The Morse potential energy function is of the form

$$V(R) = D\left(1 - \mathrm{e}^{-a(R-R_0)}\right)^2. \tag{4.34}$$

In this expression $R_0$ stands for the equilibrium bond distance, $D$ is the dissociation energy, measured between the bottom of the well $V_\mathrm{min}$ and the energy of unbound atoms, and the parameter $a$ gives the width of the well. In a Taylor expansion of (4.34) one obtains for the coefficient of the harmonic term $k = 2Da^2$. Therefore, the parameter $a$ is defined via the force constant $k$, $a = \sqrt{k/2D}$.

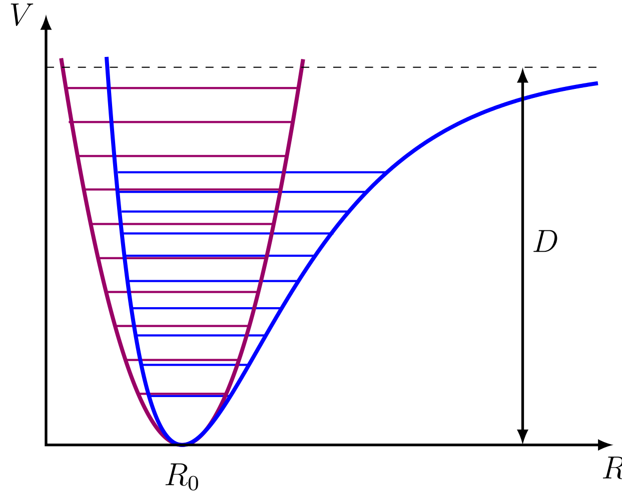


Figure 4.4: Comparison of Morse potential and parabolic potential.

The Schrödinger equation for the motion of two nuclei with the Morse potential as an interaction potential (Equation (4.35)) was solved by Morse [129]. Here $\mu$ gives the reduced mass of the system.

$$\left(-\frac{\hbar^2\nabla^2}{2\mu}+V(R)\right)\psi_n(R)=E_n\psi_n(R) \tag{4.35}$$

The eigenvalues are given by [129]

$$E_n=\hbar\omega\left(n+\frac{1}{2}\right)-\frac{\left(\hbar\omega\left(n+\frac{1}{2}\right)\right)^2}{4D}. \tag{4.36}$$

Here the frequency $\omega$ is defined via the force constant $\omega=\sqrt{k/\mu}$. The first term in Equation (4.36) is exactly the same as for a harmonic potential, only the second term assures that the spacing between subsequent energy levels is not constant anymore, but decreases with increasing quantum number $n$.

Figure 4.4 compares the Morse potential and the harmonic potential with their respective energy levels. The Morse potential has many advantages over the quantum harmonic oscillator. First, it includes bond breaking and the existence of unbound states. Second the band spacing and the transition probabilities between different quantum mechanical states are closer to reality in a Morse potential due to its anharmonicity. Since its first introduction the Morse potential has also been successfully applied to describe a covalent bond between two atoms in general, also for atoms in a crystal [130, 131].

Due to its advantages over the quantum harmonic oscillator and the proven applicability to covalent bonds inside crystals, the Morse potential was used to approximate the multi-dimensional potential energy surface in the vicinity of the minima $V_{i,\mathrm{min}}$ and $V_{j,\mathrm{min}}$ (Equations (4.37) and (4.38)).

$$V_i(q)=V_{i,\mathrm{min}}+D_i\left(1-\mathrm{e}^{-a_i(q-q_i)}\right)^2 \tag{4.37}$$

$$V_j(q)=V_{j,\mathrm{min}}+D_j\left(1-\mathrm{e}^{-a_j(q_j-q)}\right)^2 \tag{4.38}$$

Mata et al. [132] showed that the dissociation energy depends exponentially on the electric field $F$ in polar molecules. As the bonds between silicon and oxygen atoms are polar as well, a pre-factor for modeling the field dependence is included into the dissociation energy.

$$D_i = D_{i,0} 10^{k_F F} \tag{4.39}$$

The field dependence factor is defined via $k_F = 1/\mathrm{d}F$ with $\mathrm{d}F$ being the slope of the field dependence of the dissociation energy in a logarithmic plot.

### 4.4.3 Problem Specification

The NMP model describes the transition of an electron from an oxide trap to the conduction or valence band edge. In a general configuration coordinate diagram, the y axis denotes the energies of the whole system when changing its configuration from one state to another. It is now assumed that in a charge transfer process mainly the energy of the charge changes and the energies of all other components of the system remain roughly the same. Therefore, the constant energy of all remaining components $V_{\mathrm{sys}}$ can be subtracted from the energy minima in Equations (4.37) and (4.38), arriving at a description of the transition where only the energy of the transferred electron is considered.

Exemplarily in the following transitions between a donor-like trap and the conduction and valence band of the semiconductor will be studied. The three different states of the system are defined in analogy to reference [103]:

- In state $i$ the electron is located at the trap at distance $x_\mathrm{t}$ from the interface and the trap is neutral. The energy amounts to $E_\mathrm{t}(x_\mathrm{t}) = E_{\mathrm{t}0} - q_0\varphi(x_\mathrm{t})$.
- In state $j^\mathrm{V}$ the electron is located at the valence band edge at the interface and the trap is positive. The energy amounts to $E_\mathrm{V}(0) = E_{\mathrm{V}0} - q_0\varphi(x = 0)$.
- In state $j^\mathrm{C}$ the electron is located at the conduction band edge at the interface and the trap is positive. The energy amounts to $E_\mathrm{C}(0) = E_{\mathrm{C}0} - q_0\varphi(x = 0)$.

The energies are calculated using the electrostatic potential $\varphi(x)$, the energies of the trap level, and the band edges at flat band conditions.

The reference level for the electronic energy is defined in the middle of the band gap of the channel. The electric field inside the oxide is denoted with $F$. These definitions yield the following system energies [103].

$$V_{i,\mathrm{min}} = E_{\mathrm{t}0} + q_0 x_\mathrm{t} F \tag{4.40}$$

$$V^\mathrm{V}_{j,\mathrm{min}} = -1/2\,(E_{\mathrm{C}0} - E_{\mathrm{V}0}) \tag{4.41}$$

$$V^\mathrm{C}_{j,\mathrm{min}} = 1/2\,(E_{\mathrm{C}0} - E_{\mathrm{V}0}) \tag{4.42}$$

The dissociation energy for Si-O bonds varies between 4.3 eV and 8.3 eV depending on the exact bonding situation in the amorphous oxide [133, 134]. Therefore as a basic value for the dissociation energy $D_{i,0} = 5.5\,\mathrm{eV}$ is used. The slope of the dissociation constant as a function of the electric field is approximately $\mathrm{d}F = 50\,\mathrm{MV/cm}$ and the force constant

$k$ is given by $k = 1.6\,\mathrm{kg/s^2}$. Together with the remaining model parameters $R_{ij} = D_j/D_i$ and $\Delta q_{ij} = |q_j - q_i|$ and the definitions $q_i = 0$ and $q_j > 0$ (without loss of generality) the problem is now unambiguously defined.

Equations (4.43), (4.44) and (4.45) describe the Morse potentials between which NMP transitions take place. The dissociation energies are given by $D_i = D_{i,0}10^{k_F F}$ and $D_j = R_{ij} D_{i,0} 10^{k_F F}$ and the width parameter $a$ can be calculated using the force constant and the dissociation energy $a_{i,j} = \sqrt{k/\left(2D_{i,j}\right)}$.

$$V_i(q) = E_{\mathrm{t}0} + q_0 x_{\mathrm{t}} F + D_i \left(1 - \mathrm{e}^{-a_i q}\right)^2 \tag{4.43}$$

$$V_j^{\mathrm{V}}(q) = -1/2 \left(E_{\mathrm{C}0} - E_{\mathrm{V}0}\right) + D_j \left(1 - \mathrm{e}^{-a_j (\Delta q_{ij} - q)}\right)^2 \tag{4.44}$$

$$V_j^{\mathrm{C}}(q) = 1/2 \left(E_{\mathrm{C}0} - E_{\mathrm{V}0}\right) + D_j \left(1 - \mathrm{e}^{-a_j (\Delta q_{ij} - q)}\right)^2 \tag{4.45}$$

A corresponding configuration coordinate diagram for different electric fields is shown in Figure 4.5.

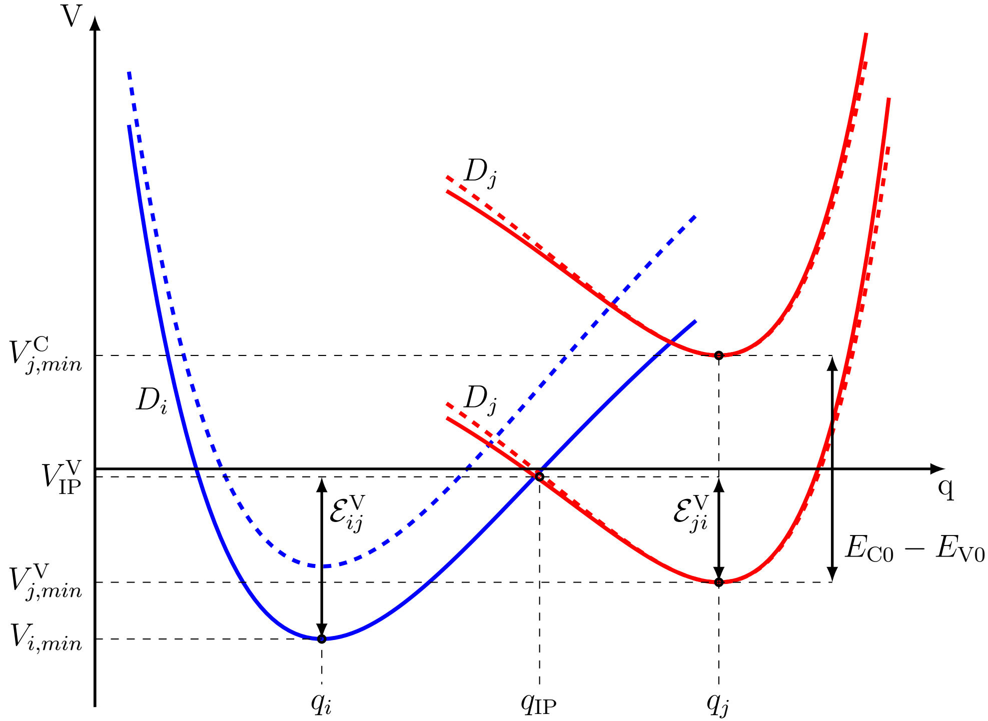


Figure 4.5: Schematic configuration coordinate diagram for an NMP transition, as specified in Equations (4.43) to (4.45). The dashed lines show the potentials with an increased electric field.

### 4.4.4 Single State Transitions

The transition rate for a transition from initial state $V_i(q)$ to final state $V_j^{\mathrm{V}}(q)$ can be derived from first-order time dependent perturbation theory using the Franck- Condon

approximation [125].

$$k_{ij} = A_{ij} f_{ij} \tag{4.46}$$

$$A_{ij} = \frac{2\pi}{\hbar} |\langle \psi_i | V_j | \psi_j \rangle| \tag{4.47}$$

$$f_{ij} = \operatorname*{ave}_{\alpha} \sum_{\beta} |\langle \psi_{i,\alpha} | \psi_{j,\beta} \rangle| \tag{4.48}$$

The first contribution of the transition rate is given by the electronic matrix elements $A_{ij}$ of the potential $V_j$ calculated in the eigenbasis of the one particle Hamiltonian using the expression $V_i$ as potential. Thus $V_j$ acts as a perturbation on the Hamiltonian of the initial states.

The second contribution is given by the lineshape function $f_{ij}$. It is calculated by forming the thermal average over all initial states of a sum running over the overlaps between the initial states $\psi_{i,\alpha}$ and the final states $\psi_{j,\beta}$. The overlaps are called Franck-Condon factor and are only non-zero, if the energies of the initial and the final state are the same. The quantum mechanical states $\psi_{i,\alpha}$ and $\psi_{j,\beta}$ are given by the solution of a one particle Schrödinger equation inside potential $V_i$ or potential $V_j$ respectively.

The wave functions $\psi_i, \psi_j$ in Equation (4.47) and the wave function $\psi_{i,\alpha}$ in Equation (4.48) are the wave functions of the electron at the trap site and $\psi_{j,\beta}$ is the wave function of the electron at the conduction or valence band edge. As the trap wave functions in Equation (4.47) are strongly localized, there is only one significant contribution at the trap site $x_\mathrm{t}$. Thus, the electronic matrix element can be approximated using a WKB factor $\lambda(E, x_\mathrm{t})$, to account for the tunneling of electrons with energy $E$ from the bands to the defect site at distance $x_\mathrm{t}$ from the interface.

$$A_{ij} \approx A_0 \lambda(E, x_\mathrm{t}) \tag{4.49}$$

The lineshape function has its largest contribution from energy levels close to the intersection point (IP). In the classical limit the lineshape function becomes a Dirac peak. The thermal average is calculated using the partition function $Z$ of the canonical ensemble. When considering for example the transition from state $i$ to state $j^\mathrm{V}$, the lineshape function becomes

$$f(V_i, V_j^\mathrm{V}) = Z^{-1} \int_{-\infty}^{\infty} \exp\left(-\frac{V_i(q')}{k_\mathrm{B}T}\right) \delta\big(V_i(q') - V_j^\mathrm{V}(q')\big) \mathrm{d}q'. \tag{4.50}$$

By definition the Dirac delta function vanishes everywhere except for

$$V_i(q) - V_j^\mathrm{V}(q) = 0. \tag{4.51}$$

So, assuming that $q_\mathrm{IP}$ solves this equation, the lineshape function evaluates to

$$f(V_i, V_j^\mathrm{V}) = \exp\left(-\frac{-V_{i,\min} - D_i \left(1 - \mathrm{e}^{-a_i q_\mathrm{IP}}\right)^2}{k_\mathrm{B}T}\right) = \exp\left(-\frac{-V_{i,\min} + V_\mathrm{IP}}{k_\mathrm{B}T}\right). \tag{4.52}$$

Unfortunately, Equation (4.51) is in general not analytically solvable. Therefore, intersection points can only be found by using numerical methods like for example Newton's method. A more detailed discussion about number and location of intersection points can be found in Section 4.4.6.

### 4.4.5 Transitions for a Continuous Band of States

Up to now it was assumed that there is only an interaction between the charges at the band edges and the trap levels. However, every charge inside the conduction or valence band with an arbitrary energy can interact with the defect level. The electron and hole densities are given by Equations (4.53) and (4.54) (compare also Equation (4.12)).

$$n = \int_{E_\mathrm{C}}^{\infty} g_\mathrm{n}(E) f_\mathrm{n}(E) \mathrm{d}E \tag{4.53}$$

$$p = \int_{-\infty}^{E_\mathrm{V}} g_\mathrm{p}(E) f_\mathrm{p}(E) \mathrm{d}E \tag{4.54}$$

The density of states in the conduction band $g_\mathrm{n}(E)$ is given by Equation (4.14) and the density of states in the valence band can be obtained analogously by exchanging the effective electron mass with the effective hole mass. The carrier distribution function for electrons is the Fermi-Dirac distribution (Equation (4.13)) and the carrier distribution function for holes is given in Equation (4.55).

$$f_\mathrm{p}(E) = \frac{1}{1 + \exp\left(-\frac{E - E_\mathrm{F}}{k_\mathrm{B}T}\right)} \tag{4.55}$$

The carrier distributions of electrons and holes are related via Equations (4.56) and (4.57)

$$f_\mathrm{n}(E) = f_\mathrm{p}(E) \exp\left(-\frac{E - E_\mathrm{F}}{k_\mathrm{B}T}\right) \tag{4.56}$$

$$f_\mathrm{p}(E) = f_\mathrm{n}(E) \exp\left(\frac{E - E_\mathrm{F}}{k_\mathrm{B}T}\right) \tag{4.57}$$

For each charge carrier inside the bands, transition rates as given in Section 4.4.4, can be found. The sum over all these rates yields the total transition rate between the defect state $i$ and all possible states in the valence band $j^\mathrm{V}$ and in the conduction band $j^\mathrm{C}$ [103].

$$k_{ij}^\mathrm{C} = \int_{E_\mathrm{C}}^{\infty} g_\mathrm{n}(E) f_\mathrm{p}(E) A_0 \lambda\left(E, x_\mathrm{t}\right) \exp\left(-\frac{-V_{i,\mathrm{min}} + V_\mathrm{IP}(E)}{k_\mathrm{B}T}\right) \mathrm{d}E \tag{4.58}$$

$$k_{ji}^\mathrm{C} = \int_{E_\mathrm{C}}^{\infty} g_\mathrm{n}(E) f_\mathrm{n}(E) A_0 \lambda\left(E, x_\mathrm{t}\right) \exp\left(-\frac{-\left(V_{j,\mathrm{min}}^\mathrm{C} + E - E_\mathrm{C}\right) + V_\mathrm{IP}(E)}{k_\mathrm{B}T}\right) \mathrm{d}E \tag{4.59}$$

$$k_{ij}^\mathrm{V} = \int_{-\infty}^{E_\mathrm{V}} g_\mathrm{p}(E) f_\mathrm{p}(E) A_0 \lambda\left(E, x_\mathrm{t}\right) \exp\left(-\frac{-V_{i,\mathrm{min}} + V_\mathrm{IP}(E)}{k_\mathrm{B}T}\right) \mathrm{d}E \tag{4.60}$$

$$k_{ji}^\mathrm{V} = \int_{-\infty}^{E_\mathrm{V}} g_\mathrm{p}(E) f_\mathrm{n}(E) A_0 \lambda\left(E, x_\mathrm{t}\right) \exp\left(-\frac{-\left(V_{j,\mathrm{min}}^\mathrm{V} + E_\mathrm{V} - E\right) + V_\mathrm{IP}(E)}{k_\mathrm{B}T}\right) \mathrm{d}E \tag{4.61}$$

In the next step one inserts Equation (4.57) into Equation (4.58) and Equation (4.56) into Equation (4.61).

As the carriers in the semiconductor are strongly localized at the respective band edges one can approximate the WKB-factor and the energy barrier in the exponent by replacing the energy dependence by the band edge energies at the interface ${E_C}^s$ and ${E_V}^s$. Then the integrals evaluate simply to electron and hole densities. The matrix elements are rewritten using $A_0\lambda\left({E_C}^s, x_t\right) = v_{th,n}\sigma_{0,n}\theta_n$ and $A_0\lambda\left({E_V}^s, x_t\right) = v_{th,p}\sigma_{0,p}\theta_p$. Here $v_{th}$ stands for the thermal velocities (see Equation 4.27) of the charge carriers and $\sigma_0\theta$ is the effective capture cross section with the tunneling coefficient $\theta$ [105].

The energies in the exponent of the lineshape function are denoted as energy barriers, e.g. $\mathcal{E}^C_{i,j} = -V_{i,\min} + V_{IP}(E_C)$. The barrier heights $\mathcal{E}_{i,j}$ and $\mathcal{E}_{j,i}$ are related by

$$\mathcal{E}^C_{i,j} = \mathcal{E}^C_{j,i} + {E_C}^s - E_t \tag{4.62}$$

$$\mathcal{E}^V_{i,j} = \mathcal{E}^V_{j,i} + {E_V}^s - E_t \tag{4.63}$$

Thus the rates become

$$k^C_{ij} = n v_{th,n}\sigma_{0,n}\theta_n \exp\left(-\frac{\mathcal{E}^C_{j,i} + E_F - E_t}{k_B T}\right) \tag{4.64}$$

$$k^C_{ji} = n v_{th,n}\sigma_{0,n}\theta_n \exp\left(-\frac{\mathcal{E}^C_{j,i}}{k_B T}\right) \tag{4.65}$$

$$k^V_{ij} = p v_{th,p}\sigma_{0,p}\theta_p \exp\left(-\frac{\mathcal{E}^V_{i,j}}{k_B T}\right) \tag{4.66}$$

$$k^V_{ji} = p v_{th,p}\sigma_{0,p}\theta_p \exp\left(-\frac{\mathcal{E}^V_{i,j} + E_t - E_F}{k_B T}\right). \tag{4.67}$$

### 4.4.6 Electron-Phonon Coupling Regimes

One distinguishes three different electron-phonon coupling (EPC) regimes. The actual regime depends on the energy difference between the initial state $i$ and the final state $j^V/j^C$ , on the dissociation energies of these two states, and on the distance $\Delta q_{ij}$ between the minima of the two states.

The energy difference $\Delta E_{j,i}$ is defined as $\Delta E_{j,i}(F) = V_{j,\min} - V_{i,\min}$. The energy difference $\Delta E_{j,i}$ as well as the dissociation energies $D_i(F)$ and $D_j(F)$ depend strongly on the electric field in the oxide. Therefore, the regime which dominates the charge transfer process can be changed easily by applying another electric field.

As the equation defining number and location of intersection points cannot be analytically solved in the case of Morse potentials, a precise definition of the different regimes is difficult. In the limiting case of the distance between the minima approaching infinity $\Delta q_{ij} \to \infty$, the criteria given below hold. (see Equations (4.68) to (4.70)) For rather small distances $\Delta q_{ij}$ and intermediate energy differences $\Delta E_{j,i}$, it is possible that criterion (4.68) is fulfilled but there is still only one intersection point with either $q_{IP} < q_i < q_j$ or $q_i < q_j < q_{IP}$.

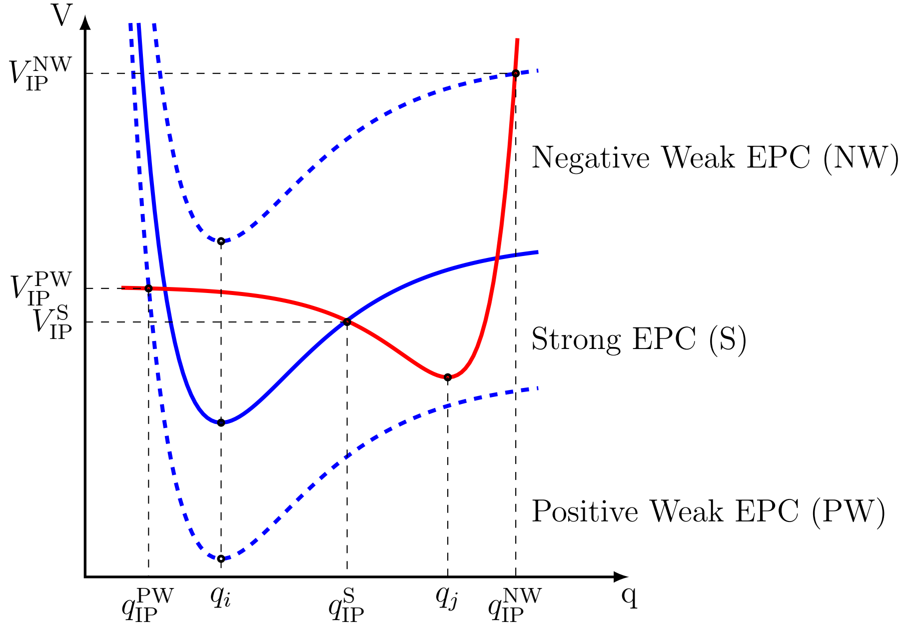


Figure 4.6: Schematic configuration coordinate diagram showing three examples for strong (S), positive weak (PW) and negative weak (NW) electron-phonon coupling.

### Strong electron-phonon coupling

It is defined by

$$|\Delta E_{j,i}(F)| < \min\left(D_i(F), D_j(F)\right). \tag{4.68}$$

In this case there are three intersection points between the two potentials. However the transition rates depend exponentially on the barrier height, so the lowest barrier domiates. The lowest barrier is the one with $q_i < q_{\text{IP}} < q_j$. In the special case of $D_i(F) = D_j(F)$, the intersection point lies exactly in the middle of the two minima $q_{\text{IP}} = (q_j + q_i)/2$.

### Positive weak electron-phonon coupling

It is defined by

$$\Delta E_{j,i}(F) > D_i(F) > 0. \tag{4.69}$$

In this case there is only one intersection point and for this point it holds that $q_{\text{IP}} < q_i < q_j$. The barrier height $\mathcal{E}_{i,j}$ for the transition between state $i$ and state $j$ lies between $\Delta E_{j,i}(F) < \mathcal{E}_{i,j} < \Delta E_{j,i}(F) + D_j(F)$. For the barrier height $\mathcal{E}_{j,i}$ from state $j$ to state $i$ it holds that $0 < \mathcal{E}_{j,i} < D_j(F)$.

### Negative weak electron-phonon coupling

It is defined by

$$\Delta E_{j,i}(F) < -D_j(F) < 0. \tag{4.70}$$

In this case there is only one intersection point and for this point it holds that $q_i < q_j < q_{\mathrm{IP}}$. The barrier height $\mathcal{E}_{i,j}$ for the transition between state $j$ and state $i$ lies between $\Delta E_{j,i}(F) < \mathcal{E}_{j,i} < \Delta E_{j,i}(F) + D_i(F)$. For the barrier height $\mathcal{E}_{j,i}$ from state $i$ to state $j$ it holds that $0 < \mathcal{E}_{i,j} < D_i(F)$.

Summing all up, there is only one main intersection point, which defines the barrier height for the transition. To reduce the computing effort, in the cases of weak EPC the barrier height was not expicitly calculated but approximated by the lower limiting case. Thus, it was set to either $\Delta E_{j,i}(F)$ or to 0 depending on the respective case. The three different cases are illustrated in Figure 4.6.

### 4.4.7 Thermal Barriers

In Section 3.1 it has been emphasized that some effects like anomalous RTN can only be explained in a four-state defect model. Between these four states, four different transitions are possible and only two are charge exchange processes which are described by NMP transition rates, given in Equations (4.64) - (4.67). The other two transitions are structural relaxations which are purely thermally activated. The transitions across these thermal barriers can be described using the transition state theory (TST). When approximating the potential energy surface around the saddle point of the transition and around the initial state by a harmonic oscillator the resulting rates obey an Arrhenius law.

$$k_{ij} = \nu_0 \exp\left(-\frac{\mathcal{E}_{ij}}{k_\mathrm{B}T}\right) \tag{4.71}$$

$$k_{ji} = \nu_0 \exp\left(-\frac{\mathcal{E}_{ji}}{k_\mathrm{B}T}\right) \tag{4.72}$$

The pre-factor is called attempt frequency $\nu_0$. A schematic configuration coordinate diagram showing the thermal barrier between state i and state j is shown in Figure 4.7.

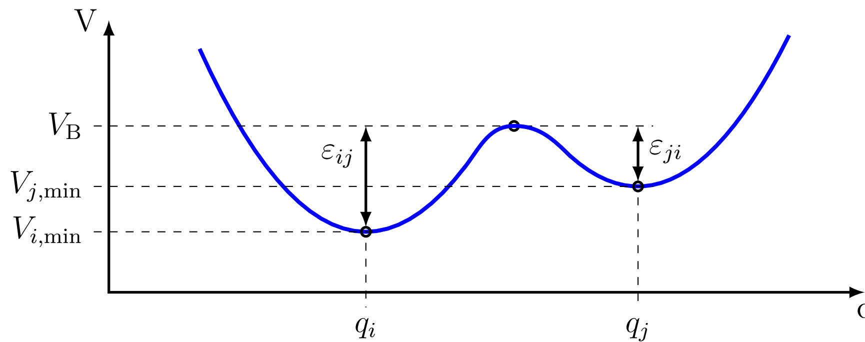


Figure 4.7: Schematic configuration coordinate diagram showing a thermal barrier. [103]

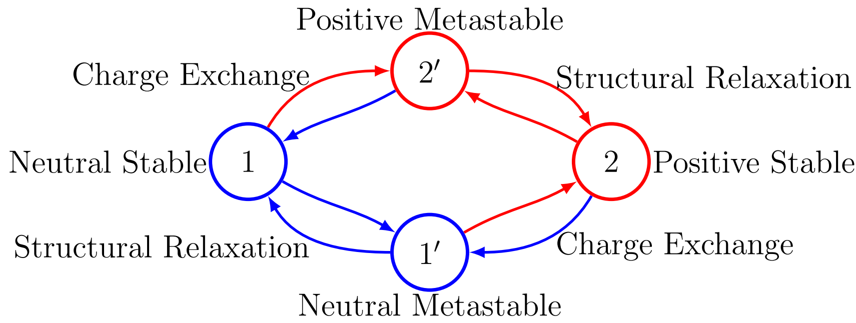


Figure 4.8: State diagram of the four-state NMP model. [103]

### 4.4.8 Four-State NMP Model

The Four-State NMP Model consists of four states 1, 1', 2 and 2', which are related by two NMP transitions and two thermal transitions. In states 1 and 1' the electron is at the defect site and the defect is neutral. In states 2 and 2' the electron is in the valence or the conduction band and the trap is positively charged. The prime always denotes a metastable state. The charge exchange reactions between states 1 and 2 are modeled by NMP transitions and the structural relaxations are modeled by thermal transitions. For NMP transitions the minima are approximated using Morse potentials, and, for structural relaxations the minima are approximated with parabolas. All four states and the relations between these states are shown in Figure 4.8.

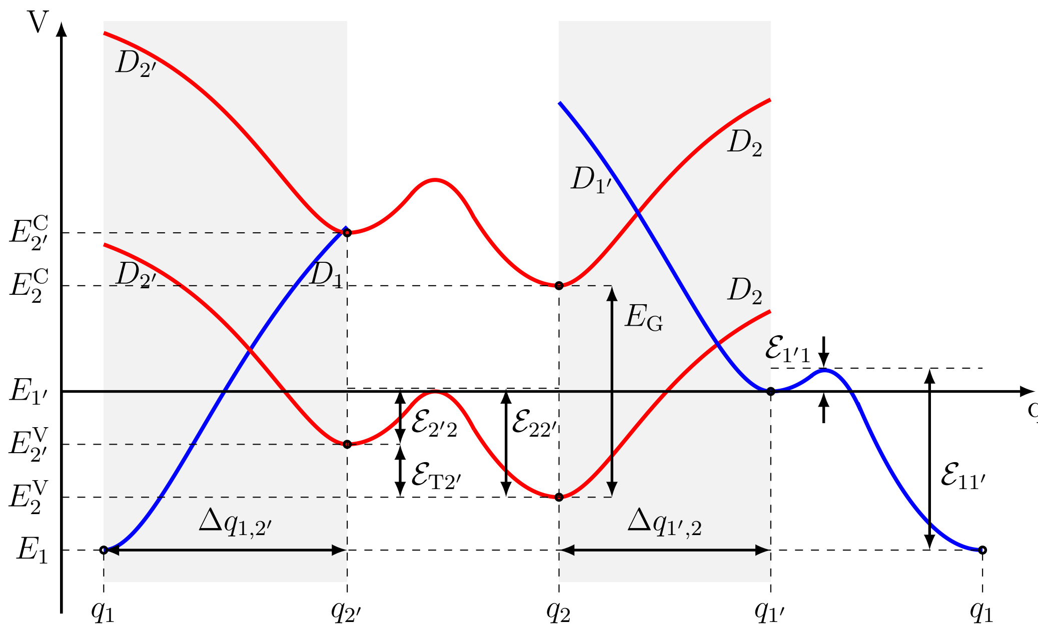


Figure 4.9: Configuration coordinate diagram of a four state NMP process. The NMP transitions modeled using Morse potentials are emphasized with a grey background color.

| Model Parameter | Symbol | Unit/Standard Value |
|---|---|---|
| Trap Density | $N_{\mathrm{ot}}$ | [cm$^{-3}$] |
| Defect Level Mean | $\overline{E_1}$ | [eV] |
| Defect Level Sigma | $\sigma_{\mathrm{E_1}}$ | [eV] |
| Metastable Defect Level Mean | $\overline{E_{1'}}$ | [eV] |
| Metastable Defect Level Sigma | $\sigma_{\mathrm{E_{1'}}}$ | [eV] |
| Dissociation parameter ($1 \rightarrow 2'$) Mean | $\overline{R_{12'}} = D_{2'}/D_1$ | [1] |
| Dissociation parameter ($1 \rightarrow 2'$) Sigma | $\sigma_{\mathrm{R_{12'}}}$ | [1] |
| Dissociation parameter ($1' \rightarrow 2$) Mean | $\overline{R_{1'2}} = D_2/D_{1'}$ | [1] |
| Dissociation parameter ($1' \rightarrow 2$) Sigma | $\sigma_{\mathrm{R_{1'2}}}$ | [1] |
| Distance parameter ($1 \rightarrow 2'$) Mean | $\overline{\Delta q_{12'}} = \lvert q_{2'} - q_1 \rvert$ | [a.u.] |
| Distance parameter ($1 \rightarrow 2'$) Sigma | $\sigma_{\Delta \mathrm{q_{12'}}}$ | [a.u.] |
| Distance parameter ($1' \rightarrow 2$) Mean | $\overline{\Delta q_{1'2}} = \lvert q_2 - q_{1'} \rvert$ | [a.u.] |
| Distance parameter ($1' \rightarrow 2$) Sigma | $\sigma_{\Delta \mathrm{q_{1'2}}}$ | [a.u.] |
| Metastable State 2 Energy Level Mean | $\overline{\mathcal{E}_{\mathrm{T2'}}}$ | [eV] |
| Metastable State 2 Energy Level Sigma | $\sigma_{\mathcal{E}_{\mathrm{T2'}}}$ | [eV] |
| Thermal Barrier 1 Mean | $\overline{\mathcal{E}_{11'}}$ | [eV] |
| Thermal Barrier 1 Sigma | $\sigma_{\mathcal{E}_{11'}}$ | [eV] |
| Thermal Barrier 2 Mean | $\overline{\mathcal{E}_{22'}}$ | [eV] |
| Thermal Barrier 2 Sigma | $\sigma_{\mathcal{E}_{22'}}$ | [eV] |
| Electron/Hole Capture Cross Section | $\sigma_{0,\mathrm{n,p}}$ | $4.5 \times 10^{-20}\,\mathrm{cm}^2$ |
| Electron/Hole Capture Cross Section Metal | $\sigma_{0,\mathrm{n,p,met}}$ | $3 \times 10^{-21}\,\mathrm{cm}^2$ |
| Attempt Frequency | $\nu_0$ | $1 \times 10^{13}\,\mathrm{Hz}$ |
| Force Constant | $k$ | $1.6\,\mathrm{kg/s}^2$ |
| Basic Dissociation Energy | $D_0$ | $5.5\,\mathrm{eV}$ |
| Field Dependence | $\mathrm{d}F$ | $50\,\mathrm{MV/cm}$ |

Table 4.2: Model parameters for the modeling of oxide traps using the four-state NMP model.

The configuration coordinate diagram of the four-state NMP model is shown in Figure 4.9. The energy minima $E_1$, $E_2^{\mathrm{C}}$ and $E_2^{\mathrm{V}}$ correspond to the energy minima in Section 4.4.3 (Equations (4.40) to (4.42)). Therefore, $E_1$ has to be specified via the trap level and $E_2^{\mathrm{C}}$ and $E_2^{\mathrm{V}}$ are given by the band edges of conduction and valence band at the interfaces. The distance between the metastable minima and the stable state 2 is given by $\mathcal{E}_{\mathrm{T2'}}$.

$$\mathcal{E}_{\mathrm{T2'}} = V_{2'}^{\mathrm{V}} - V_2^{\mathrm{V}} = V_{2'}^{\mathrm{C}} - V_2^{\mathrm{C}} \tag{4.73}$$

The quantity $\mathcal{E}_{\mathrm{T2}}$ always has to be greater than zero and also $V_{1'}$ has to be larger than $V_1$, otherwise these states would not be metastable.

To fully specify the four-state NMP model, the parameters given in Table 4.2 have to be defined in Minimos-NT. The relative locations of the trap levels and the curvatures of different potentials can vary depending on the local surroundings of the respective

traps. Therefore, these quantities are assumed to show a Gaussian distribution. This distribution is specified by the mean and the standard deviation. In Table 4.2 the parameters necessary to define location and shape of all curves in Figure 4.9 on all trap sites are given. Additionally the standard values for the constants which are used for calculating the transition rates are listed. Here an additional quantity, the capture cross section for electrons or holes interacting with the oxide from an adjacent metal layer (e.g. metal gate) is specified $\sigma_{0,\mathrm{n,p,met}}$. Using these quantities the transition rates between the four states follow directly from Equations (4.64) to (4.67) and Equations (4.71) to (4.72).

$$\begin{aligned}
k_{12'} &= k^{\mathrm{C}}_{12'} + k^{\mathrm{V}}_{12'} \\
&= n v_{\mathrm{th,n}} \sigma_{0,\mathrm{n}} \theta_{\mathrm{n}} \exp\left(-\frac{\mathcal{E}^{\mathrm{C}}_{2',1} + E_{\mathrm{F}} - E_1}{k_{\mathrm{B}}T}\right) + p v_{\mathrm{th,p}} \sigma_{0,\mathrm{p}} \theta_{\mathrm{p}} \exp\left(-\frac{\mathcal{E}^{\mathrm{V}}_{1,2'}}{k_{\mathrm{B}}T}\right) && (4.74)\\
k_{2'1} &= k^{\mathrm{C}}_{2'1} + k^{\mathrm{V}}_{2'1} \\
&= n v_{\mathrm{th,n}} \sigma_{0,\mathrm{n}} \theta_{\mathrm{n}} \exp\left(-\frac{\mathcal{E}^{\mathrm{C}}_{2',1}}{k_{\mathrm{B}}T}\right) + p v_{\mathrm{th,p}} \sigma_{0,\mathrm{p}} \theta_{\mathrm{p}} \exp\left(-\frac{\mathcal{E}^{\mathrm{V}}_{1,2'} + E_1 - E_{\mathrm{F}}}{k_{\mathrm{B}}T}\right) && (4.75)\\
k_{2'2} &= \nu_0 \exp\left(-\frac{\mathcal{E}_{22'} - \mathcal{E}_{\mathrm{T}2'}}{k_{\mathrm{B}}T}\right) && (4.76)\\
k_{22'} &= \nu_0 \exp\left(-\frac{\mathcal{E}_{22'}}{k_{\mathrm{B}}T}\right) && (4.77)\\
k_{21'} &= k^{\mathrm{C}}_{21'} + k^{\mathrm{V}}_{21'} \\
&= n v_{\mathrm{th,n}} \sigma_{0,\mathrm{n}} \theta_{\mathrm{n}} \exp\left(-\frac{\mathcal{E}^{\mathrm{C}}_{2,1'}}{k_{\mathrm{B}}T}\right) + p v_{\mathrm{th,p}} \sigma_{0,\mathrm{p}} \theta_{\mathrm{p}} \exp\left(-\frac{\mathcal{E}^{\mathrm{V}}_{1',2} + E_{1'} - E_{\mathrm{F}}}{k_{\mathrm{B}}T}\right) && (4.78)\\
k_{1'2} &= k^{\mathrm{C}}_{1'2} + k^{\mathrm{V}}_{1'2} \\
&= n v_{\mathrm{th,n}} \sigma_{0,\mathrm{n}} \theta_{\mathrm{n}} \exp\left(-\frac{\mathcal{E}^{\mathrm{C}}_{2,1'} + E_{\mathrm{F}} - E_{1'}}{k_{\mathrm{B}}T}\right) + p v_{\mathrm{th,p}} \sigma_{0,\mathrm{p}} \theta_{\mathrm{p}} \exp\left(-\frac{\mathcal{E}^{\mathrm{V}}_{1',2}}{k_{\mathrm{B}}T}\right) && (4.79)\\
k_{1'1} &= \nu_0 \exp\left(-\frac{\mathcal{E}_{11'} - E_{1'}}{k_{\mathrm{B}}T}\right) && (4.80)\\
k_{11'} &= \nu_0 \exp\left(-\frac{\mathcal{E}_{11'}}{k_{\mathrm{B}}T}\right) && (4.81)
\end{aligned}$$

From the transistion rates the capture and emission times of the defects can be calculated. These quantities can be extracted via measurements (see Chapter 3) and therefore provide one possibility to verify the model parameters in use.

Assuming that at a given time $t_0$ the system is in state $i$, a transition to state $j$ will occur after the first passage time $\tau_{i,j}$ [105]. As the first passage time is a stochastic quantity one has to look at its expectation value. The capture time for a hole is the expectation value for the transition from state 1 to state 2. If the considered system is a simple two state system this expectation value is simply given by the inverse of the respective transition rate. In a four-state system a transition from state 1 to state 2 can only be achieved over the metastable states, either via state $1'$ or state $2'$. In analogy

the emission time for a hole is the expectation value for the transition from state 2 to state 1.

$$\tau_c = \overline{\tau_{12}} \tag{4.82}$$

$$\tau_e = \overline{\tau_{21}} \tag{4.83}$$

The capture process in a four-state system can in principle take place equally probable over state $1'$ and state $2'$, in reality the actual rates for the different paths lead to different probabilities. Both transition paths can be assumed as isolated three state chains. The separation into independent paths is possible because the four-state process is assumed to be a Markov process. This means that the next transition is independent from the previous one, the system does not "remember" the reaction path via which it came into the present state. The assumption is justified as long as the system relaxes after each transition by interactions with its environment [125].

The time constants for the isolated three state chains are obtained as [105]

$$\tau_c^{1'} = \frac{k_{11'} + k_{1'1} + k_{1'2}}{k_{11'}k_{1'2}}, \tag{4.84}$$

$$\tau_c^{2'} = \frac{k_{12'} + k_{2'1} + k_{2'2}}{k_{12'}k_{2'2}}, \tag{4.85}$$

$$\tau_e^{1'} = \frac{k_{1'1} + k_{1'2} + k_{21'}}{k_{1'1}k_{21'}}, \tag{4.86}$$

$$\tau_e^{2'} = \frac{k_{2'1} + k_{2'2} + k_{22'}}{k_{2'1}k_{22'}}. \tag{4.87}$$

The total capture and emission time constants follow [105]

$$\tau_c = \frac{1}{\dfrac{1}{\tau_c^{1'}} + \dfrac{1}{\tau_c^{2'}}}, \tag{4.88}$$

$$\tau_e = \frac{1}{\dfrac{1}{\tau_e^{1'}} + \dfrac{1}{\tau_e^{2'}}}. \tag{4.89}$$

The charge exchange processes between the oxide and the channel leads to a change in the total amount of charges in the oxide, and consequently to a change in the threshold voltage. So what one actually observes are changes in the occupation probabilities of the charged and uncharged states. The time constants (Equations (4.88) and (4.89)) describe the time scales on which these changes take place. In the framework of first order Markov chain theory the probability that a transition from state $i$ to state $j$ takes place during the incremental time step $h$, assuming that the system is in state $i$ at the time t $P\{X_i(t) = 1\} = 1$, is given by

$$P\{X_j(t+h) = 1 | X_i(t) = 1\} = k_{ij}h + O(h). \tag{4.90}$$

The probability to remain in state $i$ is given by

$$P\left\{X_i(t+h)=1|X_i(t)=1\right\}=1-\sum_{i\neq j}k_{ij}h+O(h). \tag{4.91}$$

In this expression the sum runs over all reaction paths leading away from state $i$. In the limit $h\rightarrow 0$ the general Master equation is obtained as [105]

$$\frac{\partial p_i(t)}{\partial t}=-p_i(t)\sum_{j\neq i}k_{i,j}+\sum_{j\neq i}k_{i,j}p_j(t). \tag{4.92}$$

This is a first order coupled differential equation system with N equations, where N is the number of states. In the case of the four states of the NMP model the Master equation becomes

$$\frac{\partial p_1(t)}{\partial t}=k_{1'1}p_{1'}(t)+k_{2'1}p_{2'}(t)-k_{11'}p_1(t)-k_{12'}p_1(t) \tag{4.93}$$

$$\frac{\partial p_{1'}(t)}{\partial t}=k_{11'}p_1(t)+k_{21'}p_2(t)-k_{1'1}p_{1'}(t)-k_{1'2}p_{1'}(t) \tag{4.94}$$

$$\frac{\partial p_2(t)}{\partial t}=k_{1'2}p_{1'}(t)+k_{2'2}p_{2'}(t)-k_{22'}p_2(t)-k_{21'}p_2(t) \tag{4.95}$$

$$\frac{\partial p_{2'}(t)}{\partial t}=k_{12'}p_1(t)+k_{22'}p_2(t)-k_{2'2}p_{2'}(t)-k_{2'1}p_{2'}(t). \tag{4.96}$$

Additionally, the sum over all occupation probabilities has to be unity at any time, as the system always has to be in one of the possible states, resulting in the additional Equation (4.97).

$$p_1(t)+p_{1'}(t)+p_2(t)+p_{2'}(t)=1 \tag{4.97}$$

Solving these equations gives the occupation probabilities of all states as a function of time. Therefore, the evolution of the charge state of one fixed charge as a function of time is given as

$$q_{\mathrm{NMP}}(t)=q_0(p_2(t)+p_{2'}(t)). \tag{4.98}$$

When performing the calculations self consistently this additional charge is added into the Poisson equation at each iteration in every time step of the simulation. Thereby, the charges change the transition rates in the next time step. This process is computationally very demanding. To save computation time one can inhibit the simulator from adding the charges, which are still calculated in every time step, to the Poisson equation. In this case the shift of the threshold voltage due to the change of fixed charges in the oxide have to be calculated in a post processing step. This calculation is done using the Charge Sheet Approximation (CSA) described in the next section.

### 4.4.9 Charge Sheet Approximation

This approximation is based on the assumption that a trap with charge $q_{\mathrm{NMP}}(t)$ at distance $x_{\mathrm{t}}$ from the interface corresponds to a homogenous charge sheet with the charge sheet density $\sigma_{\mathrm{t}}$.

$$\sigma_{\mathrm{t}}(t) = \frac{q_{\mathrm{NMP}}(t)}{WL} \tag{4.99}$$

By inserting this charge sheet density in Equation (3.2), which follows directly from the Poisson equation, one obtains the following threshold voltage shift at time $t$ due to the additional charge

$$\Delta V_{\mathrm{th}}(t) = -\frac{q_{\mathrm{NMP}}(t)}{\epsilon_0 \epsilon_r WL} \left(d_{\mathrm{ox}} - x_{\mathrm{t}}\right). \tag{4.100}$$

In reality the impact of a trapped charge on the threshold voltage might vary from the estimation by Equation (4.100), depending on the distribution of traps and an eventually inhomogeneous current density in the channel [135]. This is accounted for by introducing a factor $\eta_r$ [136]. Usually for large ensembles of traps, the actual distribution has a minor impact, leading to a value of $\eta_r$ close to unity. To calculate the total change $\Delta V_{\mathrm{th}}(t)_{\mathrm{tot}}$ in the threshold voltage due to all trapped charges in the oxide, the sum over all traps $N = N_{\mathrm{ot}} V$ has to be evaluated.

$$\Delta V_{\mathrm{th}}(t)_{\mathrm{tot}} = -\sum_{n}^{N} \left( \frac{q_{\mathrm{NMP,n}}(t)}{\epsilon_0 \epsilon_r WL} \left(d_{\mathrm{ox}} - x_{\mathrm{t}}\right) \eta_{r,n} \right) \tag{4.101}$$

# CHAPTER 5 Results

In this chapter the measured and simulated characteristics of the devices A-D described in Section 2.6 are presented. At first, the exact chronological order of the measurements is given. This order is very important, as the devices' properties react extremely sensitively to thermal stress and during some of the measurements the devices were heated up externally. Then the parameters used for simulating $I_D(V_G)$ characteristics are given and the influence of some of the most important parameters on the characteristic is discussed. The impact of oxide defects and interface traps is analyzed with measurements and simulations of hysteresis and BTI. This reveals important details about the defects governing the degradation of $MoS_2$ transistors.

## 5.1 Measurements

In general, degradation effects on the $MoS_2$ devices studied in this work are large. While on the one hand, this work targets at analyzing exactly these degradation mechanisms, on the other hand there is an unavoidable degradation of the devices during the course of the measurements. This degradation leads to a change in the device parameters from one measurement to another. Therefore, it does not make sense to consider, for example, one PBTI measurement as a single event, but one rather has to treat this experiment as one of many experiments in a row. The results of this experiment might be influenced by preceding measurements.

What is more, as shown in Figure 2.11(b), all devices were fabricated close to each other on top of one $MoS_2$ flake. Therefore, any external annealing steps always have an influence on all devices and any voltage stress which is applied to one device is at the same time applied to all other devices via the common back gate.

Every external heating step will prove to have a big impact on all devices. When applying a voltage at the back gate of the devices, always only the channel of one device carries a current, as only one contact is set to a fixed drain voltage, while the source contacts and all other drain contacts are grounded. Therefore, stress induced charge capture mechanisms in the other devices and resulting permanent degradation effects influencing subsequent measurements can probably be neglected.

The exact measurement history is given in Figure 5.1.

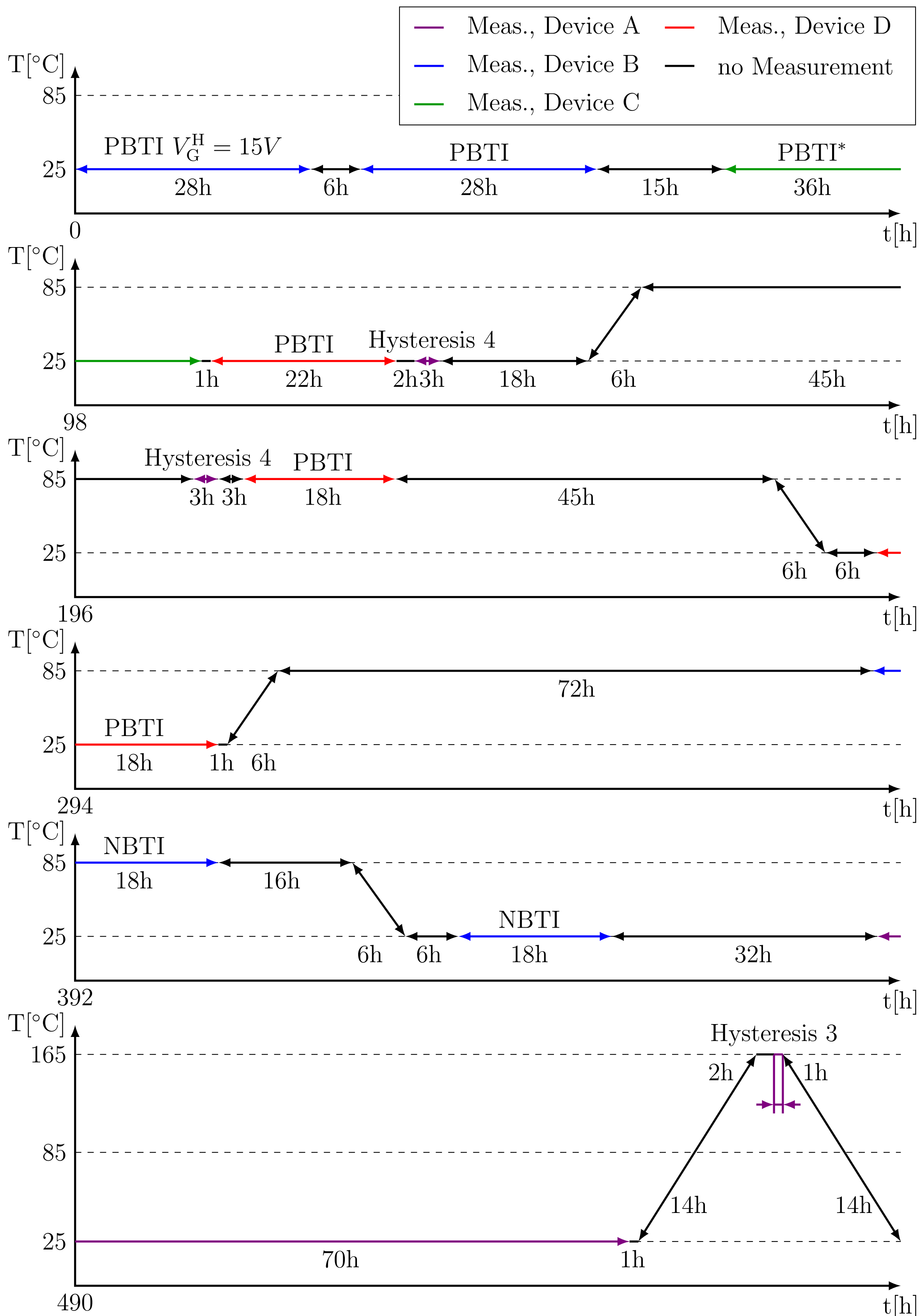


Figure 5.1: Measurement history of devices A-D. "Hysteresis 4" states that four hysteresis sweeps were performed. If there are no further remarks, NBTI/PBTI refers to a typical BTI measurement cycle.

In a hysteresis measurement the drain current is measured as a function of the gate voltage, starting at -20V, going up to +20V and returning back to -20V again. Such a cycle is repeated three or four times for every measurement. For different measurements the sweep rate $S$ is varied, the variation intervals used for measurements at different temperatures are summarized in Table 5.1. Further details of the hysteresis measurement process can be found in Section 3.2.1.

| $T$[°C] | $S$[V/s] | $t_{\mathrm{m}}$[s] |
|---|---|---|
| 25 | 0.2-5 | 800-32 |
| 85 | 0.2-100 | 800-1.6 |
| 165 | 4000 | 0.03 |

Table 5.1: Sweep rates used for hysteresis measurements at different temperatures.

A typical BTI measurement cycle consists of four stressing periods, where the device is subjected to the high voltage $V_{\mathrm{G}}^{\mathrm{H}} = \pm 20\,\mathrm{V}$ for 0.5 ks, then for 1.0 ks, for 5.0 ks and finally for 10.0 ks. After each stress period the threshold voltage shift is measured during the recovery period which lasts 10.0 ks. During recovery the gate contact was left at a floating potential. If a different stress voltage level $V_{\mathrm{G}}^{\mathrm{H}}$ was used or a different total recovery time, these values are listed separately in Figure 5.1. In the PBTI measurement marked with "$*$" in Figure 5.1 four subsequent 10.0 ks stress periods were performed using an increasing stress voltage $V_{\mathrm{G}}^{\mathrm{H}} = \pm 5\,\mathrm{V}/\pm 10\,\mathrm{V}/\pm 15\,\mathrm{V}/\pm 20\,\mathrm{V}$. Further details of the BTI measurement process can be found in Section 3.3.4.

## 5.2 Modeling of Transfer Characteristics

Figure 5.2 compares the measured and simulated transfer characteristics on device A. One can see that they show good agreement. The main difficulty when it comes to obtaining these results is to implement the material properties of an $MoS_2$ monolayer into the framework of the Minimos-NT simulator. S. Thiele [77] remarked that the band structure of $MoS_2$ monolayers is very similar to that of gallium arsenide (GaAs). Both materials are direct semiconductors and show two minima in the conduction band and one dominant minimum in the valence band. In the case of GaAs the side minimum lies at the L point, $\Delta E \approx 0.3\,\mathrm{eV}$ [86] higher than the main minimum and in the case of $MoS_2$ the side minimum lies between K and $\Gamma$ point, $\Delta E \approx 0.2\,\mathrm{eV}$ [59] higher than the main minimum (compare Figure 2.7). Therefore, the in Minimos-NT implemented material parameters for GaAs were used as basis for the following adaptations.

The adapted material parameters are presented in Table 5.2. The number of equivalent conduction band minima $M_{\mathrm{C}}$ is a pre-factor of the effective density of states (see Equation (4.19)). The work function differences at source and drain contact $E_{\mathrm{W}}$ are set to the Schottky barrier height, measured for gold contacts on $MoS_2$ monolayers. The work function difference at the gate contact $E_{\mathrm{WG}}$ is chosen as the difference between silicon

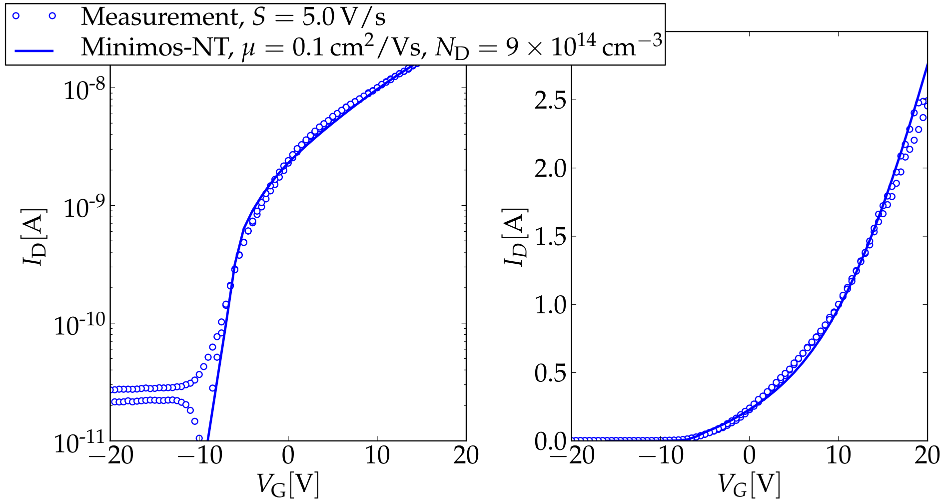


Figure 5.2: Comparison of measured and simulated transfer characteristics of device A at $T = 25\,°\mathrm{C}$. The distance between the measurement points corresponds to the step voltage $V_{\mathrm{step}} = 0.5\,\mathrm{V}$ used for sampling the voltage range in the measurement.

mid gap and the valence band, as without any specification, the Fermi level would be located at silicon mid gap in Minimos-NT.

Table 5.2 contains ten different parameters, which seems to be a lot. However, as it was analyzed by Machta et al. [137] many multi-parameter models like the drift-diffusion model are sensitive to only a small number of parameters and robust to changes in the rest. This observation proves to be true in this context as well. The simulated transfer characteristics change only slightly when altering, for example, the size of the band gap, the effective masses or the relative permittivity. This is why the small differences between used and most accurate reported values in literature, shown in Table 5.2, are of minor importance. Only few settings are essential to obtain an accordance as good as shown in Figure 5.2.

First of all, in order to obtain the right function profile above threshold, it is very important to extend the contact at source and drain across the entire area of the top contact. As described in Section 2.5 the titanium adhesion layer forms covalent bonds to the surface of $MoS_2$ making the top contact the main pathway for the current.

Secondly, the saturation current is governed by three factors. It is determined by the width of the respective device, given in Section 2.6. Furthermore, it is influenced by the mobility, which was calculated as described in Section 2.4. The mobility has to be recalculated for every new device and after every annealing step. Long annealing periods, like the ones shown in Figure 5.1 change the contact resistance and therefore the effective mobility as well. The effective mobility, given in column "Value (ref.)" in Table 5.2, was obtained by taking the maximum of the derivative of all $I_D\,(V_G)$ characteristics measured on device A during the first hysteresis measurement round at 25 °C. Finally the saturation current depends sensitively on the level of external doping. This dependence

| Parameter | Symbol | Var. | Value (used) | Value (ref.) | Source | Section |
|---|---|---|---|---|---|---|
| Band Gap | $E_G$ | no | 2.76 eV | 2.67 eV | [59] | 2.3.2 |
| Electron Affinity | $\chi$ | no | −3.74 eV | −3.84 eV | [13] | 2.3.2 |
| Doping Density | $N_D$ | yes | $9 \times 10^{14}\,\mathrm{cm}^{-3}$ | - | - | - |
| Eff. Mobility | $\mu^{\mathrm{eff}}$ | yes | $0.1\,\mathrm{cm}^2/\mathrm{Vs}$ | $0.08(5)\,\mathrm{cm}^2/\mathrm{Vs}$ | - | 2.4 |
| Conduction Min. | $M_C$ | no | 2 | 2 | [77] | - |
| Eff. Electron Mass | $m_n^*$ | no | 0.57 | 0.55 | [13] | 2.3.2 |
| Eff. Hole Mass | $m_p^*$ | no | 0.66 | 0.56 | [13] | 2.3.2 |
| Rel. Permittivity | $\epsilon_r$ | no | 4.2 | 4.0 | [13] | 2.3.2 |
| Work func. S/D | $E_W$ | no | 0.126 eV | 0.126 eV | [88] | 2.5 |
| Work func. G | $E_{WG}$ | no | 0.56 eV | 0.56 eV | - | - |

Table 5.2: Adapted material parameters of $MoS_2$ monolayers.The third column of this table is titled “Var.”, standing for variation. It states whether this parameter is considered as a material constant and is therefore left unchanged for all simulations or whether this parameter is assumed to change from device to device and due to thermal annealing between different measurement rounds. The fourth column gives the numerical value of the parameter used for simulations, either on all devices or especially for simulating transfer characteristics of device A at 25 °C. The fifth column holds the at present most probable numerical value, which might slightly differ from the value used and the next column gives the literature source, where this value can be found. The last column refers to the section of this work, where the respective parameter is discussed in more detail.

is illustrated in Figure 5.3.

Even though an $MoS_2$ monolayer is known to be intrinsically n-doped, it has been shown that with the choice of the right contact material it is possible to fabricate a pMOS transistor, where holes are the majority charge carriers [80]. Therefore, the doping density $N_D$, which is used in the simulations, gives not the intrinsic doping level, but rather the charge density contributing to the current flow, which is influenced strongly by the contacts as well. The effective doping $N_D$ is obtained as the difference between the donor concentration $N_{\mathrm{don}}$ and the acceptor concentration $N_{\mathrm{acc}}$. The acceptor concentration is always chosen to be equal to the level of effective doping $N_{\mathrm{acc}} = N_D$ and the donor concentration is chosen twice as big $N_{\mathrm{don}} = 2N_D$. The effective doping density $N_D$ is used as a fit parameter to adjust the saturation current level and is therefore varied for different devices and for measurement rounds at different temperatures.

The third factor essential for obtaining a good accordance between measurement and simulation is the amount of fixed charges in the channel region. These charges cause a shift of the threshold voltage. In a stationary simulation, where thermal equilibrium ($t \to \infty$) is established at every voltage step, the effective charge state of the oxide traps is not realistic, especially the traps with long time constants show in reality a different charge state. In this case the amount of fixed charges is modeled by placing a

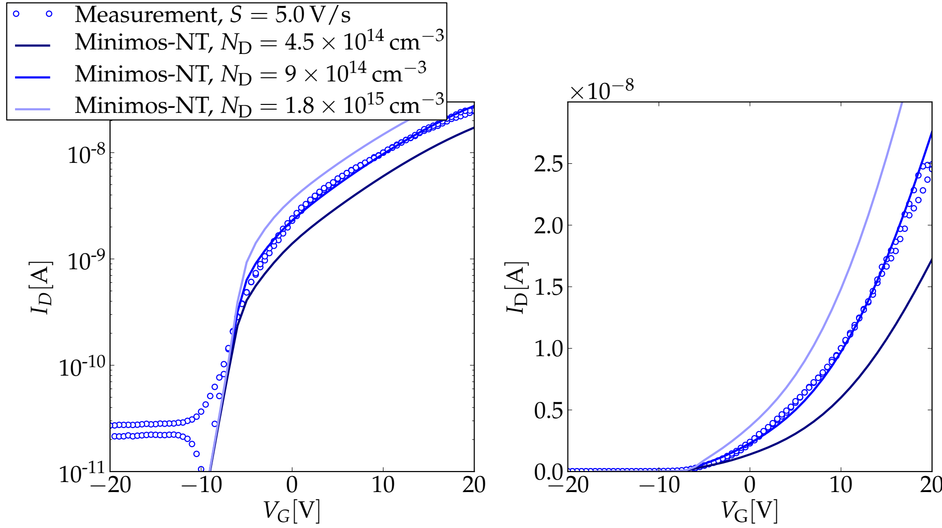


Figure 5.3: Comparison of simulation results for different values of the fit parameter $N_D$ on device A at $T = 25\,°C$.

sheet of fixed charges at the interface between gate dielectric and channel. The sheet density of interface charges $N_{ch}$ is a second fit parameter, adapted for every device after every annealing step, determining the threshold voltage. For example, for device A at 25 °C the interface charge density $N_{ch} = 1.7 \times 10^{12}\,cm^{-2}$ causes a shift of the threshold voltage of about $\Delta V_{th} \approx -8\,V$. The interface charge density is set to zero for transient simulations including oxide traps.

Finally, to model the sub threshold slope correctly, the right amount of interface traps has to be placed close to the conduction band edge. Figure 5.4 illustrates the effect of a changed interface trap density $N_{it}$ on the transfer characteristic and it shows that the interface traps have to be modeled as donor like traps. Acceptor like traps would shift the threshold voltage to more positive values, contrarily to the trend observed.

The interface traps were modeled using the SRH model with trap levels following a normal distribution, as described in Section 4.3. The model parameters chosen to adjust the sub threshold slope are given in Table 5.3. In the third column of this table it is indicated that only the interface trap density was varied for different devices, whereas all other parameters were kept the same. The interface trap density is assumed to stay the same on one device, regardless of any annealing steps.

I set the maximum of the Gaussian distribution of trap levels at $-0.2\,eV$ below the conduction band edge. The distribution is cut off by ${E_t}^{max}$ at exactly the same maximum trap level. This is done in order to assure that no interface traps are permanently charged throughout most part of the $I_D\,(V_G)$ sweep, effectively leading to a shift of a threshold voltage. Thus, the upper cut off of the distribution is situated below the band edge and not at the band edge to enable a clear separation of the adjustment of the sub threshold slope and the threshold voltage. I set the lower cut off exactly at the valence band edge. As the variation of defect levels $\sigma_t$ is small, most of the defects lie between $-0.2\,eV$ and $-0.5\,eV$ below the conduction band edge. Only these interface traps seem to have an

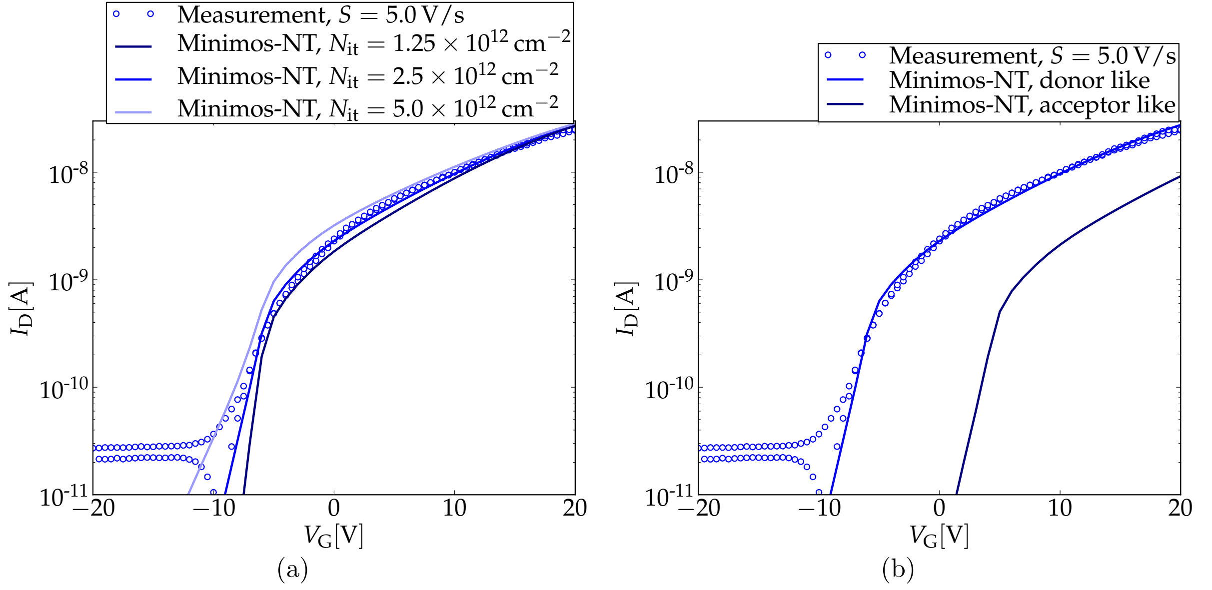


Figure 5.4: Comparison of different interface trap densities $N_{it}$ and donor vs. acceptor like traps on device A at $T = 25\,°C$.

| Model Parameter | Symbol | Var. | Value |
|---|---|---|---|
| Trap Density | $N_{it}$ | yes | $2.5 \times 10^{12}\,cm^{-2}$ |
| Mean Defect Level | $\overline{E_t}$ | no | $-3.94\,eV$ |
| Std. Deviation of Defect Levels | $\sigma_t$ | no | $0.3\,eV$ |
| Maximum Defect Level | $E_t^{max}$ | no | $-3.94\,eV$ |
| Minimum Defect Level | $E_t^{min}$ | no | $-6.5\,eV$ |

Table 5.3: Model parameters used for modeling the interface traps between the $MoS_2$ monolayer and $SiO_2$ using the SRH model.

impact on the sub threshold slope.

Summing all up, even if there are many model parameters to describe the $MoS_2$ monolayer as the channel material of a back gate transistor, most of the parameters hardly influence the transfer characteristic at all. This leads to three main fit parameters in static simulations, namely the doping density $N_D$, the sheet density of fixed interface charges $N_{ch}$ and the sheet density of interface traps $N_{it}$.

Another parameter having only a minor impact on the transfer characteristic, is the effective mass of charge carriers. S. Thiele [77] proposed to correct quantum mechanical confinement by using a multiplicative factor of 3.0 for the effective mass (see Section 4.2). This factor was not used in this work, as it's effect on the transfer characteristic is small, which is demonstrated in Figure 5.5.

In this work I focus on modeling the hysteresis measurements of device A at 25 °C, 85 °C and 165 °C, on the NBTI measurements of device B and on the PBTI measurements

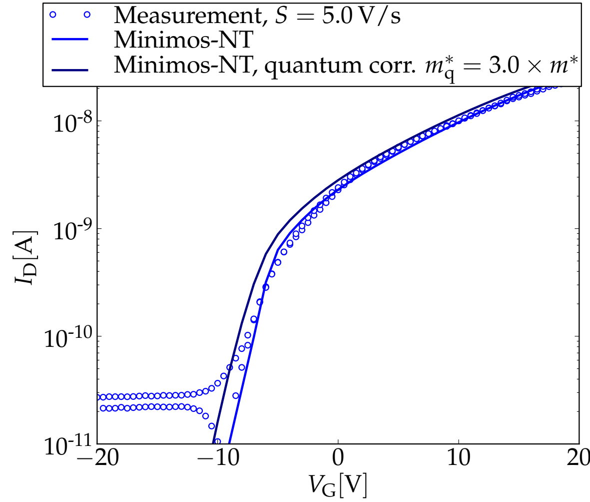


Figure 5.5: Simulation results obtained with and without the correction proposed for quantum confinement by S. Thiele [77]. The characteristics of device A at $T = 25\,°\mathrm{C}$ are shown.

of device D, both at 25 °C and 85 °C (compare Figure 5.1). Due to the variability, the fit parameters have to be adjusted to each device and to every annealing step. The doping density $N_\mathrm{D}$ and the mobility $\mu^\mathrm{eff}$ vary between all devices and temperature steps. The interface trap density and the density of fixed interface charges are considered as device properties and remain unaffected by annealing.

| Device | Temperature | $W$[µm] | $N_\mathrm{D}$[cm$^{-3}$] | $\mu^\mathrm{eff}$[cm$^2$/Vs] | $N_\mathrm{it}$[cm$^{-2}$] | $N_\mathrm{ch}$[cm$^{-2}$] |
|---|---|---|---|---|---|---|
| A | 25 °C | 6.8 | $9 \times 10^{14}$ | 0.1 | $2.5 \times 10^{12}$ | $1.7 \times 10^{12}$ |
| A | 85 °C | 6.8 | $3.5 \times 10^{15}$ | 0.25 | $2.5 \times 10^{12}$ | $1.7 \times 10^{12}$ |
| A | 165 °C | 6.8 | $1.5 \times 10^{19}$ | 1.5 | $2.5 \times 10^{12}$ | $1.7 \times 10^{12}$ |
| B | 25 °C | 8.0 | $3.2 \times 10^{15}$ | 0.32 | $2.5 \times 10^{12}$ | $1.1 \times 10^{12}$ |
| B | 85 °C | 8.0 | $3.2 \times 10^{15}$ | 0.4 | $2.5 \times 10^{12}$ | $1.1 \times 10^{12}$ |
| D | 25 °C | 4.8 | $2.0 \times 10^{16}$ | 0.13 | $7.5 \times 10^{12}$ | $0.7 \times 10^{12}$ |
| D | 85 °C | 4.8 | $2.0 \times 10^{16}$ | 0.2 | $7.5 \times 10^{12}$ | $0.7 \times 10^{12}$ |

Table 5.4: Variation of parameters for different devices at different temperatures.

In Table 5.4 the fit parameters for these devices and temperature steps are given together with the widths of different devices. The doping density increases due to annealing and remains at the higher level for subsequent measurements even at lower temperatures. This can be easily by an activation of existing defects during the thermal treatment. At higher temperatures, the extracted mobility increases significantly. Due to increased lattice scattering, an opposite trend would be expected. This is again an indication that the effective mobility includes first and foremost the amount of current flowing across the Schottky barriers, which increases at higher temperatures due to an

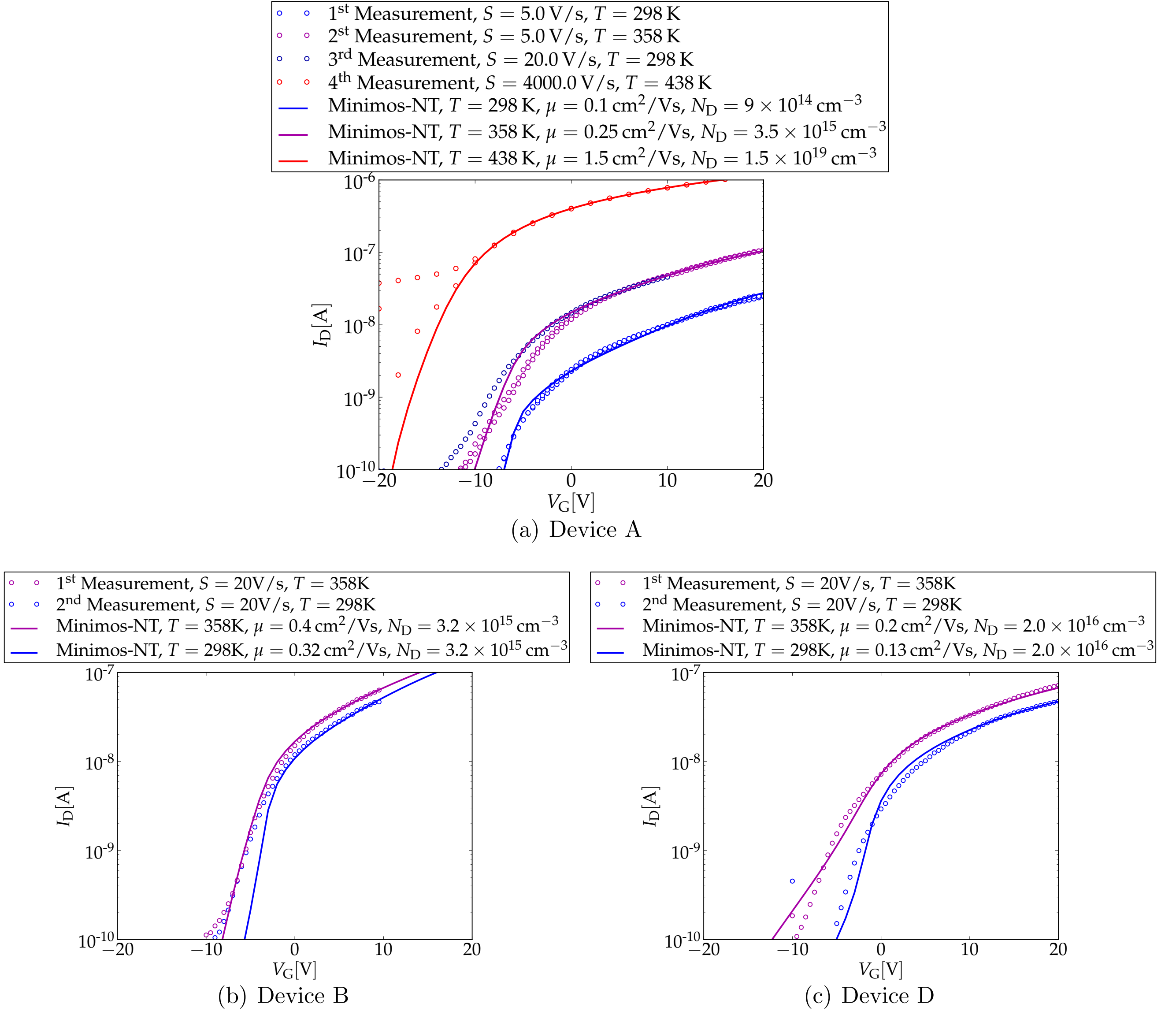

(a) Device A

(b) Device B

(c) Device D

Figure 5.6: Transfer characteristics measured at different times on devices A, B and D.

increased kinetic energy of carriers. The characteristics, which were simulated using the parameters from Table 5.4, are shown in Figure 5.6.

## 5.3 Modeling of Hysteresis Measurements

As demonstrated in Section 3.2, the hysteresis observed in the transfer characteristic can be explained by charge trapping and detrapping events in the oxide. To model the charge exchange with oxide traps, the four-state NMP model (see Section 4.4.8) was used. The model parameters of the four-state NMP model, which obtained the best

accordance between measured and simulated hysteresis characteristics, are presented in Table 5.5. The column “Var.” shows that only the oxide trap density $N_{\mathrm{ot}}$ is assumed to be affected by annealing steps.

| Model Parameter | Symbol | Var. | Value |
|---|---|---|---|
| Trap Density | $N_{\mathrm{ot}}$ | yes | $2 \times 10^{20}\,\mathrm{cm}^{-3}$ |
| Defect Level Mean | $\overline{E_1}$ | no | 0.6 eV |
| Defect Level Sigma | $\sigma_{\mathrm{E}_1}$ | no | 0.32 eV |
| Metastable Defect Level Mean | $\overline{E_{1'}}$ | no | 1.26 eV |
| Metastable Defect Level Sigma | $\sigma_{\mathrm{E}_{1'}}$ | no | 0.15 eV |
| Dissociation parameter ($1 \rightarrow 2'$) Mean | $\overline{R_{12'}} = D_{2'}/D_1$ | no | 0.39 |
| Dissociation parameter ($1 \rightarrow 2'$) Sigma | $\sigma_{\mathrm{R}_{12'}}$ | no | 0.2 |
| Dissociation parameter ($1' \rightarrow 2$) Mean | $\overline{R_{1'2}} = D_2/D_{1'}$ | no | 0.76 |
| Dissociation parameter ($1' \rightarrow 2$) Sigma | $\sigma_{\mathrm{R}_{1'2}}$ | no | 0.23 |
| Distance parameter ($1 \rightarrow 2'$) Mean | $\overline{\Delta q_{12'}} = \lvert q_{2'} - q_1 \rvert$ | no | 2.12 |
| Distance parameter ($1 \rightarrow 2'$) Sigma | $\sigma_{\Delta \mathrm{q}_{12'}}$ | no | 0.8 |
| Distance parameter ($1' \rightarrow 2$) Mean | $\overline{\Delta q_{1'2}} = \lvert q_2 - q_{1'} \rvert$ | no | 0.85 |
| Distance parameter ($1' \rightarrow 2$) Sigma | $\sigma_{\Delta \mathrm{q}_{1'2}}$ | no | 0.3 |
| Metastable State 2 Energy Level Mean | $\overline{\mathcal{E}_{\mathrm{T}2'}}$ | no | 0.19 eV |
| Metastable State 2 Energy Level Sigma | $\sigma_{\mathcal{E}_{\mathrm{T}2'}}$ | no | 0.25 eV |
| Thermal Barrier 1 Mean | $\overline{\mathcal{E}_{11'}}$ | no | 1.5 eV |
| Thermal Barrier 1 Sigma | $\sigma_{\mathcal{E}_{11'}}$ | no | 0.36 eV |
| Thermal Barrier 2 Mean | $\overline{\mathcal{E}_{22'}}$ | no | 0.1 eV |
| Thermal Barrier 2 Sigma | $\sigma_{\mathcal{E}_{22'}}$ | no | 0.01 eV |
| Electron/Hole Capture Cross Section | $\sigma_{0,\mathrm{n,p}}$ | no | $4.5 \times 10^{-15}\,\mathrm{cm}^2$ |

Table 5.5: Set of adjusted parameters for the upper defect band in silicon dioxide for the modeling of oxide traps using the four-state NMP model.

These parameter values are unique properties of a given defect band in silicon dioxide, which remain unchanged for different devices and even for different channel materials. For all simulations the traps in the oxide were assumed to be hole traps. The arguments leading to this conclusion are summarized in Section 5.3.2. On devices with a silicon channel, another defect band situated $-1.5\,\mathrm{eV}$ below the defect band analyzed in this work was extracted [128]. Both defect bands together with the alignment of silicon and $MoS_2$ band gaps are shown in Figure 5.7(a). This figure illustrates the band alignment in the flatband case.

To emphasize the impact of oxide defects on the simulated transfer characteristics, Figure 5.7(b) shows a direct comparison of simulation results with and without oxide defects. First of all, using a four-state NMP model to describe oxide defects, a hysteresis in the transfer characteristics can be simulated. Without oxide defects there is no hysteresis at all and the up sweep and the down sweep overlap exactly. Furthermore, the permanently positive charged defects in the oxide cause a shift of the transfer char-

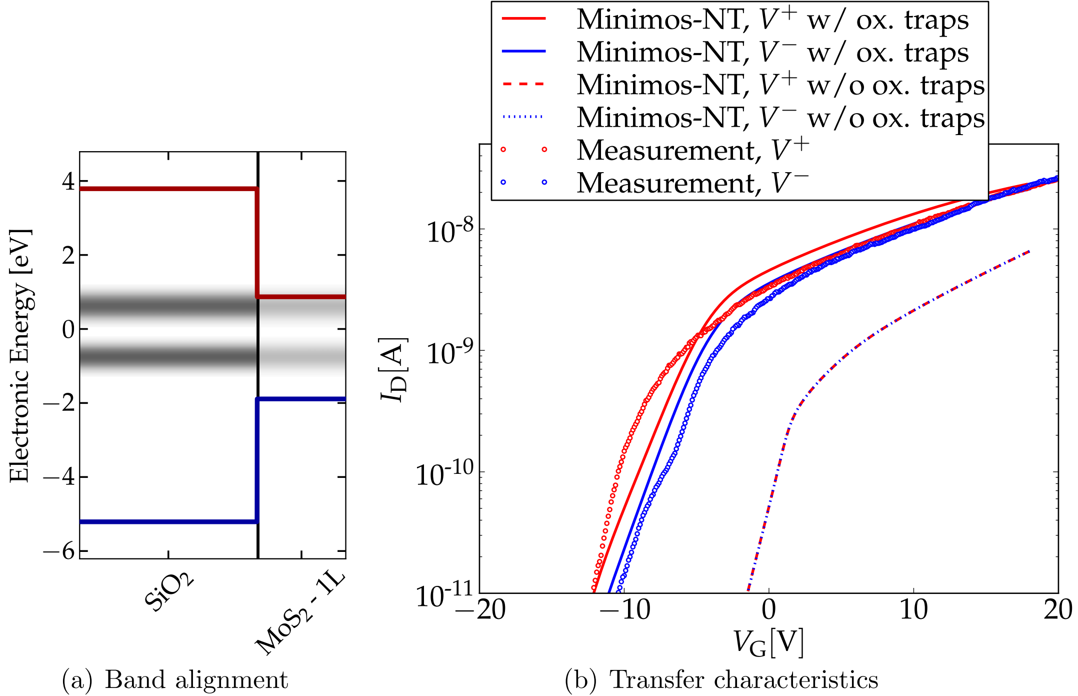


(a) Band alignment (b) Transfer characteristics

Figure 5.7: Oxide defect bands in silicon dioxide, as reported by Rzepa et al. [128] and as extracted in this work can be seen in Figure (a). In Figure (b) simulated transfer characteristics with and without oxide traps are compared with measured curves. The characteristics were measured at $T = 25\,°\mathrm{C}$ with $S = 0.2\,\mathrm{V/s}$ and a step voltage of $V_{\mathrm{step}} = 0.1\,\mathrm{V}$ on device A.

acteristic to lower gate voltages. It is obvious that the transfer characteristic in Figure 5.7(b) shows PBTI like hysteresis (compare Section 3.2.1). All hysteresis measurements were performed on device A at three different temperatures. The density of oxide traps $N_{\mathrm{ot}}$ was adjusted to obtain a good agreement with the measurements.

Figure 5.8(a) illustrates that when using the same oxide trap density of $6 \times 10^{19}\,\mathrm{cm}^{-3}$ for all temperature steps, the hysteresis at low temperatures is by far too small. Therefore, the oxide trap density has to be increased at lower temperatures. This behavior is best interpreted as a deactivation of oxide traps during the annealing process. The deactivation of oxide traps does not necessarily mean that there really are fewer oxide traps at higher temperatures. In contrast, it might be that only the time constants for charging the traps change such that at lower temperatures more traps can become neutralized during the up sweep, causing a larger hysteresis and a smaller threshold voltage shift(compare Section 3.2). In this case, the change of the oxide trap density only masks a temperature dependence of some of the barrier heights in the NMP model, as the time constants are defined by the rates implemented in the NMP model. The rates themselves then depend on the barrier heights for transitions between different states (see Section 4.4.8). Further investigations would have to reveal the exact mechanisms of the reduction of hysteresis at higher temperatures.

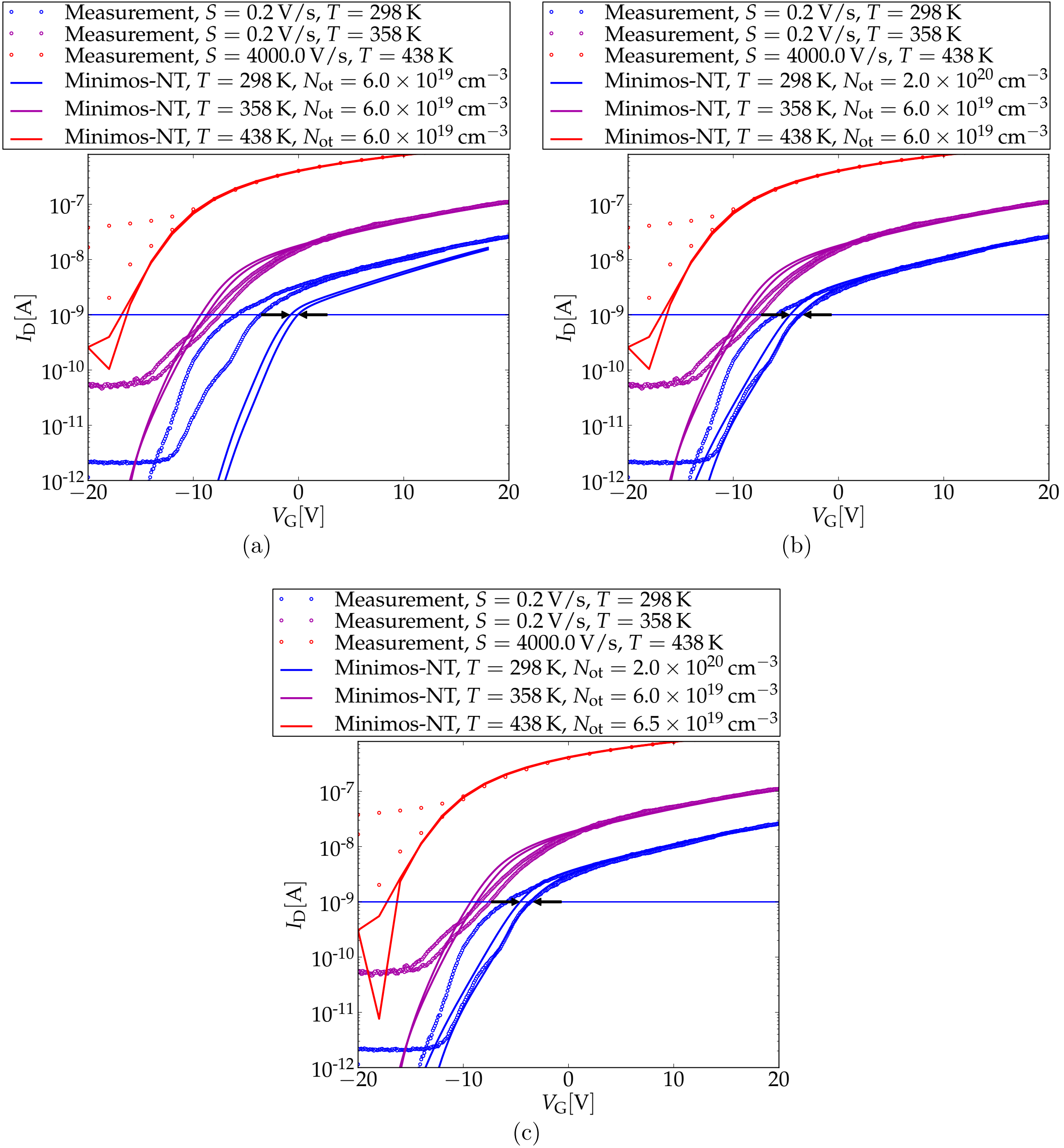


Figure 5.8: Simulated hysteresis characteristics using different concentrations of oxide defects at different temperatures. The characteristics were measured on device A. The black arrows indicate the hysteresis width calculated using a constant current criterion for the simulation at $T = 25\,°\mathrm{C}$. The calculation of the hysteresis width is discussed in Section 5.3.3.

The difference between Figures 5.8(b) and 5.8(c) is the density of oxide traps used to describe the transfer characteristic at 165 °C. To obtain a perfect fit, the oxide

trap density had to be increased slightly for the highest temperature. The adjustment is smaller than for the first temperature step, but it has to be made in the opposite direction. This might be related to the other time domain, which is analyzed now, as at 165 °C the characteristic was measured at a very high sweep rate. In any case the nonlinear temperature dependence of the oxide trap density points again towards a more complex mechanism, which is not fully understood yet.

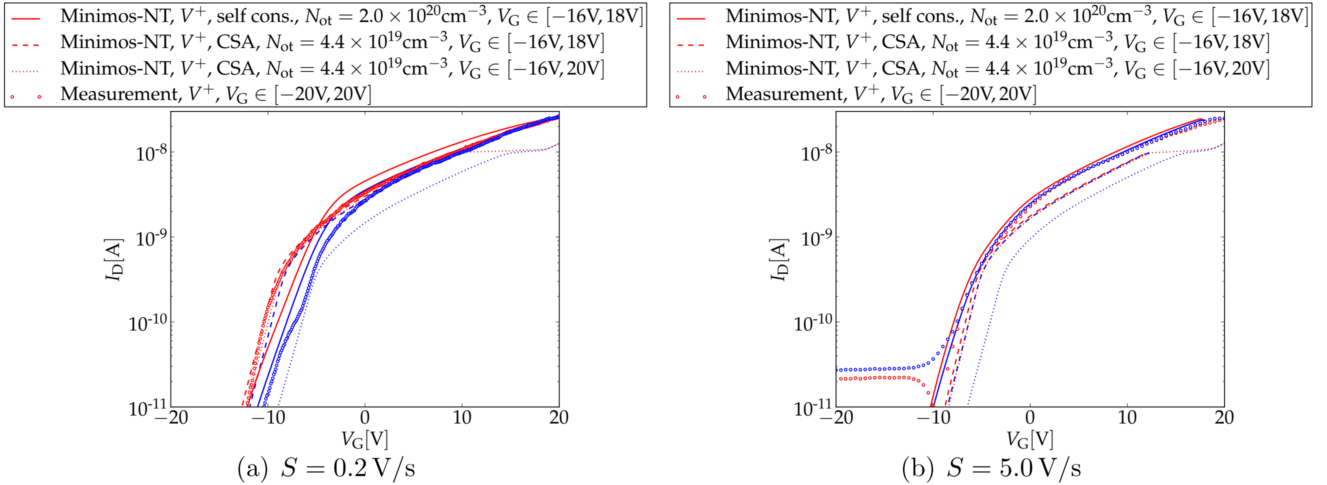


(a) $S = 0.2\,\mathrm{V/s}$ (b) $S = 5.0\,\mathrm{V/s}$

Figure 5.9: Comparison of simulated transfer characteristics on device A, at $T = 25\,°\mathrm{C}$ and $S = 0.2\,\mathrm{V/s}$ ($V_{\mathrm{step}} = 0.1\,\mathrm{V}$) or $S = 5.0\,\mathrm{V/s}$ ($V_{\mathrm{step}} = 0.5\,\mathrm{V}$) respectively. The simulation results are shown for different sweep ranges, which were obtained by using either self-consistent simulations or the CSA (see Section 4.4.9). The $V^-$ sweeps corresponding to the $V^+$ sweeps are colored blue.

Figure 5.9 shows the best simulation results obtained on device A, at 25 °C. It can be seen that our model can describe accurately the decline of the hysteresis width, which was observed when increasing the sweep rate $S$. Unfortunately especially when simulating a large hysteresis, numerical instabilities occured, which will now be briefly discussed.

In the derivation of the rates for the four-state NMP model, the so called band edge approximation was used to simplify Equations (4.58) to (4.61) to the form of Equations (4.64) to (4.67). In this approximation, parts of the integrals are evaluated at the band edges which can be crude for high electric fields. In this case, due to the shift of trap levels, more and more traps interact with more energetic charge carriers further away from the band edges which is neglected by the band edge approximation. So for large negative or positive gate voltages, the error introduced by the band edge approximation can become large. What is more, the simulation becomes numerically unstable for large positive or negative gate voltages. At negative gate voltages this is because of the very small amount of charge carriers in this voltage regime in nMOS devices. At high gate voltages this is caused by the large variations in the amount of charges in the oxide (compare Equation (4.98)). In self consistent simulations these charges are added to the

Poisson equation at every time step making it numerically unstable.

One possible way to avoid this problem is to limit the simulated sweep region to an interval smaller than the one used for measurements. However, it is widely acknowledged that the exact hysteresis width of an $MoS_2$ layer on silicon dioxide, depends strongly on the sweep range [108]. This is perfectly consistent with our theory, as by reducing the upper boundary of the sweep range, fewer defects can be neutralized during the up sweep, causing a smaller hysteresis (see Section 3.2). An increase of the lower boundary of the sweep range is expected to have a smaller impact on the hysteresis width, as it mainly reduces the overall sweep time $t_{\mathrm{m}}$ for a constant sweep rate $S$.

A second way of avoiding numerical instabilities at high gate voltages, is to use the charge sheet approximation, which was explained in Section 4.4.9. As the amount of charges in the oxide is not updated at every step of the iteration, strong variations in this quantity are not important anymore. Unfortunately the results obtained using the CSA are not very realistic. The obtained oxide trap density is by nearly one order of magnitude smaller than in the self consistent simulations. What is more, the dependence of the hysteresis width on the sweep rate $S$ decreases compared to self consistent simulations. As the dependence of the hysteresis width on the sweep rate $S$ is generally observed to be large, this effect increases the discrepancies between simulation and measurement. If the same sweep range as for the self consistent simulation is used for the CSA approximation, the hysteresis width obtained by the CSA is smaller. Still, the CSA can be used to analyze the trend when increasing the sweep range. Extending the sweep range up to 20 V increases the hysteresis width a lot, even if the feature in the characteristic at high voltages is probably an artifact.

Thus summing all up, it can be said that for hysteresis simulations the CSA is not very well suited. Therefore, one should try to perform self consistent simulations in any case possible. However, as the CSA reduces the computational effort, it might be used for qualtitative estimations. Finally, the fact that the hysteresis width estimated from self consistent simulations is smaller than the measured hysteresis width, should be attributed to the smaller sweeping range used in self consistent simulations. The hysteresis observed at $S = 5.0\,\mathrm{V/s}$ is not PBTI-like but NBTI-like. This cannot be modeled so far, but a qualitative explanation will be given at the end of the next section. In Figure 5.10 self consistent simulation results for the transfer characteristics measured at higher temperatures are presented.

## 5.3.1 Effect of Interface States

The accordance between measurement and simulation above threshold is in general good. However, what could not be modeled with the settings used up to this point are the characteristics below threshold. The measurement at 165 °C shows a pronounced hump at low voltages. For the measurements at 85 °C the current saturates for negative gate voltages and for measurements at 25 °C only during the down sweep a saturation of the current is observed. The features at low temperatures lie only at a few ten fA. A detailed investigation of these features is not reasonable, as they are close to the measurement accuracy, possibly being measurement artifacts. The hump at 165 °C on the other hand,

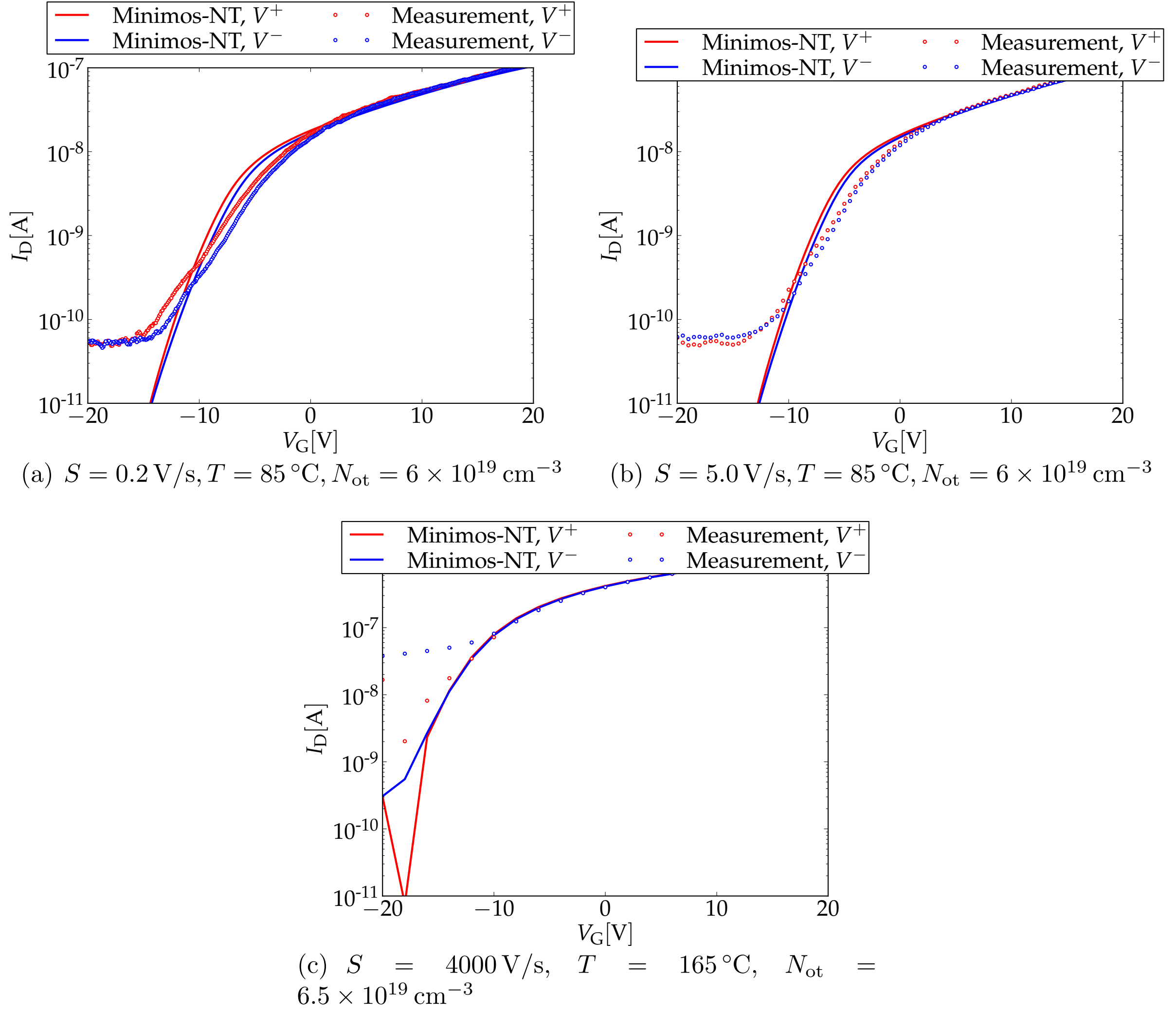


(a) $S = 0.2\,\mathrm{V/s}, T = 85\,°\mathrm{C}, N_{\mathrm{ot}} = 6 \times 10^{19}\,\mathrm{cm}^{-3}$ (b) $S = 5.0\,\mathrm{V/s}, T = 85\,°\mathrm{C}, N_{\mathrm{ot}} = 6 \times 10^{19}\,\mathrm{cm}^{-3}$

(c) $S = 4000\,\mathrm{V/s}$, $T = 165\,°\mathrm{C}$, $N_{\mathrm{ot}} = 6.5 \times 10^{19}\,\mathrm{cm}^{-3}$

Figure 5.10: Comparison of simulated transfer characteristics on device A, at $T = 85\,°\mathrm{C}$ in Figures (a) and (b) and at $T = 165\,°\mathrm{C}$ in Figure (c). The simulations were performed self consistently using different oxide trap densities, sweep rates and sweep ranges. The lower boundary of the sweep range amounted to $V_G = -16\,\mathrm{V}$ at $T = 85\,°\mathrm{C}$ and $V_G = -20\,\mathrm{V}$ at $T = 165\,°\mathrm{C}$. The decrease in the hysteresis width with increasing sweep rate $S$ was successfully modelled.

is of the magnitude of several nA, being certainly a real characteristic. In the following it will be shown that by changing the distribution and concentration of interface trap levels, the hump can be simulated correctly. The simulated transfer characteristics for different concentrations of interface traps at $T = 165\,°\mathrm{C}$ are shown in Figure 5.11.

At the vertex of the hump the drain current changes its sign. At very low gate voltages the electrons flow from drain to source and not the other way around. The hump can be reproduced in simulations if the interface trap density is increased significantly.

This can be explained by using the SRH model, which describes the charge carrier's

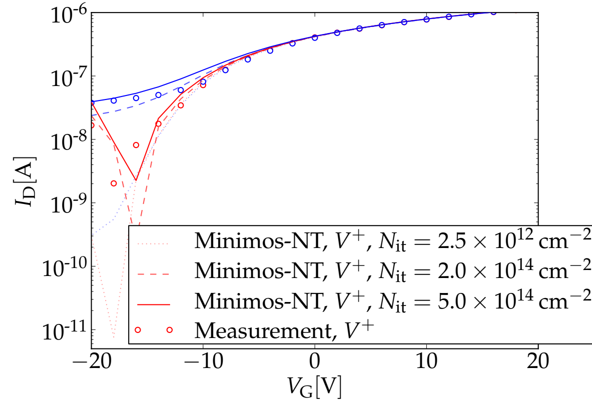


Figure 5.11: Simulation results obtained using different interface trap parameter sets. The characteristic was measured on device A, at $T = 165\,°C$ and $S = 4000\,V/s$ using a step voltage of $V_{step} = 2.0\,V$. Simulations were performed self consistently using $N_{ot} = 6.5 \times 10^{19}\,cm^{-3}$. The $V^-$ sweeps corresponding to the $V^+$ sweeps are colored blue.

interaction with interface defects, and the assumption that the concentration of interface defects is large around mid gap. For negative gate voltages, the Fermi level is located somewhere in the middle of the band gap, making generation and recombination of charge carriers especially effective. In the initial state many defects are missing an electron. As the gate voltage increases the Fermi level sweeps up towards the conduction band edge and many traps acquire an additional electron.

The negative sign of the drain current in this initial phase can be described equivalently in the electron or in the hole picture. In the electron picture the defects attract electrons not only from source but also from drain during the up sweep, leading in effect to a net current from drain to source. In the hole picture the generation of holes in the $MoS_2$ channel outweighs the generation of electrons, as more and more traps capture an electron. This leads to a temporary hole current towards drain which is the same as an electron current towards source. Finally, as the injection of electrons across the Schottky barrier at source increases for higher gate voltages, the effect of the interface states declines.

It has already been discussed in Section 5.2 that the interface traps close to the conduction band edge define the sub threshold slope. Up to now the distribution of interface trap levels was chosen such that the interface traps are strongly localized at the conduction band edge. The interface trap levels were placed at a sufficient distance from the band edge not to cause a threshold voltage shift, but so close that a minimum number of trap levels suffices to define the sub threshold slope. The parameter set defining the interface traps in the framework of the SRH model, is given in Table 5.3. This alignment of interface traps is shown in Figure 5.12(a). This Figure contains a set of oxide traps as well, randomly distributed according to the parameters in Table 5.5.

Increasing the density of interface traps using this distribution, causes only a decrease in the sub threshold slope but cannot model the hump, as the necessary defect states

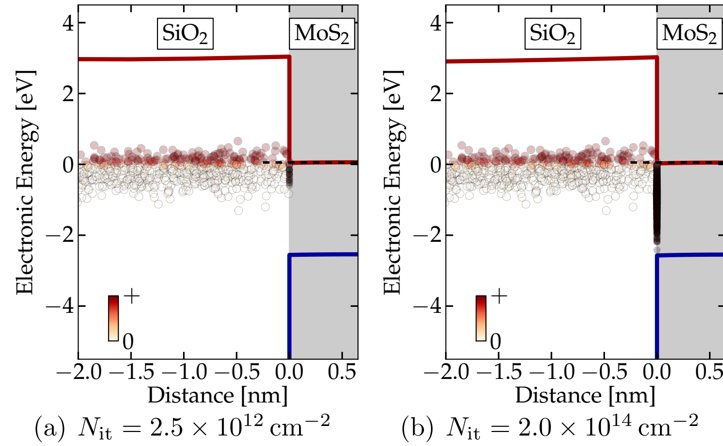


(a) $N_{\mathrm{it}} = 2.5 \times 10^{12}\,\mathrm{cm}^{-2}$ (b) $N_{\mathrm{it}} = 2.0 \times 10^{14}\,\mathrm{cm}^{-2}$

Figure 5.12: Comparison of band alignments including interface traps for different interface trap parameter sets. The donor like oxide traps are charged according to the colorbar in the lower left corner. The black dots at the interface stand for donor like interface traps.

in mid gap are missing. Therefore, the distribution of interface traps was changed to a broader distribution over the whole band gap. The new distribution of interface traps is shown in Figure 5.12(b).

The density of interface traps, showing the best accordance between simulated and measured $I_{\mathrm{D}}(V_{\mathrm{G}})$ at $T = 165\,°\mathrm{C}$, is as high as $N_{\mathrm{it}} = 5.0 \times 10^{14}\,\mathrm{cm}^{-2}$. Assuming that a monolayer is 5 Å thick, one obtains a volume density of defects of $1 \times 10^{28}\,\mathrm{m}^{-3}$. Furthermore, using the Avogardo constant ($N_{\mathrm{A}} = 6.022 \times 10^{23}\,\mathrm{mol}^{-1}$) and the molar volume of silicon ($V_{\mathrm{m}}(\mathrm{Si}) = 12.06 \times 10^{-6}\,\mathrm{m}^3/\mathrm{mol}$) [138], the approximate volume density of atoms can be calculated as $4.99 \times 10^{28}\,\mathrm{m}^{-3}$. This is the upper boundary for the volume density of atoms, as the silicon crystal shows the highest packing density. In reality atoms in an $MoS_2$ monolayer are not as densely packed as in a silicon crystal. Anyway, using this approximation the above interface trap density $N_{\mathrm{it}}$ corresponds to an interface defect at every fifth atom.

In the same way one can calculate the approximate number of atoms in the boundary layer of the amorphous silicon at the interface. The molar volume of silicon dioxide amounts to $V_{\mathrm{m}}(\mathrm{SiO_2}) = 29 \times 10^{-6}\,\mathrm{m}^3/\mathrm{mol}$ [139] which leads to a volume density of atoms of $2.08 \times 10^{28}\,\mathrm{m}^{-3}$. Therefore, a defect is located roughly at every second atom of the silicon dioxide boundary layer and at every fifth atom of the $MoS_2$ monolayer. This makes clear that an interface trap density of $N_{\mathrm{it}} = 5.0 \times 10^{14}\,\mathrm{cm}^{-2}$ is the upper limit which can be considered reasonable.

Thus, simulations were also done for an interface trap density of $N_{\mathrm{it}} = 2.0 \times 10^{14}\,\mathrm{cm}^{-2}$, corresponding to an interface defect at every twelfth atom of the $MoS_2$ monolayer. Just for comparison, using these approximations the initial interface trap density of $N_{\mathrm{it}} = 2.5 \times 10^{12}\,\mathrm{cm}^{-2}$ corresponds to a defect at every thousandth atom. The interface parameter sets used, are given in Table 5.6. The minimum and maximum defect

levels are the same in all three cases and are given in Table 5.3. In Figures 5.13 and 5.14 one can see simulated characteristics for various concentrations of interface traps at $T = 25\,°\mathrm{C}$ and $T = 85\,°\mathrm{C}$.

| $N_{\mathrm{it}}$ | $\overline{E}_{\mathrm{t}}$ | $\sigma_{\mathrm{t}}$ |
|---|---|---|
| $2.5 \times 10^{12}\,\mathrm{cm}^{-2}$ | $-3.94\,\mathrm{eV}$ | $0.3\,\mathrm{eV}$ |
| $2.0 \times 10^{14}\,\mathrm{cm}^{-2}$ | $-4.83\,\mathrm{eV}$ | $0.5\,\mathrm{eV}$ |
| $5.0 \times 10^{14}\,\mathrm{cm}^{-2}$ | $-4.83\,\mathrm{eV}$ | $0.44\,\mathrm{eV}$ |

Table 5.6: Different trap parameter sets used to model the hump in the sub threshold region of measured $I_{\mathrm{D}}(V_{\mathrm{G}})$ characteristics.

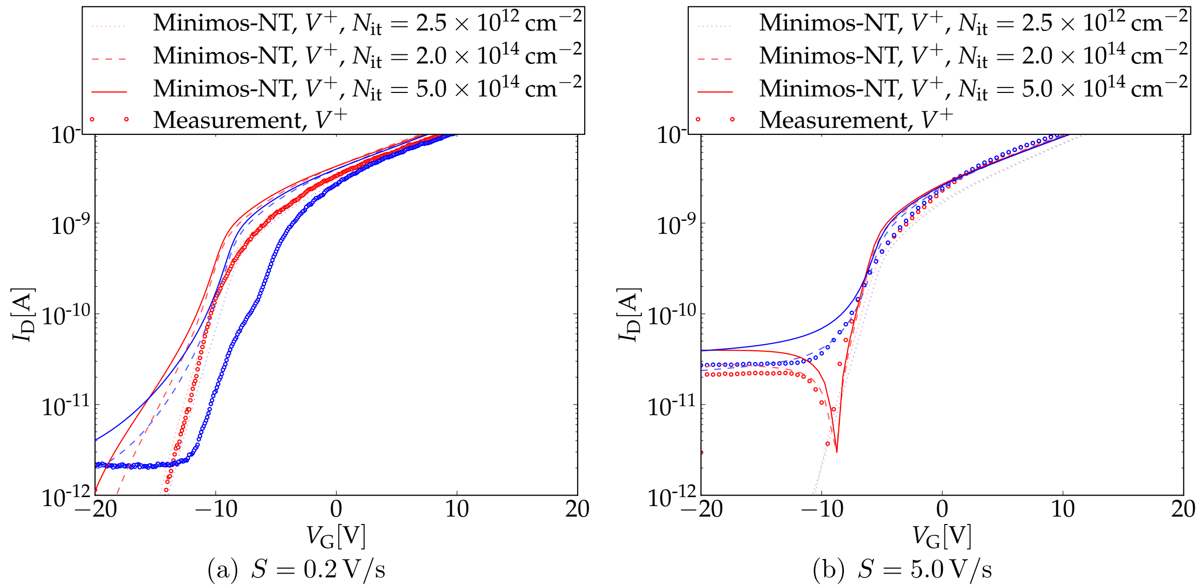


Figure 5.13: Comparison of simulated transfer characteristics using different interface trap parameter sets. The characteristics were measured on device A, at $T = 25\,°\mathrm{C}$ and $S = 0.2\,\mathrm{V/s}$ ($V_{\mathrm{step}} = 0.1\,\mathrm{V}$) or $S = 5.0\,\mathrm{V/s}$ ($V_{\mathrm{step}} = 0.5\,\mathrm{V}$) respectively. Simulations were performed using the CSA- approximation and $N_{\mathrm{ot}} = 4.4 \times 10^{19}\,\mathrm{cm}^{-3}$. The $V^-$ sweeps corresponding to the $V^+$ sweeps are colored blue.

Even if there might not be a perfect quantitative agreement between measured and simulated characteristics in Figure 5.13 due to the usage of CSA, the simulation results help in explaining the measured features below threshold. In Figure 5.13(a) the decline in the hysteresis width at around $-10\,\mathrm{V}$ is due to an increase in the current caused by the emission of electrons from the interface traps, as the Fermi level gradually scans over the upper part of the band gap. This effect also causes a crossover of the down sweep

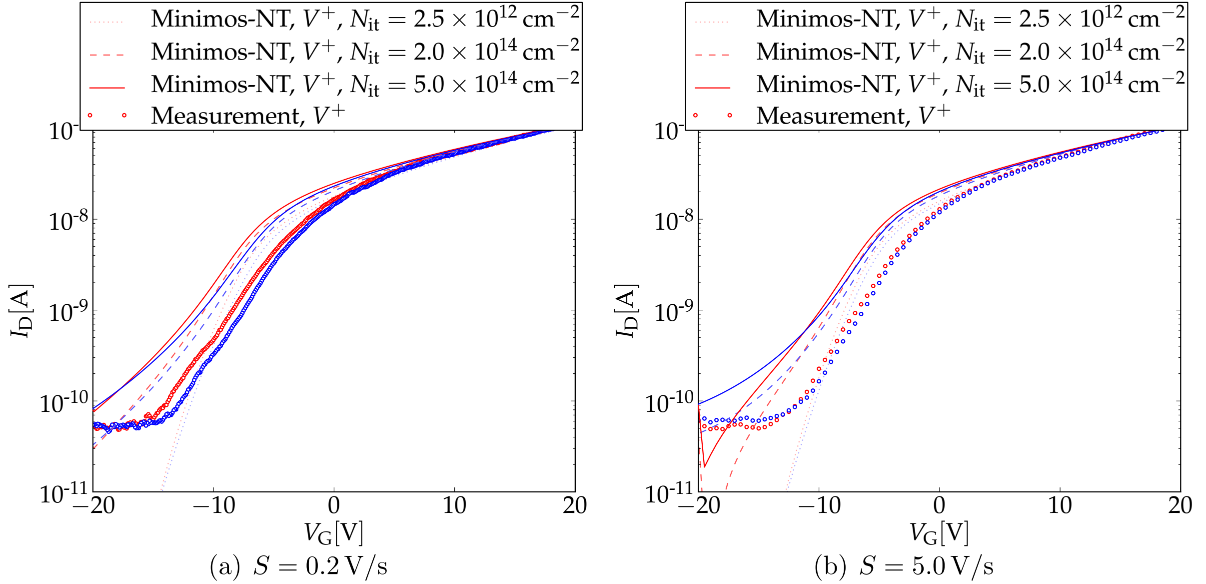


(a) $S = 0.2\,V/s$ (b) $S = 5.0\,V/s$

Figure 5.14: Comparison of simulated transfer characteristics using different interface trap parameter sets. The characteristics were measured on device A, at $T = 85\,°C$ and $S = 0.2\,V/s$ ($V_{step} = 0.1\,V$) or $S = 5.0\,V/s$ ($V_{step} = 0.5\,V$) respectively. Simulations were performed self consistently using $N_{ot} = 6.0 \times 10^{19}\,cm^{-3}$. The $V^-$ sweeps corresponding to the $V^+$ sweeps are colored blue.

with the up sweep, once the current caused by electron emission from traps becomes larger than the electron current injected over the Schottky barrier at source.

At the higher sweep rate in Figure 5.13(b) one can again see the hump caused by a change of the sign of the drain current at the beginning of the up sweep. Additionally, there is again a crossover between up sweep and down sweep at low voltages due to the additional charge carriers injected by the traps. Because of the higher sweep rate, the crossover takes place at voltages close to threshold and as the hysteresis is small, this leaves only a narrow voltage interval where the simulation results clearly exhibit PBTI-like hysteresis. Therefore, the NBTI-like hysteresis observed in the measured characteristic is probably caused by very dominant interface traps and a small hysteresis width.

In Figure 5.14, the interface traps lead to a saturation of the current at a low level, just as observed in the measurements. Again one can see that the intersection point between up and down sweep is shifted to higher voltages at higher sweep rates.

### 5.3.2 Oxide Defect Type

As the upper defect band in silicon dioxide has only become significant when describing the interaction of oxide traps with an $MoS_2$ layer, the type of the defect band has to be determined along with all other model parameters, given in Table 5.5. One distinguishes

between electron or acceptor-like traps, which are negatively charged when carrying an electron and neutral otherwise and hole or donor-like traps, which are neutral when carrying an electron and positively charged otherwise (see Section 4.3). To be able to directly compare a transfer characteristic with donor-like traps and one with acceptor-like traps, CSA has to be used because self-consistent simulations do not converge. In Figure 5.15(a) the results of self consistent simulations are compared to the results of the CSA to prove the applicability of the CSA in this case. The oxide trap density which has to be used in the charge sheet approximation to obtain similar results as for self consistent simulations, is always lower than the oxide trap density for self consistent simulations. For 165 °C it amounts to $N_{\mathrm{ot}} = 1.6 \times 10^{19}\,\mathrm{cm}^{-3}$.

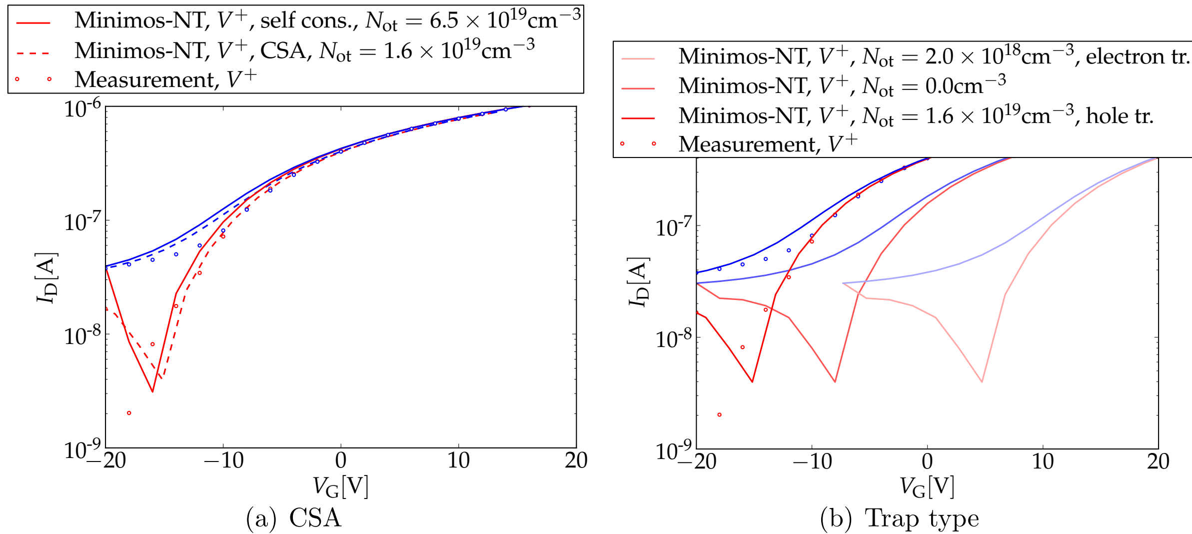


(a) CSA (b) Trap type

Figure 5.15: Simulated transfer characteristics at $T = 165\,°\mathrm{C}$ using the CSA or self-consistent simulations are shown in Figure (a). The CSA is necessary to be able to change the type of oxide traps. Simulated characteristics with different trap densities and trap types are shown in Figure (b). All simulations in this graph are using the CSA. The $V^-$ sweeps corresponding to the $V^+$ sweeps are colored blue.

Changing the trap type from hole traps to electron traps demonstrates that the negative charge of electron traps shifts the characteristic into the wrong direction. This behavior is shown in Figure 5.15(b). Compared to the case without any oxide traps, the characteristic is shifted towards lower voltages by positive charges and towards higher voltages by negative charges, in accordance with Equations (4.101) or (3.2). Thus the measurements show that there is a positive net charge in the vicinity of the channel. The interface charges have already been identified as donor like traps (see Figure 5.4(b)), which are neutral in the on state of the device and partially positively charged in the off state, thereby creating some positive charges in the vicinity of the channel.

The contribution of oxide traps to the positive net charge can be explained in two ways. The straightforward explanation is to state that the new defect band used in this

work is a hole trapping band. Another possible explanation is to define the band as an electron trapping band and to add a third defect band above the two other defect bands. This third defect band has to be a hole trapping band and the charges of this band have to overcompensate the negative charges introduced by the electron trapping band. As the first approach is easier and introduces fewer model parameters, this approach was used in this work.

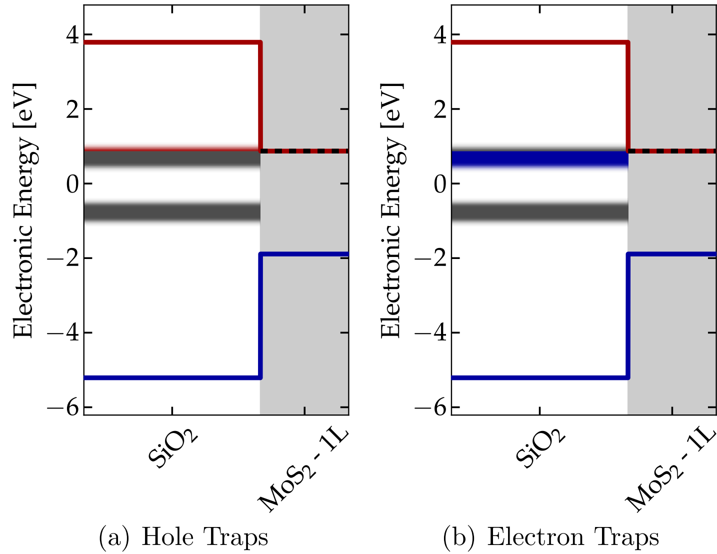


Figure 5.16: Band alignment with a hole trapping band (a) or an electron trapping band (b) as upper defect band. The lower defect band is in both cases a hole trapping band [128].

In Figure 5.16 the band diagram is shown, once using an electron trapping band as upper defect band and once using a hole trapping band. The band diagrams also make clear that due to the band alignment the same oxide trap density causes a larger shift if the traps are treated as electron traps instead of hole traps. Summing all up, interface traps and oxide traps are both modeled as donor like or hole traps in this work.

### 5.3.3 Hysteresis Width

At the end of this Section, after analyzing the impact of different parameters on simulations of hysteresis characteristics, the hysteresis width as a quantitative indicator for the quality of simulations was calculated. The hysteresis width is defined as the voltage difference between up sweep and down sweep measured at threshold voltage. This definition is not unambiguous because many different definitions exist for extracting the threshold voltage from measurement data [140]. In this work the constant current criterion defined by Lee et al. [141] was used. This criterion defines the threshold voltage as the voltage, at which the drain current $I_\mathrm{D}$, normalized by the channel width/length $(W/L)$ ratio, equals a predefined value $I_\mathrm{VT}$. On device A, where all hysteresis mea-

surements were made, the ratio amounts to $W/L = 6.8$. I applied the criterion using $I_{VT} = 0.15\,\mathrm{nA}$, which corresponds to a drain current of $I_D = 1.0\,\mathrm{nA}$. In this way the threshold voltage for up and down sweep was calculated and the evaluated hysteresis width for measured and simulated characteristics at 25 °C are presented in Table 5.7. The values obtained for the curves at 85 °C are shown in Table 5.8.

| | | | Hysteresis Width [V] | |
|---|---|---|---|---|
| | | | $S = 0.2\,\mathrm{Vs}^{-1}$ | $S = 5.0\,\mathrm{Vs}^{-1}$ |
| Measurement | | | 2.2 | 0.0 |
| self consistent, | $N_{it} = 2.5 \times 10^{12}\,\mathrm{cm}^{-2}$, | $V_G \in [-16\,\mathrm{V}, 18\,\mathrm{V}]$ | 0.9 | 0.5 |
| CSA, | $N_{it} = 2.5 \times 10^{12}\,\mathrm{cm}^{-2}$, | $V_G \in [-16\,\mathrm{V}, 18\,\mathrm{V}]$ | 0.7 | 0.0 |
| CSA, | $N_{it} = 2.5 \times 10^{12}\,\mathrm{cm}^{-2}$, | $V_G \in [-16\,\mathrm{V}, 20\,\mathrm{V}]$ | 3.7 | 2.0 |
| CSA, | $N_{it} = 2.0 \times 10^{14}\,\mathrm{cm}^{-2}$, | $V_G \in [-16\,\mathrm{V}, 18\,\mathrm{V}]$ | 0.8 | 0.0 |
| CSA, | $N_{it} = 5.0 \times 10^{14}\,\mathrm{cm}^{-2}$, | $V_G \in [-16\,\mathrm{V}, 18\,\mathrm{V}]$ | 0.8 | 0.5 |

Table 5.7: Hysteresis widths measured at a constant current $I_D = 1.0\,\mathrm{nA}$ for $T = 25$ °C.

| | | | Hysteresis Width [V] | |
|---|---|---|---|---|
| | | | $S = 0.2\,\mathrm{Vs}^{-1}$ | $S = 5.0\,\mathrm{Vs}^{-1}$ |
| Measurement | | | 0.9 | 0.5 |
| self consistent, | $N_{it} = 2.5 \times 10^{12}\,\mathrm{cm}^{-2}$, | $V_G \in [-16\,\mathrm{V}, 20\,\mathrm{V}]$ | 0.6 | 0.5 |
| self consistent, | $N_{it} = 2.0 \times 10^{14}\,\mathrm{cm}^{-2}$, | $V_G \in [-20\,\mathrm{V}, 20\,\mathrm{V}]$ | 0.8 | 0.5 |
| self consistent, | $N_{it} = 5.0 \times 10^{14}\,\mathrm{cm}^{-2}$, | $V_G \in [-20\,\mathrm{V}, 20\,\mathrm{V}]$ | 0.7 | 0.5 |

Table 5.8: Hysteresis widths measured at a constant current $I_D = 1.0\,\mathrm{nA}$ for $T = 85$ °C.

At 25 °C the agreement between measured and simulated widths is mediocre. This can be attributed to the convergence problems, which lead to the usage of the CSA and to a reduced sweep range. In any case, the calculated hysteresis widths make it plausible that one might obtain a perfect fit, if one could simulate the characteristic self consistently using the full sweep range and an interface trap density of $N_{it} = 2.0 \times 10^{14}\,\mathrm{cm}^{-2}$. At 85 °C the accordance between measured and simulated widths is very good when using an interface trap density of $N_{it} = 2.0 \times 10^{14}\,\mathrm{cm}^{-2}$.

## 5.4 Modeling of BTI Measurements

NBTI was measured on device B and PBTI was measured on device D. The complete measurement setup consists of stress and recovery cycles with several full $I_D(V_G)$ sweeps during recovery at the points where the threshold voltage shift $\Delta V_{th}$ is extracted (compare Sections 3.3.4 and 5.1). To reduce the computational effort only stress and recovery

cycles without including full $I_D(V_G)$ sweeps were simulated. In simulations the threshold voltage shift is obtained directly from the voltage shift calculated with the CSA (see Equation (4.101)).

The BTI is caused by the interaction of charge carriers with defects in the oxide. Therefore, the same parameter set for the four-state NMP model as extracted for the hysteresis measurements was used to model BTI measurements. The parameters of the four-state NMP model are given in Table 5.5. Other parameters like doping, device width or interface trap density differ from device to device. The special parameters for devices B and D used in the BTI simulations are listed in Table 5.4, only the density of fixed charges was set to zero for BTI simulations, because it is replaced by the oxide traps. The oxide trap density is a property of the silicon dioxide and is therefore assumed to be similar for all measurements at 85 °C. Small changes in the effective oxide defect density can be explained by the different annealing time, which the device was subjected to. When measuring the hysteresis, the devices had just been heated up to 85 °C. The PBTI measurement followed soon after that, but then there was an additional cooling and reheating cycle before NBTI was measured. (see Figures 5.1) For both PBTI and NBTI measurements the oxide trap density was set to $N_{ot} = 8 \times 10^{19}\,\mathrm{cm}^{-3}$, which is close to the value of $N_{ot} = 6 \times 10^{19}\,\mathrm{cm}^{-3}$ used for hysteresis simulations on device A at 85 °C.

Due to the small current at the high negative voltage level NBTI simulations on nMOS devices tend to be numerically unstable. To increase the current in the negative voltage region and thereby to improve the numerical stability, it is important to perform the simulations self consistently. When applying negative stress voltages, there are more positive charges in the channel, causing a higher current in the low voltage region. However, the simulations remain unstable at $V_G^H = -20.0\,\mathrm{V}$. Therefore, the high level voltages of $V_G^H = \pm 20.0\,\mathrm{V}$ used for measurements were replaced by $V_G^H = \pm 16.0\,\mathrm{V}$ in the simulations.

The reduction of the high voltage levels serves another purpose as well. As already discussed in Section 5.3, the band edge approximation is used in all simulations, which introduces larger errors for very high or very low stress voltages. To keep the errors caused by the band edge approximation on a reasonable scale, the high level voltages should be reduced for simulations.

In the measurements the gate contact was floating during the recovery cycles. This floating potential is difficult to model in the simulations. In Minimos-NT one can define floating contacts, which are characterized by the fact that after an initializing step the charge on the contacts remains constant. Therefore, by setting the gate contact to a floating contact in simulations there is no recovery at all, but a permanent stress due to the charge on the gate contact. This is not what happens in measurements, where there are always leakage currents flowing away from the gate contact. These currents establish an equilibrium voltage at the gate contact, enabling a recovery of the device.

A better approach to modeling floating contacts is to make a good guess for the equilibrium voltage $V_G^L$ and to set the gate contact during the recovery cycle to this voltage. Still, the equilibrium voltage $V_G^L$ is not known. For simplicity it is assumed that the equilibrium voltage during the floating phases is the same as the initial equilibrium voltage of

the device before applying any stress $V_G^L \approx V_{G,init}$. The value for $V_{G,init}$ depends on many factors like for example the processing of the devices. Our BTI simulations indicate that a value of $V_G^L = 6.5\,V$ is most reasonable. The BTI results for this value of the equilibrium voltage are shown in Figure 5.17. These graphs confirm that with one physically consistent defect band the output characteristics including hysteresis measurements and NBTI as well as PBTI can be reproduced.

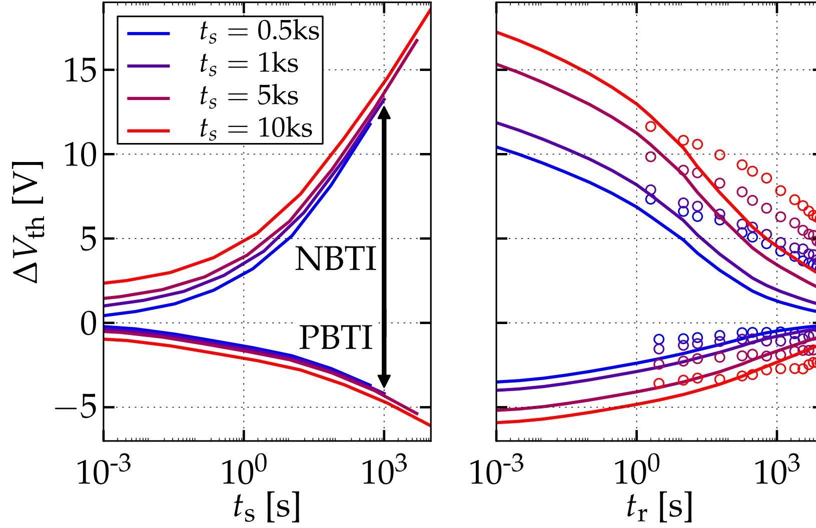


Figure 5.17: Measured and simulated threshold voltage shifts of a BTI Measurement at $T = 85\,°C$. The circles are the discrete measurement points. In Minimos-NT simulations complete stress and recovery curves can be calculated and are shown in the plots as solid lines. For simulations $V_G^L = 6.5\,V$ was used.

The band alignment during the simulation of PBTI using $V_G^L = 6.5\,V$ is shown in Figure 5.18. In the four graphs the charging and decharging process of the traps during the measurement is illustrated. At first, the device is initialized using $V_G^L = 6.5\,V$ as equilibrium voltage. It can be seen that this gate voltage is close to the flatband voltage. The next time step shows the situation at the end of the stress cycle. Some traps which have formerly been positively charged are now neutral, because they have emitted a hole. In the following graph the gate voltage has just switched back to equilibrium value, changing Fermi level and band alignment but not the charge state of the traps. The Fermi level is indicated as a dashed black line in the channel of the $MoS_2$ monolayer. The last time step which is presented shows that after a sufficiently long recovery period, nearly all traps have returned to their initial charge state. In these plots one can see that the Fermi level is shifted only by a small amount due to strong Fermi level pinning. The band alignment during NBTI simulations using the same setting is shown in Figure 5.19.

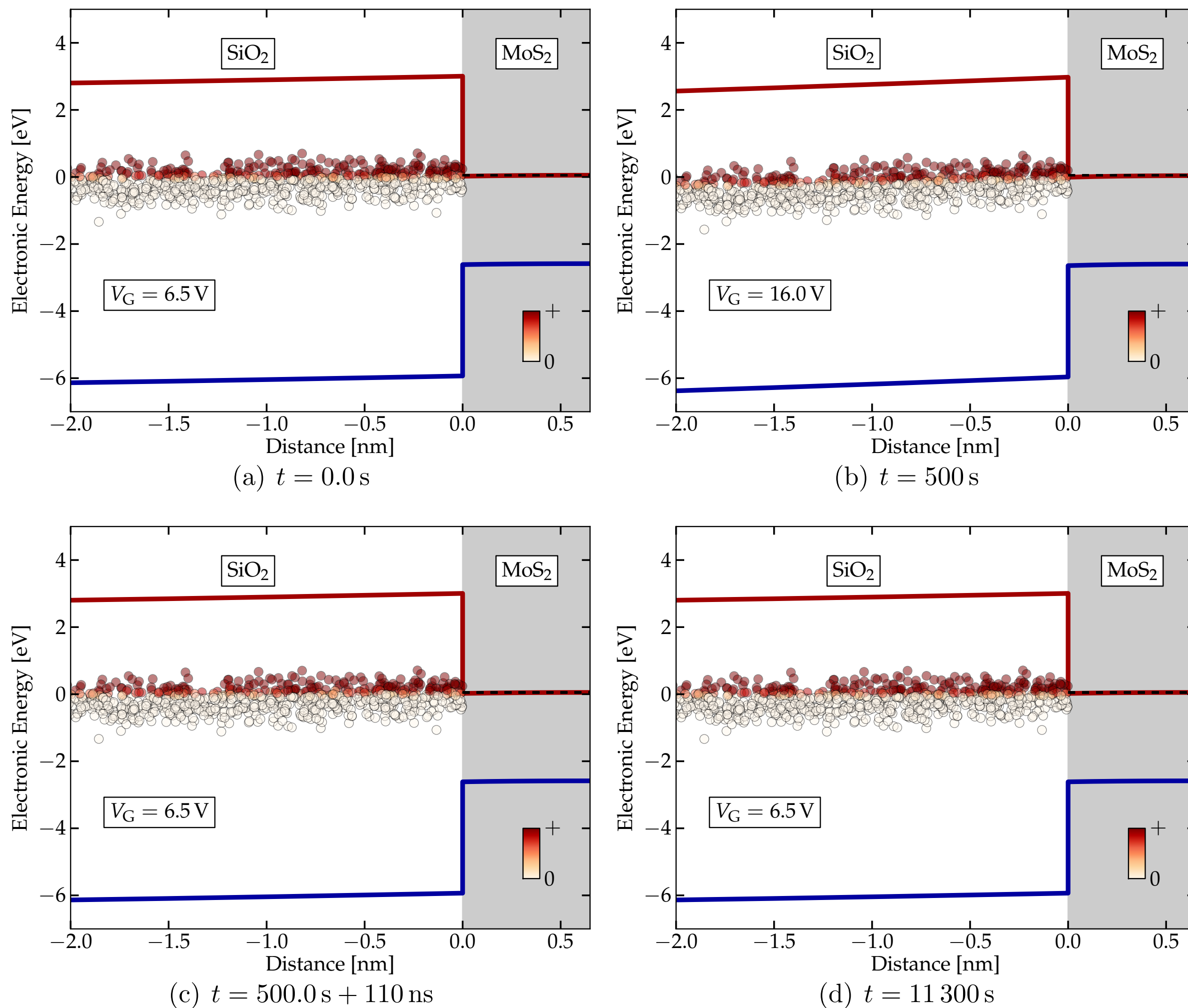


(a) $t = 0.0\,s$ (b) $t = 500\,s$ (c) $t = 500.0\,s + 110\,ns$ (d) $t = 11\,300\,s$

Figure 5.18: Band diagrams showing the charge state of oxide traps during a PBTI measurement on device D at $T = 85\,°C$ using $V_G^L = 6.5\,V$. Shortly after $t = 0.0\,s$, the first stress phase starts, which lasts 500 s. Next, there is a recovery period of 10 000 s before the next stress period starts shortly after $t = 11\,300\,s$.

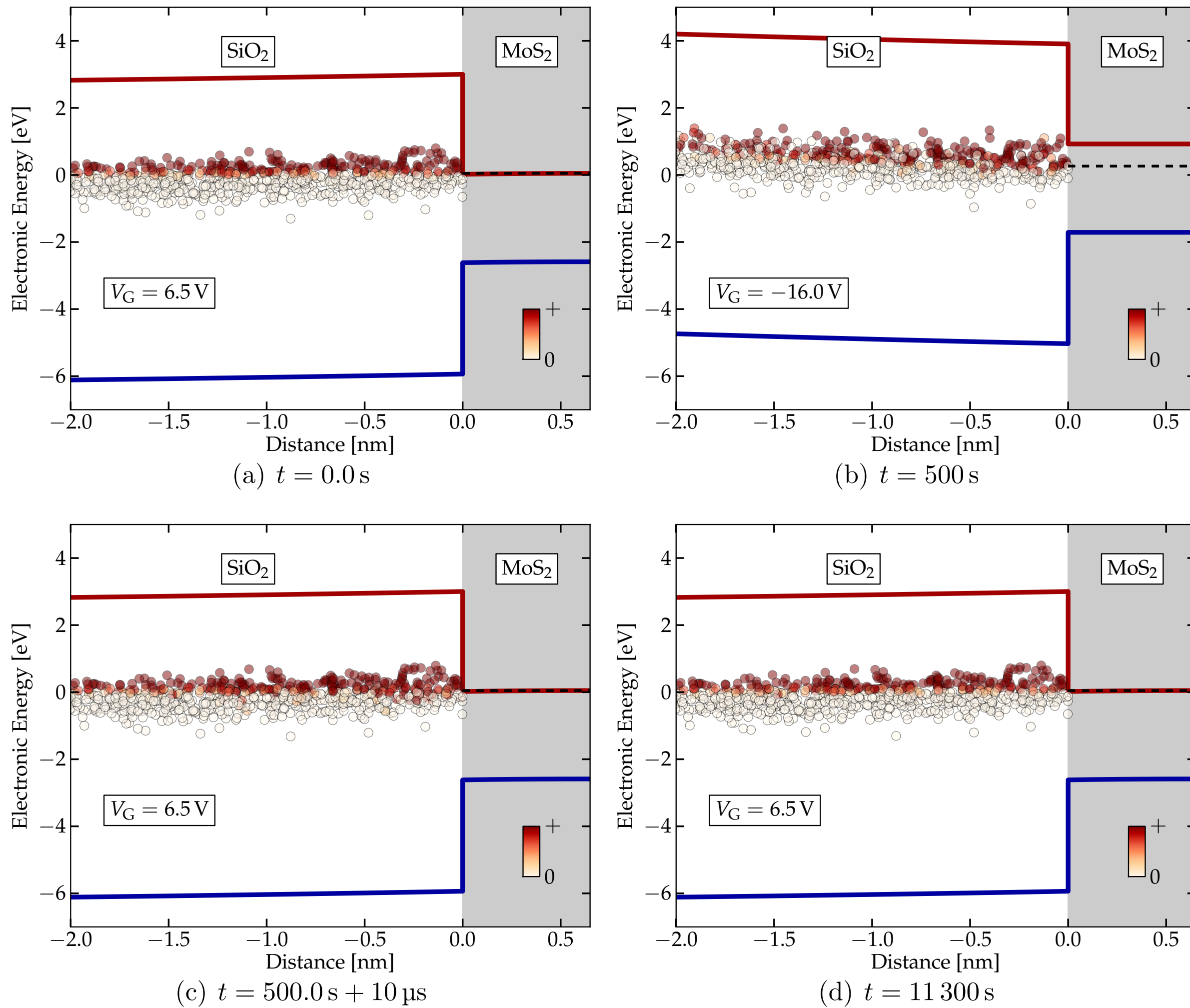


(a) $t = 0.0\,\mathrm{s}$ (b) $t = 500\,\mathrm{s}$ (c) $t = 500.0\,\mathrm{s} + 10\,\mu\mathrm{s}$ (d) $t = 11\,300\,\mathrm{s}$

Figure 5.19: Band diagrams showing the charge state of oxide traps during a NBTI measurement on device B at $T = 85\,°\mathrm{C}$ using $V_\mathrm{G}^\mathrm{L} = 6.5\,\mathrm{V}$. Shortly after $t = 0.0\,\mathrm{s}$, the first stress phase starts, which lasts $500\,\mathrm{s}$. Next, there is a recovery period of $10\,000\,\mathrm{s}$ before the next stress period starts shortly after $t = 11\,300\,\mathrm{s}$.

# CHAPTER 6 Conclusions

In this work it is demonstrated that the drift-diffusion model can be successfully applied to novel devices based on monolayers of, for example, $MoS_2$ (see Section 5.2). This is an important finding as it validates the applicability of conventional TCAD tools for simulation of 2D channel devices and is therefore an important step towards industrial maturity of these novel device concepts.

In Section 2 the material parameters which constitute the inputs for drift-diffusion simulations are thoroughly analysed. At this point some new physics come into play, causing numerous dependencies of quantities which for conventional three-dimensional materials have been known as constants. For example in the case of two-dimensional materials the band structure shows dominant excitonic effects and depends sensitively on surrounding materials. I have analysed these effects based on an extensive literature research of both, experimental and theoretical studies (see Section 2.3). Another speciality of two-dimensional channel materials is the close relation between transistor properties and its contacts. In this context it has been shown that most contact materials exhibit strong Fermi level pinning when used together with TMDs and usually form Schottky barriers (see Section 2.5). Therefore, the drain current flow is strongly affected by the contacts, making such quantities as effective carrier mobility or doping density highly dependent on them (see Section 5.2). The intrinsic mobility of the monolayer remains unaffected by the contacts but typically cannot be reached in transistor operation.

One main concern about the applicability of the classical, large scale drift-diffusion model to devices based on two-dimensional materials was the, to the model inherent, neglection of quantum mechanical effects. Nevertheless, it could be shown that at the current development stage of the devices, where the current flow is governed by scattering events, quantum mechanical confinement has a negligible impact (see Section 4.2).

As only devices which can perform reliably have ever reached maturity, a main focus of this work lay on the analysis of reliability-related issues like hysteresis effects which are observed on devices using $MoS_2$ monolayers as a channel. I argued that the observed hysteresis is primarily caused by the interaction of charge carriers with defects in the underlying amorphous $SiO_2$ layer. The main arguments in this regard are the time scale on which this phenomenon can be observed (see Section 3.2) and the successful modeling of the hysteresis, using a four-state NMP model to describe the interaction of charge carriers with oxide traps (see Section 5.3). While hysteresis measurements

stress the devices on a broad range of voltages for a narrow window of time intervals, BTI measurements stress the devices at discrete voltages but on longer time scales. Therefore, both measurement techniques target at analysing the interaction between charge carriers and defects in the oxide, but they do that for completely different ranges of stressing voltages and times. In consequence, it is a strong validation of the theoretical framework presented in this work that both effects can be modeled consistently using this framework (see Sections 5.3 and 5.4).

The extraction of the parameters of the four-state NMP model serves another purpose besides the mere modeling of characteristics: It provides the location of the defect bands in $SiO_2$. These defect bands are a material property of the silicon dioxide and therefore indicate which materials might be able to perform reliably. If the conduction and valence band edges of the channel material are located in the middle of a defect band, there will always be a strong interaction between charge carriers and the defects. If on the other hand the band edge is away far enough from the defect bands, the interaction of charge carriers with defects in the oxide becomes small, leading to small hysteresis and BTI degradation. Analysing the band alignment of the $MoS_2$ monolayer to $SiO_2$ in this respect (see Figure 5.7(a)) reveals that an nMOS $MoS_2$ transistor on $SiO_2$ can probably never perform reliably, whereas a pMOS $MoS_2$ transistor on $SiO_2$ could perform well, if there is no further defect band below the two which have been investigated up to now. This question will have to be answered by future investigations.

Apart from oxide defects, also defects at the interface between the monolayer and the silicon dioxide have been studied in this work (see Section 4.3). I have shown that the role of interface defects mainly governs the sub threshold region of the characteristics (see Section 5.3.1). The density of interface states observed in this work is very high, but future improvements of processing technology might help to reduce it.

## 6.1 Outlook

The new findings reported here are certainly not the end but rather the start point of a multitude of investigations related to the reliability of two-dimensional channel materials. In order to further validate the theory that hysteresis and BTI are caused by the same defects, the dependence of the hysteresis width on the sweep frequency (see Figure 3.5) should be modeled and the BTI measurement procedure should be simulated in a more detailed setup to be able to determine the equilibrium gate voltage. Another idea, which could be addressed, is that the hybridization of the $MoS_2$ monolayer below the contacts could be modeled more realistically by using an increased, inhomogeneous doping profile below the contacts.

The weakest point of this work is certainly that all parameters were extracted only from a very limited set of four devices fabricated in one process. To be able to prove the generality of the reported findings, it is indispensable to study a larger variety of devices from different fabrication processes using different transistor structures and different material combinations. In this context a more detailed and thorough extraction of NMP parameters for the upper defect band in $SiO_2$ using also other channel materials will be necessary.

On the long run, it might be interesting to take a closer look at the four-state NMP model using Morse potentials and benchmark it for a variety of different devices against the conventional four-state NMP model using harmonic potentials. If devices based on two-dimensional channel materials reach a more mature stage, it could be interesting to take a closer look at the quantities, which seem to vary from device to device, like the effective mobility or the doping density and develop a new physics-based model to describe these variations.

Summing all up, the applicability of the drift-diffusion model to FETs based on two-dimensional channel materials is demonstrated, paving the way for future investigations using this powerful tool. Furthermore, it could be demonstrated that some huge problems of this new technology like a hysteresis in transfer characteristics can be related to the interaction of charge carriers with traps in surrounding dielectrics and could extract an additional defect band in $SiO_2$ which might help in identifying promising future material systems. The results presented in this work show that even if the studied system of a $MoS_2$ monolayer on $SiO_2$ might not reach maturity in the end, transistors based on two-dimensional TMD layers can work reliably and might one day be able to replace conventional silicon transistors.

# APPENDIX A Data

## A.1 Experimental Band Gaps

| Substrate | Source | $E_{\mathrm{G}}$ | $E_{\mathrm{OPT}}$ | $E_{\mathrm{EXC}}$ |
|---|---|---|---|---|
| BLG | [11] | 2.18(4) eV (STS) | 1.63(1) eV (PL) | 0.55(4) eV |
| HOPG ($\epsilon_{\mathrm{r}} \approx 11$ [43]) | [11] | 1.94(4) eV (STS) | 1.67(3) eV (PL) | 0.27(5) eV |
| suspended ($\epsilon_{\mathrm{r}} = 1$) | [26] | - | 1.68 eV (PS) | - |
| $SiO_2$ ($\epsilon_{\mathrm{r}} \approx 3.9$) | [32] | - | 1.64 eV (PL) | - |
| | [37] | - | 1.66 eV (PL) | - |

Table A.1: Experimentally obtained values for the band gap in single layer $MoSe_2$ (BLG = bilayered graphene). $T = 77\,\mathrm{K}$ for all measurements.

| Substrate | Source | $E_{\mathrm{G}}$ | $E_{\mathrm{OPT}}$ | $E_{\mathrm{EXC}}$ |
|---|---|---|---|---|
| $SiO_2$ ($\epsilon_{\mathrm{r}} \approx 3.9$) | [142] | 2.910(2) eV (Refl.) | 2.078(2) eV (Refl.) | 0.830(2) eV |
| | [143] | 2.73 eV$^{\star}$ (TP-PLE) | 2.02 eV$^{\star}$ (PL) | 0.71(1) eV$^{\star}$ |
| | [144] | $> 2.48$ eV (TP-PLE) | 2.0 eV (Abs.) | $> 0.44$ eV |

Table A.2: Experimentally obtained values for the band gap in single layer $WS_2$ (Refl. = reflectivity measurement,TP-PLE = two-photon photoluminescence excitation spectroscopy). $T = 77\,\mathrm{K}$ for all measurements except for those marked with "$\star$", where $T = 293\,\mathrm{K}$.

In a reflectivity measurement the light from a broad-band light source is reflected from the monolayer and the intensity of the reflected light is analysed as a function of the photon energy.

In two-photon photoluminescence excitation spectroscopy, one shines pulsed laser light with half the frequency of the allowed two-photon transition on the sample. Two-

photon excitation is a third order optical process, where two photons are simulatenously absorbed to excite one electron. The selection rules for these processes forbid transitions to s-states, which is why only excited p-states in the excitonic spectrum can be probed. [144] By analysing the spectrum of p states a lower boundary for the excitonic binding energy can be given or when looking for the onset of a linear rise in the spectrum one can as well determine the electronic band gap. [143]

| Substrate | Source | $E_{\mathrm{G}}$ | $E_{\mathrm{OPT}}$ | $E_{\mathrm{EXC}}$ |
|---|---|---|---|---|
| HOPG ($\epsilon_{\mathrm{r}} \approx 11$ [43]) | [145] | 2.08(1) eV | - | - |
| $SiO_2$ ($\epsilon_{\mathrm{r}} \approx 3.9$) | [142] | 2.533(4) eV (Refl.) | 1.740(4) eV (Refl.) | 0.790(4) eV |
| | [146] | $> 2.02$ eV$^\star$ (TP-PLE) | 1.65 eV$^\star$ (Abs., PL) | $> 0.37$ eV$^\star$ |
| suspended ($\epsilon_{\mathrm{r}} = 1$) | [26] | - | 1.7 eV (PS) | - |

Table A.3: Experimentally obtained values for the band gap in single layer $WSe_2$. $T =$ 77 K for all measurements except for those marked with "⋆", where $T =$ 293 K.

| $N$ | Substrate | Source | $E_{\mathrm{G}}{}^{\mathrm{d}}$ | $E_{\mathrm{G}}{}^{\mathrm{i}}$ | $E_{\mathrm{OPT}}{}^{\mathrm{d}}$ | $E_{\mathrm{OPT}}{}^{\mathrm{i}}$ |
|---|---|---|---|---|---|---|
| 2 | BLG | [29] | - | 1.56(4) eV (STS) | - | - |
| 3 | BLG | [29] | - | 1.32(4) eV (STS) | - | - |
| bulk | - | [46] | - | - | 1.38 eV (PS) | 1.09 eV (PS) |

Table A.4: Experimentally obtained values for the band gap in multilayer $MoSe_2$.

In Table A.5 a positive sign of the band offset indicates that the band edge of the second material lies above the band edge of the first material, whereas a negative sign states that the band edge of the second material lies below the band edge of the first material. In an internal photoemission measurement, electrons from a semiconducting material are excited across a dielectric barrier using laser light. At the photon energy corresponding to the barrier height the yield starts to increase exponentially. [148]

| Substrate | Source | stacking | 1st Band | 2nd Band | Offset |
|---|---|---|---|---|---|
| HOPG | [145] (STS) | lateral | 2L $MoSe_2$ CB | 1L $MoSe_2$ CB | 0.08(10) eV |
| | | | 2L $MoSe_2$ VB | 1L $MoSe_2$ VB | −0.43(10) eV |
| | | | 2L $WSe_2$ CB | 1L $WSe_2$ CB | 0.15(10) eV |
| | | | 2L $WSe_2$ VB | 1L $WSe_2$ VB | −0.12(10) eV |
| | [44] (STS, XPS) | vertical | 1L $WSe_2$ CB | 1L $MoS_2$ CB | −0.76(12) eV |
| | | | 1L $WSe_2$ VB | 1L $MoS_2$ VB | −0.83(7) eV |
| $SiO_2$ | [147] ($I_D(V_G)$) | vertical | 1L $MoS_2$ CB | Graphene | −0.29 eV |
| | [148] (IPE) | vertical | bulk $SiO_2$ CB | 4L $MoS_2$ VB | −4.2 eV |
| | | vertical | 2nm $HfO_2$ CB | 4L $MoS_2$ VB | −3.7 eV |
| | [22] (IPE) | vertical | bulk $SiO_2$ CB | 4L $MoS_2$ VB | −4.2(1) eV |
| | | vertical | 4L $WS_2$ CB | 4L $MoS_2$ VB | 0.0(1) eV |

Table A.5: Experimentally obtained values for the band offsets (CB = conduction band, VB = valence band, IPE = internal photoemission).

## A.2 DFT Band Gaps

| Source | Method | SOC | Coulomb | $\epsilon_M$ | $L$ | k-Point | $a$ | $E_G$ | $E_{OPT}$ | $E_{EXC}$ | $\chi$ |
|---|---|---|---|---|---|---|---|---|---|---|---|
| [13] | LDA+$G_0W_0$+MW | yes | truncated | 2D | 20 Å | 30x30x1 | 3.32 Å | 2.18 eV | 1.76 eV | 0.42 eV | −3.46 eV |
| [11] | LDA+$G_0W_0$+BSE | yes | truncated | 3D | 25 Å | 12x12x1 | 3.29 Å | 2.26 eV | 1.61 eV | 0.65 eV | - |
| [29] | LDA+$G_0W_0$ | yes | truncated | 3D | 50 Å | 12x12x1 | 3.29 Å | 2.25 eV | - | - | - |
| [63] | PBE+$G_0W_0$ | yes | truncated | 3D | 17 Å | 12x12x1 | 3.33 Å | 1.98 eV | - | - | −3.22 eV |
| [64] | PBE+$G_0W_0$ | no | truncated | 3D | 23 Å | 12x12x1 | 3.31 Å | 2.33 eV | - | - | −3.36 eV |
| [65] | HSE+$G_0W_0$+BSE | yes | full | 3D | 15 Å | 6x6x1 | 3.32 Å | 2.41 eV | 1.66 eV | 0.75 eV | - |
| [66] | PBE+$G_0W_0$+BSE | no | full | 3D | 15 Å | 11x11x1 | 3.29 Å | 2.39 eV | 2.2 eV | 0.19 eV | −3.58 eV |

Table A.6: DFT results for the band structure of monolayer $MoSe_2$. All results refer to vacuum environment, $T = 0\,K$.

| Source | Method | SOC | Coulomb | $\epsilon_M$ | $L$ | k-Point | $a$ | $E_G$ | $E_{OPT}$ | $E_{EXC}$ | $\chi$ |
|---|---|---|---|---|---|---|---|---|---|---|---|
| [13] | LDA+$G_0W_0$+MW | yes | truncated | 2D | 20 Å | 30x30x1 | 3.19 Å | 2.43 eV | 1.95 eV | 0.48 eV | −4.73 eV |
| [63] | PBE+$G_0W_0$ | yes | truncated | 3D | 17 Å | 12x12x1 | 3.19 Å | 2.31 eV | - | - | −3.58 eV |
| [64] | PBE+$G_0W_0$ | no | truncated | 3D | 23 Å | 12x12x1 | 3.20 Å | 2.88 eV | - | - | −3.53 eV |
| [65] | HSE+$G_0W_0$+BSE | yes | full | 3D | 15 Å | 6x6x1 | 3.19 Å | 2.88 eV | 2.17 eV | 0.71 eV | - |
| [66] | PBE+$G_0W_0$+BSE | no | full | 3D | 15 Å | 11x11x1 | 3.16 Å | 2.94 eV | 2.5 eV | 0.44 eV | −3.53 eV |
| [40] | PBE+$G_0W_0$+BSE | no | full | 3D | 19 Å | 15x15x1 | 3.16 Å | 3.05 eV | 2.51 eV | 0.54 eV | - |

Table A.7: DFT results for the band structure of monolayer $WS_2$. All results refer to vacuum environment, $T = 0\,K$.

| Source | Method | SOC | Coulomb | $\epsilon_M$ | $L$ | k-Point | $a$ | $E_G$ | $E_{OPT}$ | $E_{EXC}$ | $\chi$ |
|---|---|---|---|---|---|---|---|---|---|---|---|
| [13] | LDA+$G_0W_0$+MW | yes | truncated | 2D | 20 Å | 30x30x1 | 3.32 Å | 2.08 eV | 1.65 eV | 0.43 eV | −3.85 eV |
| [63] | PBE+$G_0W_0$ | yes | truncated | 3D | 17 Å | 12x12x1 | 3.32 Å | 1.98 eV | - | - | −3.22 eV |
| [64] | PBE+$G_0W_0$ | no | truncated | 3D | 23 Å | 12x12x1 | 3.33 Å | 2.38 eV | - | - | −3.17 eV |
| [65] | HSE+$G_0W_0$+BSE | yes | full | 3D | 15 Å | 6x6x1 | 3.32 Å | 2.42 eV | 1.75 eV | 0.67 eV | - |
| [66] | PBE+$G_0W_0$+BSE | no | full | 3D | 15 Å | 11x11x1 | 3.26 Å | 2.7 eV | 2.6 eV | 0.1 eV | −3.14 eV |

Table A.8: DFT results for the band structure of monolayer $WSe_2$. All results refer to vacuum environment, $T = 0\,K$.

| N | St. | Source | Method | Coulomb | $L$[Å] | k-Point | $a/c$[Å] | $E_G{}^{d}/{}^{i}$[eV] | $E_{OPT}{}^{d}/{}^{i}$[eV] | $E_{EXC}{}^{d}$[eV] | $\chi$[eV] |
|---|---|---|---|---|---|---|---|---|---|---|---|
| 2 | 2H | [29] | LDA+$G_0W_0$ (!) | truncated | 50 | 12x12x1 | 3.29/- | 2.2/1.85 | -/- | - | - |
| 3 | 2H | [29] | LDA+$G_0W_0$ (!) | truncated | 50 | 12x12x1 | 3.29/- | 2.1/1.7 | -/- | - | - |
| B | 2H | [52] | PBE+$GW_0$ (!) | full | 15 | 12x12x2 | 3.29/12.93 | 1.39/0.84 | -/- | - | -5.08 |

Table A.9: DFT results for the band structure of multilayer $MoSe_2$. All calculations were performed using the three dimensional form of the dielectric constant. Spin-orbit coupling is taken into account in all of the listed calculations. An exclamation mark (!) behind a method is used to underline that in these calculations Van der Waals interactions were not accounted for.

| N | St. | Source | Substrate | $E_G{}^{d}/{}^{i}$[eV] | $E_{OPT}{}^{d}/{}^{i}$[eV] | $E_{EXC}{}^{d}$[eV] |
|---|---|---|---|---|---|---|
| 1 | 2H | [11] | BLG | 2.13/2.13 | 1.61/1.61 | 0.52 |
| 1 | 2H | [29] | BLG | 2.05/2.05 | -/- | - |
| 2 | 2H | [29] | BLG | 2.03/1.65 | -/- | - |
| 3 | 2H | [29] | BLG | 2.0/1.46 | -/- | - |

Table A.10: DFT results for the band structure of $MoSe_2$ on different substrates. The DFT parameters are the same as given for references [11] [29] in Table A.6.

## A.3 Effective Masses

| Material | Source | $m^*_\mathrm{n}/m_0$ | $m^*_\mathrm{p}/m_0$ |
|---|---|---|---|
| $MoSe_2$ | [13] | 0.49 | 0.61 |
| $MoSe_2$ | [65] | 0.7 | 0.55 |
| $MoSe_2$2 | [40] | 0.38 | 0.44 |
| $WS_2$ | [13] | 0.46 | 0.42 |
| $WS_2$ | [65] | 0.44 | 0.45 |
| $WS_2$ | [40] | 0.27 | 0.32 |
| $WSe_2$ | [13] | 0.48 | 0.44 |
| $WSe_2$ | [65] | 0.53 | 0.52 |
| $WSe_2$ | [40] | 0.29 | 0.34 |

Table A.11: Effective masses for charge carriers in monolayer $MoSe_2$, $WS_2$ and $WSe_2$ ($m_0$ stands for the electron mass in vacuum).

# Bibliography

[1] P. Zhao, S. Desai, M. Tosun, T. Roy, H. Fang, A. Sachid, M. Amani, C. Hu, and A. Javey, "2D layered materials: From materials properties to device applications," *Technical Digest - International Electron Devices Meeting, IEDM*, vol. 27.3.1, pp. 699–700, 2015.

[2] K. Novoselov, A. Geim, S. Morozov, D. Jiang, Y. Zhang, S. Dubonos, I. Grigorieva, and A. A. Firsov, "Electric field effect in atomically thin carbon films." *Science*, vol. 306, pp. 666–669, 2004.

[3] K. I. Bolotin, K. J. Sikes, Z. Jiang, M. Klima, G. Fudenberg, J. Hone, P. Kim, and H. L. Stormer, "Ultrahigh electron mobility in suspended graphene," *Solid State Communications*, vol. 146, no. 9-10, pp. 351–355, 2008.

[4] L. Liao, Y.-C. Lin, M. Bao, R. Cheng, J. Bai, Y. Liu, Y. Qu, K. L. Wang, Y. Huang, and X. Duan, "High-speed graphene transistors with a self-aligned nanowire gate," *Nature*, vol. 467, no. 7313, pp. 305–8, 2010.

[5] M. Y. Han, B. Özyilmaz, Y. Zhang, and P. Kim, "Energy band-gap engineering of graphene nanoribbons," *Physical Review Letters*, vol. 98, no. 20, pp. 1–4, 2007.

[6] Y. Zhang, T.-T. Tang, C. Girit, Z. Hao, M. C. Martin, A. Zettl, M. F. Crommie, Y. R. Shen, and F. Wang, "Direct observation of a widely tunable bandgap in bilayer graphene." *Nature*, vol. 459, no. 7248, pp. 820–3, 2009.

[7] B. Radisavljevic, A. Radenovic, J. Brivio, V. Giacometti, and A. Kis, "Single-layer MoS2 transistors," *Nature nanotechnology*, vol. 6, no. 3, pp. 147–50, 2011.

[8] Y. Yoon, K. Ganapathi, and S. Salahuddin, "How good can monolayer MoS2 transistors be?" *Nano letters*, vol. 11, no. 9, pp. 3768–73, 2011.

[9] X. Cui, G.-H. Lee, Y. D. Kim, G. Arefe, P. Y. Huang, C.-h. Lee, D. A. Chenet, X. Zhang, L. Wang, F. Ye, F. Pizzocchero, B. S. Jessen, K. Watanabe, T. Taniguchi, D. A. Muller, T. Low, P. Kim, and J. Hone, "Multi-terminal transport measurements of MoS2 using a van der Waals heterostructure device platform," *Nature Nanotechnology*, vol. 10, no. 6, pp. 534–540, 2015.

[10] X. Chen, Y. Wu, Z. Wu, Y. Han, S. Xu, L. Wang, W. Ye, T. Han, Y. He, Y. Cai, and N. Wang, "High-quality sandwiched black phosphorus heterostructure and its quantum oscillations," *Nature Communications*, vol. 6, p. 7315, 2015.

[11] M. M. Ugeda, A. J. Bradley, S.-f. Shi, F. H. Jornada, Y. Zhang, D. Y. Qiu, W. Ruan, S.-k. Mo, Z. Hussain, Z.-x. Shen, F. Wang, S. G. Louie, and M. F. Crommie, "Giant bandgap renormalization and excitonic effects in a monolayer transition metal dichalcogenide semiconductor," *Nature materials*, vol. 13, no. December, pp. 1091–1095, 2014.

[12] Q. H. Wang, K. Kalantar-Zadeh, A. Kis, J. N. Coleman, and M. S. Strano, "Electronics and optoelectronics of two-dimensional transition metal dichalcogenides," *Nature Nanotechnology*, vol. 7, no. 11, pp. 699–712, 2012.

[13] F. A. Rasmussen and K. S. Thygesen, "Computational 2D Materials Database: Electronic Structure of Transition-Metal Dichalcogenides and Oxides," *Journal of Physical Chemistry C*, vol. 119, no. 23, pp. 13 169–13 183, 2015.

[14] G. Eda, H. Yamaguchi, D. Voiry, T. Fujita, M. Chen, and M. Chhowalla, "Photoluminescence from Chemically Exfoliated MoS2," *Nano Lett.*, vol. 12, p. 526, 2012.

[15] M. M. Benameur, B. Radisavljevic, J. S. Héron, S. Sahoo, H. Berger, and A. Kis, "Visibility of dichalcogenide nanolayers." *Nanotechnology*, vol. 22, no. 12, p. 125706, 2011.

[16] V. Nicolosi, M. Chhowalla, M. G. Kanatzidis, M. S. Strano, and J. N. Coleman, "Liquid Exfoliation of Layered Materials," *Science*, vol. 340, no. 6139, p. 1226419, 2013.

[17] Z. Zeng, Z. Yin, X. Huang, H. Li, Q. He, G. Lu, F. Boey, and H. Zhang, "Single-layer semiconducting nanosheets: High-yield preparation and device fabrication," *Angewandte Chemie - International Edition*, vol. 50, no. 47, pp. 11 093–11 097, 2011.

[18] Y. H. Lee, X. Q. Zhang, W. Zhang, M. T. Chang, C. T. Lin, K. D. Chang, Y. C. Yu, J. T. W. Wang, C. S. Chang, L. J. Li, and T. W. Lin, "Synthesis of large-area MoS 2 atomic layers with chemical vapor deposition," *Advanced Materials*, vol. 24, no. 17, pp. 2320–2325, 2012.

[19] S. Najmaei, Z. Liu, W. Zhou, X. Zou, G. Shi, S. Lei, B. I. Yakobson, J.-C. Idrobo, P. M. Ajayan, and J. Lou, "Vapor Phase Growth and Grain Boundary Structure of Molybdenum Disulfide Atomic Layers," *Nature materials*, vol. 12, no. 8, pp. 754–759, 2013.

[20] A. M. van der Zande, P. Y. Huang, D. a. Chenet, T. C. Berkelbach, Y. You, G.-H. Lee, T. F. Heinz, D. R. Reichman, D. a. Muller, and J. C. Hone, "Grains and

grain boundaries in highly crystalline monolayer molybdenum disulphide." *Nature materials*, vol. 12, no. 6, pp. 554–61, 2013.

[21] M. Amani, M. L. Chin, A. G. Birdwell, T. P. O'Regan, S. Najmaei, Z. Liu, P. M. Ajayan, J. Lou, and M. Dubey, "Electrical performance of monolayer MoS2 field-effect transistors prepared by chemical vapor deposition," *Applied Physics Letters*, vol. 102, no. 19, 2013.

[22] D. Chiappe, I. Asselberghs, S. Sutar, S. Iacovo, V. Afanas'ev, A. Stesmans, Y. Balaji, L. Peters, M. Heyne, M. Mannarino, W. Vandervorst, S. Sayan, C. Huyghebaert, M. Caymax, M. Heyns, S. De Gendt, I. Radu, and A. Thean, "Controlled Sulfurization Process for the Synthesis of Large Area MoS 2 Films and MoS 2 /WS 2 Heterostructures," *Advanced Materials Interfaces*, vol. 3, no. 4, 2015.

[23] Y. Zhan, Z. Liu, S. Najmaei, P. M. Ajayan, and J. Lou, "Large-area vapor-phase growth and characterization of MoS 2 atomic layers on a SiO 2 substrate," *Small*, vol. 8, no. 7, pp. 966–971, 2012.

[24] T. Cheiwchanchamnangij and W. R. L. Lambrecht, "Quasiparticle band structure calculation of monolayer , bilayer , and bulk MoS 2," *Physical Review B*, vol. 85, no. 205302, pp. 1–4, 2012.

[25] K. F. Mak, K. He, C. Lee, G. H. Lee, J. Hone, T. F. Heinz, and J. Shan, "Tightly bound trions in monolayer MoS2." *Nature materials*, vol. 12, no. 3, pp. 207–11, 2013.

[26] A. R. Klots, A. K. M. Newaz, B. Wang, D. Prasai, H. Krzyzanowska, J. Lin, D. Caudel, N. J. Ghimire, J. Yan, B. L. Ivanov, K. A. Velizhanin, A. Burger, D. G. Mandrus, N. H. Tolk, S. T. Pantelides, and K. I. Bolotin, "Probing excitonic states in suspended two-dimensional semiconductors by photocurrent spectroscopy," *Scientific Reports*, vol. 4, p. 6608, 2014.

[27] C. Zhang, A. Johnson, C.-l. Hsu, L.-j. Li, and C.-k. Shih, "Direct Imaging of Band Pro fi le in Single Layer MoS 2 on Graphite: Quasiparticle Energy Gap, Metallic Edge States, and Edge Band Bending," *Nano Letters*, 2014.

[28] H. P. Komsa and A. V. Krasheninnikov, "Effects of confinement and environment on the electronic structure and exciton binding energy of MoS2 from first principles," *Physical Review B - Condensed Matter and Materials Physics*, vol. 86, no. 24, pp. 1–6, 2012.

[29] A. J. Bradley, M. M. Ugeda, F. H. Da Jornada, D. Y. Qiu, W. Ruan, Y. Zhang, S. Wickenburg, A. Riss, J. Lu, S. K. Mo, Z. Hussain, Z. X. Shen, S. G. Louie, and M. F. Crommie, "Probing the Role of Interlayer Coupling and Coulomb Interactions on Electronic Structure in Few-Layer MoSe2 Nanostructures," *Nano Letters*, vol. 15, no. 4, pp. 2594–2599, 2015.

[30] C. Delerue, G. Allan, and M. Lannoo, "Dimensionality-Dependent Self-Energy Corrections and Exchange-Correlation Potential in Semiconductor Nanostructures," *Physical Review Letters*, vol. 90, no. 7, pp. 0–3, 2003.

[31] K. F. Mak, C. Lee, J. Hone, J. Shan, and T. F. Heinz, "Atomically thin MoS2: A new direct-gap semiconductor," *Physical Review Letters*, vol. 105, no. 13, pp. 2–5, 2010.

[32] S. Tongay, J. Zhou, C. Ataca, K. Lo, T. S. Matthews, J. Li, J. C. Grossman, and J. Wu, "Thermally Driven Crossover from Indirect toward Direct Bandgap in 2D Semiconductors: MoSe2 versus MoS2," *Nano Lett.*, vol. 12, no. 11, pp. 5576–5580, 2012.

[33] Y. Ding, Y. Wang, J. Ni, L. Shi, S. Shi, and W. Tang, "First principles study of structural, vibrational and electronic properties of graphene-like MX2 (M=Mo, Nb, W, Ta; X=S, Se, Te) monolayers," *Physica B: Condensed Matter*, vol. 406, no. 11, pp. 2254–2260, 2011.

[34] S. W. Han, H. Kwon, S. K. Kim, S. Ryu, W. S. Yun, D. H. Kim, J. H. Hwang, J. S. Kang, J. Baik, H. J. Shin, and S. C. Hong, "Band-gap transition induced by interlayer van der Waals interaction in MoS2," *Physical Review B - Condensed Matter and Materials Physics*, vol. 84, no. 4, pp. 17–22, 2011.

[35] L. Debbichi, O. Eriksson, and S. Lebègue, "Electronic structure of two-dimensional transition metal dichalcogenide bilayers from ab initio theory," *Physical Review B*, vol. 89, no. 20, p. 205311, 2014.

[36] A. M. Van Der Zande, J. Kunstmann, A. Chernikov, D. A. Chenet, Y. You, X. Zhang, P. Y. Huang, T. C. Berkelbach, L. Wang, F. Zhang, M. S. Hybertsen, D. A. Muller, D. R. Reichman, T. F. Heinz, and J. C. Hone, "Tailoring the electronic structure in bilayer molybdenum disulfide via interlayer twist," *Nano Letters*, vol. 14, no. 7, pp. 3869–3875, 2014.

[37] J. S. Ross, S. Wu, H. Yu, N. J. Ghimire, A. M. Jones, G. Aivazian, J. Yan, D. G. Mandrus, D. Xiao, W. Yao, and X. Xu, "Electrical control of neutral and charged excitons in a monolayer semiconductor." *Nature communications*, vol. 4, p. 1474, 2013.

[38] K. P. O'Donnell and X. Chen, "Temperature dependence of semiconductor band gaps," *Applied Physics Letters*, vol. 58, no. 25, pp. 2924–2926, 1991.

[39] K. He, C. Poole, K. F. Mak, and J. Shan, "Experimental demonstration of continuous electronic structure tuning via strain in atomically thin MoS2," *Nano Letters*, vol. 13, no. 6, pp. 2931–2936, 2013.

[40] H. Shi, H. Pan, Y. W. Zhang, and B. I. Yakobson, "Quasiparticle band structures and optical properties of strained monolayer MoS2 and WS2," *Physical Review B - Condensed Matter and Materials Physics*, vol. 87, no. 15, pp. 1–8, 2013.

[41] H. M. Hill, A. F. Rigosi, K. T. Rim, G. W. Flynn, and T. F. Heinz, “Band alignment in MoS 2 /WS 2 transition metal dichalcogenide heterostructures probed by scanning tunneling microscopy and spectroscopy,” *Nano Letters*, 2016.

[42] H. J. Conley, B. Wang, J. I. Ziegler, R. F. Haglund, S. T. Pantelides, and K. I. Bolotin, “Bandgap Engineering of Strained Monolayer and Bilayer MoS 2,” *Nano Letters*, vol. 13, no. 8, pp. 3626–3630, 2013.

[43] G. E. Jellison, J. D. Hunn, and H. N. Lee, “Measurement of optical functions of highly oriented pyrolytic graphite in the visible,” *Physical Review B - Condensed Matter and Materials Physics*, vol. 76, no. August, pp. 05 125: 1–8, 2007.

[44] M.-h. Chiu, C. Zhang, H.-w. Shiu, C.-p. Chuu, C.-H. Chen, C.-y. S. Chang, C.-h. Chen, M.-y. Chou, C.-k. Shih, and L.-j. Li, “Determination of band alignment in the single-layer MoS2/WSe2 heterojunction.” *Nature communications*, vol. 6, no. May, p. 7666, 2015.

[45] A. Splendiani, L. Sun, Y. Zhang, T. Li, J. Kim, C. Y. Chim, G. Galli, and F. Wang, “Emerging photoluminescence in monolayer MoS2,” *Nano Letters*, vol. 10, no. 4, pp. 1271–1275, 2010.

[46] K. Kam and B. A. Parkinson, “Detailed Photocurrent Spectroscopy,” *Journal of Physical Chemistry*, vol. 86, no. 4, pp. 463–467, 1982.

[47] Andreas Garhofer, “Ab Initio Studies of Graphene-Metal Interfaces,” Ph.D. dissertation, Vienna University of Technology, 2013.

[48] W. Kohn, “Nobel Lecture: Electronic structure of matter—wave functions and density functionals,” *Reviews of Modern Physics*, vol. 71, no. 5, pp. 1253–1266, 1999.

[49] W. Kohn and L. Sham, “Self-Consistent Equations Including Exchange and Correlation Effects,” *Physical Review*, vol. 140, no. 1965, pp. 1133–1138, 1965.

[50] D. M. Ceperley and B. J. Alder, “Ground state of the electron gas by a stochastic model,” *Physical Review Letters*, vol. 45, no. 7, pp. 566–569, 1980.

[51] J. P. Perdew, K. Burke, and M. Ernzerhof, “Generalized Gradient Approximation Made Simple,” *Physical Review Letters*, vol. 77, no. 18, pp. 3865–3868, 1996.

[52] H. Jiang, “Electronic band structures of molybdenum and tungsten dichalcogenides by the GW approach,” *Journal of Physical Chemistry C*, vol. 116, no. 14, pp. 7664–7671, 2012.

[53] F. Aryasetiawan, “The GW method,” *Rep. Prog. Phys.*, vol. 61, pp. 237–312, 1998.

[54] F. Hüser, T. Olsen, and K. S. Thygesen, "How dielectric screening in two-dimensional crystals affects the convergence of excited-state calculations: Monolayer MoS2," *Physical Review B - Condensed Matter and Materials Physics*, vol. 88, no. 24, pp. 1–9, 2013.

[55] E. E. Salpeter and H. A. Bethe, "A relativistic equation for bound-state problems," *Physical Review*, vol. 84, no. 6, pp. 1232–1242, 1951.

[56] G. Strinati, "Dynamical shift and broadening of core excitons in semiconductors," *Physical Review Letters*, vol. 49, no. 20, pp. 1519–1522, 1982.

[57] M. Rohlfing and S. Louie, "Electron-hole excitations and optical spectra from first principles," *Physical Review B*, vol. 62, no. 8, pp. 4927–4944, 2000.

[58] A. Molina-Sanchez, D. Sangalli, K. Hummer, A. Marini, and L. Wirtz, "Effect of spin-orbit interaction on the optical spectra of single-layer, double-layer, and bulk MoS2," *Physical Review B - Condensed Matter and Materials Physics*, vol. 88, no. 4, pp. 1–6, 2013.

[59] D. Y. Qiu, F. H. da Jornada, and S. G. Louie, "Screening and Many-Body Effects in Two-Dimensional Crystals: Monolayer MoS2," *Physical Review B*, vol. 93, p. 235435, 2016.

[60] J. Heyd, G. E. Scuseria, and M. Ernzerhof, "Hybrid functionals based on a screened Coulomb potential," *Journal of Chemical Physics*, vol. 118, no. 18, pp. 8207–8215, 2003.

[61] F. A. Rasmussen, P. S. Schmidt, K. T. Winther, and K. S. Thygesen, "Efficient many-body calculations of 2D materials using exact limits for the screened potential: Band gaps of MoS$_2$, hBN, and phosphorene," vol. 00, 2016.

[62] R. Soklaski, Y. Liang, and L. Yang, "Temperature effect on optical spectra of monolayer molybdenum disulfide," *Applied Physics Letters*, vol. 104, no. 19, 2014.

[63] C. Gong, H. Zhang, W. Wang, L. Colombo, R. M. Wallace, and K. Cho, "Band alignment of two-dimensional transition metal dichalcogenides: Application in tunnel field effect transistors," *Applied Physics Letters*, vol. 103, no. 5, 2013.

[64] Y. Liang, S. Huang, R. Soklaski, and L. Yang, "Quasiparticle band-edge energy and band offsets of monolayer of molybdenum and tungsten chalcogenides," *Applied Physics Letters*, vol. 103, no. 4, p. 042106, 2013.

[65] A. Ramasubramaniam, "Large excitonic effects in monolayers of molybdenum and tungsten dichalcogenides," *Physical Review B - Condensed Matter and Materials Physics*, vol. 86, no. 11, pp. 1–6, 2012.

[66] V. D. S. Ganesan, J. Linghu, C. Zhang, Y. P. Feng, and L. Shen, "Heterostructures of phosphorene and transition metal dichalcogenides for excitonic solar cells: A first-principles study," *Applied Physics Letters*, vol. 108, no. 12, p. 122105, 2016.

[67] C. Ataca and S. Ciraci, "Stable, Sinlger layer MX2 Transistion Metal Oxides and Dichalcogenides," *Physical Chemistry C*, 2012.

[68] W. S. Yun, S. W. Han, S. C. Hong, I. G. Kim, and J. D. Lee, "Thickness and strain effects on electronic structures of transition metal dichalcogenides," *Physical Review B*, vol. 85, no. 3, p. 033305, 2012.

[69] A. Tkatchenko and M. Scheffler, "Accurate molecular van der Waals interactions from ground-state electron density and free-atom reference data," *Physical Review Letters*, vol. 102, no. 7, pp. 6–9, 2009.

[70] J. He, K. Hummer, and C. Franchini, "Stacking effects on the electronic and optical properties of bilayer transition metal dichalcogenides MoS 2, MoSe 2, WS 2, and WSe 2," *Physical Review B - Condensed Matter and Materials Physics*, vol. 89, no. 7, pp. 1–11, 2014.

[71] D. M. Caughey and R. E. Thomas, "Carrier Mobilities in Silicon Empirically Related to Doping and Field," *Proceedings of the IEEE*, vol. 55, no. 12, pp. 2192–2193, 1967.

[72] S. Selberherr, *Analysis and Simulation of Semiconductor Devices.* Springer, New York, 1984.

[73] B. W. H. Baugher, H. O. H. Churchill, Y. Yang, and P. Jarillo-herrero, "Intrinsic Electronic Transport Properties of High Quality Monolayer and Bilayer MoS2," *Nano Letters*, vol. 13, no. 9, p. 130809091841007, 2013.

[74] K. S. Novoselov, D. Jiang, F. Schedin, T. J. Booth, V. V. Khotkevich, S. V. Morozov, and A. K. Geim, "Two-dimensional atomic crystals," *Proceedings of the National Academy of Sciences of the United States of America*, vol. 102, no. 30, pp. 10 451–10 453, 2005.

[75] D. J. Late, B. Liu, H. S. S. R. Matte, V. P. Dravid, and C. N. R. Rao, "Hysteresis in single-layer MoS2 field effect transistors." *ACS Nano*, vol. 6, no. 6, pp. 5635–41, 2012.

[76] S. Das, H.-Y. Y. Chen, A. V. Penumatcha, and J. Appenzeller, "High Performance Multi-layer MoS2 Transistors with Scandium Contacts." *Nano letters*, vol. 13, no. 1, pp. 100–5, 2012.

[77] S. A. Thiele, "Simulation von Transistoren aus zweidimensionalen Materialien jenseits von Graphen," Master's thesis, Technische Universität Ilmenau, 2013.

[78] W. Liu, J. Kang, D. Sarkar, Y. Khatami, D. Jena, and K. Banerjee, “Role of metal contacts in designing high-performance monolayer n-type WSe2 field effect transistors,” *Nano Letters*, vol. 13, no. 5, pp. 1983–1990, 2013.

[79] S. Kim, A. Konar, W.-S. Hwang, J. H. Lee, J. Lee, J. Yang, C. Jung, H. Kim, J.-B. Yoo, J.-Y. Choi, Y. W. Jin, S. Y. Lee, D. Jena, W. Choi, and K. Kim, “High-mobility and low-power thin-film transistors based on multilayer MoS2 crystals.” *Nature communications*, vol. 3, p. 1011, 2012.

[80] S. Chuang, C. Battaglia, A. Azcatl, S. McDonnell, J. S. Kang, X. Yin, M. Tosun, R. Kapadia, H. Fang, R. M. Wallace, and A. Javey, “MoS 2P-type Transistors and Diodes Enabled by High Work Function MoO xContacts,” *Nano Letters*, vol. 14, no. 3, pp. 1337–1342, 2014.

[81] A. Allain, J. Kang, K. Banerjee, and A. Kis, “Electrical contacts to two-dimensional semiconductors,” *Nature Materials*, vol. 14, no. 12, pp. 1195–1205, 2015.

[82] J. Kang, D. Sarkar, W. Liu, D. Jena, and K. Banerjee, “A Computational Study of Metal-Contacts to Beyond-Graphene 2D Semiconductor Materials,” *IEEE International Electron Devices Meeting (IEDM)*, pp. 407–410, 2012.

[83] J. Kang, W. Liu, D. Sarkar, D. Jena, and K. Banerjee, “Computational study of metal contacts to monolayer transition-metal dichalcogenide semiconductors,” *Physical Review X*, vol. 4, no. 3, pp. 1–14, 2014.

[84] J. Kang, W. Liu, and K. Banerjee, “High-performance MoS2 transistors with low-resistance molybdenum contacts,” *Applied Physics Letters*, vol. 104, no. 9, pp. 2–7, 2014.

[85] I. Popov, G. Seifert, and D. Tom??nek, “Designing electrical contacts to MoS 2 Monolayers: A computational study,” *Physical Review Letters*, vol. 108, no. 15, pp. 1–5, 2012.

[86] S. M. Sze and M. K. Lee, *Semiconductor Devices*, 2015, vol. 1.

[87] C. Gong, L. Colombo, R. M. Wallace, and K. Cho, “The Unusual Mechanism of Partial Fermi Level Pinning at Metal-MoS2 Interfaces,” *Nano letters*, vol. 14, pp. 1714–1720, 2014.

[88] N. Kaushik, A. Nipane, F. Basheer, S. Dubey, S. Grover, M. M. Deshmukh, and S. Lodha, “Schottky barrier heights for Au and Pd contacts to MoS2,” *Applied Physics Letters*, vol. 105, no. 11, pp. 1–5, 2014.

[89] C. Maurel, R. Coratger, F. Ajustron, J. Beauvillain, and P. Gerard, “Electrical characteristics of metal/semiconductor nanocontacts using light emission in a scanning tunneling microscope,” *Journal of Applied Physics*, vol. 94, no. 3, pp. 1979–1982, 2003.

[90] C.-H. Lee, G.-h. Lee, A. M. van der Zande, W. Chen, Y. Li, M. Han, X. Cui, G. Arefe, C. Nuckolls, T. F. Heinz, J. Guo, J. Hone, and P. Kim, "Atomically thin p–n junctions with van der Waals heterointerfaces," *Nature Nanotechnology*, vol. 9, no. 9, pp. 676–681, 2014.

[91] V. Podzorov, M. E. Gershenson, C. Kloc, R. Zeis, and E. Bucher, "High-mobility field-effect transistors based on transition metal dichalcogenides," *Applied Physics Letters*, vol. 84, no. 17, pp. 3301–3303, 2004.

[92] H. Liu, M. Si, Y. Deng, A. T. Neal, Y. Du, S. Najmaei, P. M. Ajayan, J. Lou, and P. D. Ye, "Switching mechanism in single-layer molybdenum disulfide transistors: An insight into current flow across Schottky barriers," *ACS Nano*, vol. 8, no. 1, pp. 1031–1038, 2014.

[93] H. Fang, S. Chuang, T. C. Chang, K. Takei, T. Takahashi, and A. Javey, "High-performance single layered WSe 2 p-FETs with chemically doped contacts," *Nano Letters*, vol. 12, no. 7, pp. 3788–3792, 2012.

[94] H. Fang, M. Tosun, G. Seol, T. C. Chang, K. Takei, J. Guo, and A. Javey, "Degenerate n Doping of Few-Layer Transition Metal Dichalcogenides by Potassium," *Nano letters*, vol. 13, pp. 1991–1995, 2013.

[95] M. Amani, M. L. Chin, A. G. Birdwell, T. P. O'Regan, S. Najmaei, Z. Liu, P. M. Ajayan, J. Lou, and M. Dubey, "Electrical performance of monolayer MoS2 field-effect transistors prepared by chemical vapor deposition," *Applied Physics Letters*, vol. 102, no. 19, 2013.

[96] J. Kang, W. Liu, and K. Banerjee, "High-performance MoS2 transistors with low-resistance molybdenum contacts," *Applied Physics Letters*, vol. 104, no. 9, pp. 2–7, 2014.

[97] H. Liu and P. D. Ye, "MoS2 Dual-Gate MOSFET with Atomic-Layer-Deposited Al2O3 as Top-Gate Dielectric," *IEEE Electron Device Letters*, vol. 33, no. 4, pp. 546–548, 2012.

[98] T. Roy, M. Tosun, J. S. Kang, A. B. Sachid, S. B. Desai, M. Hettick, C. C. Hu, and A. Javey, "Field-effect transistors built from all two-dimensional material components," *ACS Nano*, vol. 8, no. 6, pp. 6259–6264, 2014.

[99] S. Larentis, B. Fallahazad, and E. Tutuc, "Field-effect transistors and intrinsic mobility in ultra-thin MoSe 2 layers," *Applied Physics Letters*, vol. 101, no. 22, 2012.

[100] P. M. Lenahan, "What can electron paramagnetic resonance tell us about the Si/SiO2 system?" *Journal of Vacuum Science & Technology B: Microelectronics and Nanometer Structures*, vol. 16, no. 4, p. 2134, 1998.

[101] T. Grasser, W. Goes, Y. Wimmer, F. Schanovsky, G. Rzepa, M. Waltl, K. Rott, H. Reisinger, V. V. Afanas'Ev, A. Stesmans, A. M. El-Sayed, and A. L. Shluger, "On the microscopic structure of hole traps in pMOSFETs," *IEEE International Electron Devices Meeting*, pp. 21.1.1–4, 2014.

[102] T. Grasser, H. Reisinger, P. J. Wagner, and B. Kaczer, "Time-dependent defect spectroscopy for characterization of border traps in metal-oxide-semiconductor transistors," *Physical Review B - Condensed Matter and Materials Physics*, vol. 82, no. 24, pp. 1–10, 2010.

[103] G. Rzepa, "Microscopic Modeling of NBTI in MOS Transistors," Master's thesis, Vienna University of Technology, 2013.

[104] M. J. Uren, M. J. Kirton, and S. Collins, "Anomalous telegraph noise in small-area silicon metal-oxide-semiconductor field-effect transistors," *Physical Review B*, vol. 37, no. 14, pp. 8346–8350, 1988.

[105] T. Grasser, "Stochastic charge trapping in oxides: From random telegraph noise to bias temperature instabilities," *Microelectronics Reliability*, vol. 52, no. 1, pp. 39–70, 2012.

[106] T. Grasser, B. Kaczer, W. Goes, H. Reisinger, T. Aichinger, P. Hehenberger, P.-j. Wagner, F. Schanovsky, J. Franco, M. T. Luque, and M. Nelhiebel, "The Paradigm Shift in Understanding the Bias Temperature Instability : From Reaction – Diffusion to Switching Oxide Traps," *Transactions on Device and Materials Reliability, IEEE*, vol. 58, no. 11, pp. 3652–3666, 2011.

[107] H. Qiu, L. Pan, Z. Yao, J. Li, Y. Shi, and X. Wang, "Electrical characterization of back-gated bi-layer MoS 2 field-effect transistors and the effect of ambient on their performances," *Applied Physics Letters*, vol. 100, no. 12, pp. 2014–2017, 2012.

[108] Y. Guo, X. Wei, J. Shu, B. Liu, J. Yin, C. Guan, Y. Han, S. Gao, and Q. Chen, "Charge trapping at the MoS2-SiO2 interface and its effects on the characteristics of MoS2 metal-oxide-semiconductor field effect transistors," *Applied Physics Letters*, vol. 106, no. 10, 2015.

[109] K. Choi, S. R. A. Raza, H. S. Lee, P. J. Jeon, A. Pezeshki, S.-w. Min, J. S. Kim, W. Yoon, S.-y. Ju, K. Lee, and S. Im, "Trap density probing on top-gate MoS2 nanosheet field-effect transistors by photo-excited charge collection spectroscopy," *Nanoscale*, vol. 7, pp. 5617–5623, 2015.

[110] Y. Park, H. W. Baac, J. Heo, and G. Yoo, "Thermally activated trap charges responsible for hysteresis in multilayer MoS2 field-effect transistors," *Applied Physics Letters*, vol. 108, no. 8, p. 083102, 2016.

[111] J. Shu, G. Wu, Y. Guo, B. Liu, X. Wei, and Q. Chen, "The Intrinsic Origin of the Hysteresis in the MoS2 Field Effect Transistors," *Nanoscale*, pp. 3049–3056, 2016.

[112] Y. Y. Illarionov, G. Rzepa, M. Waltl, T. Knobloch, A. Grill, M. M. Furchi, T. Mueller, and T. Grasser, “The Role of Charge Trapping in MoS 2 / SiO 2 and MoS 2 / hBN Field-Effect Transistors,” *2D Materials*, vol. 3, no. 3, pp. 035 004.1–15, 2016.

[113] D. K. Schroder, “Negative bias temperature instability: What do we understand?” *Microelectronics Reliability*, vol. 47, no. 6, pp. 841–852, 2007.

[114] D. M. Fleetwood, “Border traps’ in MOS devices,” *IEEE transactions on nuclear science*, vol. 39, no. 2, pp. 269–271, 1992.

[115] T. Grasser, T. Aichinger, G. Pobegen, H. Reisinger, P. J. Wagner, J. Franco, M. Nelhiebel, and B. Kaczer, “The ’permanent’ component of NBTI: Composition and annealing,” *IEEE International Reliability Physics Symposium Proceedings*, pp. 605–613, 2011.

[116] B. E. Deal, M. Sklar, a. S. Grove, and E. H. Snow, “Characteristics of the Surface-State Charge (Qss) of Thermally Oxidized Silicon,” *Journal of The Electrochemical Society*, vol. 114, no. d, p. 266, 1967.

[117] K. O. Jeppson and C. M. Svensson, “Negative bias stress of MOS devices at high electric fields and degradation of MNOS devices,” *Journal of Applied Physics*, vol. 48, no. 5, pp. 2004–2014, 1977.

[118] T. Grasser, P.-J. Wagner, P. Hehenberger, W. Goes, and B. Kaczer, “A Rigorous Study of Measurement Techniques for Negative Bias Temperature Instability,” *IEEE Transactions on Device and Materials Reliability*, vol. 8, no. 3, pp. 526–535, 2008.

[119] W. Van Roosbroeck, “Theory of the Flow of Electrons and Holes in Germanium and Other Semiconductors,” *Bell System Technical Journal*, vol. 29, no. 4, pp. 560–607, 1950.

[120] D. L. Scharfetter and H. K. Gummel, “Large-Signal Analysis of a Silicon Read Diode Oscillator,” *IEEE Transactions on Electron Devices*, vol. 16, no. 1, pp. 64–77, 1969.

[121] Global TCAD Solutions, “Minimos-NT Manual,” Vienna, 2015.

[122] M. Lundstrom, “Drift-diffusion and computational electronics - Still going strong after 40 years!” *International Conference on Simulation of Semiconductor Processes and Devices, SISPAD*, vol. 2015-Octob, pp. 1–3, 2015.

[123] M. G. Ancona, “Electron transport in graphene from a diffusion-drift perspective,” *IEEE Transactions on Electron Devices*, vol. 57, no. 3, pp. 681–689, 2010.

[124] D. Jiménez, “Drift-diffusion model for single layer transition metal dichalcogenide field-effect transistors,” *Applied Physics Letters*, vol. 101, no. 24, 2012.

[125] W. Goes, F. Schanovsky, and T. Grasser, "Advanced Modeling of Oxide Defects," in *Bias Temperature Instability for Devices and Circuits*. Springer, New York, 2013, vol. 1, pp. 457–484.

[126] A. Neugroschel, C. T. Sah, K. M. Han, M. S. Carroll, T. Nishida, J. T. Kavalieros, and Y. Lu, "Direct-current measurements of oxide and interface traps on oxidized silicon," *IEEE Transactions on Electron Devices*, vol. 42, no. 9, pp. 1657–1662, 1995.

[127] W. Shockley and W. T. Read, "Statistics of the Recombination of Holes and Electrons," *Physical Review*, vol. 87, no. 46, pp. 835–842, 1952.

[128] G. Rzepa, M. Waltl, W. Goes, B. Kaczer, J. Franco, T. Chiarella, N. Horiguchi, and T. Grasser, "Complete Extraction of Defect Bands Responsible for Instabilities in n and pFinFETs," *2016 Symposium on VLSI Technology Digest of Technical Papers*, pp. 208–209, 2016.

[129] P. Morse, "Diatomic Molecules According to the Wave Mechanics. II. Vibrational Levels," *Physical Review*, vol. 34, no. 1, pp. 57–64, 1929.

[130] L. A. Girifalco and V. G. Weizer, "Application of the morse potential function to cubic metals," *Physical Review*, vol. 114, no. 3, pp. 687–690, 1959.

[131] R. W. Keyes, "Bonding and antibonding potentials in group-IV semiconductors," *Physical Review Letters*, vol. 34, no. 21, pp. 1334–1337, 1975.

[132] I. Mata, E. Molins, I. Alkorta, and E. Espinosa, "Effect of an external electric field on the dissociation energy and the electron density properties: The case of the hydrogen bonded dimer HF-HF," *Journal of Chemical Physics*, vol. 130, no. 4, pp. 0–16, 2009.

[133] J. A. Dean, *Lange's Handbook of Chemistry*, 15th ed. McGraw-Hill,Inc, 1999.

[134] A. C. T. van Duin, A. Strachan, S. Stewman, Q. Zhang, X. Xu, and W. A. Goddard, "ReaxFFSiO Reactive Force Field for Silicon and Silicon Oxide Systems," *J. Phys. Chem. A*, vol. 107, no. 19, pp. 3803–3811, 2003.

[135] A. Asenov, R. Balasubramaniam, A. R. Brown, and J. H. Davies, "RTS amplitudes in decananometer MOSFETs: 3-D simulation study," *IEEE Transactions on Electron Devices*, vol. 50, no. 3, pp. 839–845, 2003.

[136] B. Kaczer, P. J. Roussel, T. Grasser, and G. Groeseneken, "Statistics of multiple trapped charges in the gate oxide of deeply scaled MOSFET devicesapplication to NBTI," *IEEE Electron Device Letters*, vol. 31, no. 5, pp. 411–413, 2010.

[137] B. B. Machta, R. Chachra, M. K. Transtrum, and J. P. Sethna, "Parameter Space Compression Underlies Emergent Theories and Predictive Models," *Science*, vol. 4878, no. November, pp. 3192–3195, 2013.

[138] P. J. Mohr, B. N. Taylor, and D. B. Newell, "CODATA Recommended Values of the Fundamental Physical Constants - 2006," *Journal of Physical and Chemical Reference Data*, vol. 37.3, no. July, pp. 1–6, 2008.

[139] H. Helgeson, "Summary and critique of the thermodynamic properties of rock-forming minerals," *American Journal of Science*, vol. 278, pp. 1–229, 1978.

[140] K. Terada, K. Nishiyama, and K. ichi Hatanaka, "Comparison of MOSFET-threshold-voltage extraction methods," *Solid-State Electronics*, vol. 45, no. 1, pp. 35–40, 2001.

[141] H. Lee, S. Oh, and G. Fuller, "A simple and accurate method to measure the threshold voltage of an enhancement mode MOSFET," *IEEE Transactions on Electron Devices*, vol. 29, no. 2, pp. 346–348, 1982.

[142] A. T. Hanbicki, M. Currie, G. Kioseoglou, A. L. Friedman, and B. T. Jonker, "Measurement of high exciton binding energy in the monolayer transition-metal dichalcogenides WS2 and WSe2," *Solid State Communications*, vol. 203, pp. 16–20, 2015.

[143] B. Zhu, X. Chen, and X. Cui, "Exciton Binding Energy of Monolayer WS2," *Scientific Reports*, vol. 5, p. 9218, 2015.

[144] Z. Ye, T. Cao, K. O'Brien, H. Zhu, X. Yin, Y. Wang, S. G. Louie, and X. Zhang, "Probing Excitonic Dark States in Single-layer Tungsten Disulfide," *Nature*, vol. 513, no. 7517, pp. 214–218, 2014.

[145] C. Zhang, Y. Chen, J.-K. Huang, X. Wu, L.-J. Li, W. Yao, J. Tersoff, and C.-K. Shih, "Visualizing Band Offsets and Edge States in Bilayer-Monolayer Transition Metal Dichalcogenides Lateral Heterojunction," *Nature Communications*, vol. 6, pp. 1–6, 2016.

[146] K. He, N. Kumar, L. Zhao, Z. Wang, K. F. Mak, H. Zhao, and J. Shan, "Tightly bound excitons in monolayer WSe2," *Physical Review Letters*, vol. 113, no. 2, pp. 1–5, 2014.

[147] S. Larentis, J. R. Tolsma, B. Fallahazad, D. C. Dillen, K. Kim, A. H. Macdonald, and E. Tutuc, "Band offset and negative compressibility in graphene-MoS2 heterostructures," *Nano Letters*, vol. 14, no. 4, pp. 2039–2045, 2014.

[148] V. V. Afanas'ev, D. Chiappe, C. Huyghebaert, I. Radu, S. D. Gendt, M. Houssa, and A. Stesmans, "Band alignment at interfaces of few-monolayer MoS 2 with SiO 2 and HfO 2," *Microelectronic Engineering*, vol. 147, pp. 294–297, 2015.

Hiermit erkläre ich, dass die vorliegende Arbeit gemäß dem Code of Conduct – Regeln zur Sicherung guter wissenschaftlicher Praxis (in der aktuellen Fassung des jeweiligen Mitteilungsblattes der TU Wien), insbesondere ohne unzulässige Hilfe Dritter und ohne Benutzung anderer als der angegebenen Hilfsmittel, angefertigt wurde. Die aus anderen Quellen direkt oder indirekt übernommenen Daten und Konzepte sind unter Angabe der Quelle gekennzeichnet. Die Arbeit wurde bisher weder im In– noch im Ausland in gleicher oder in ähnlicher Form in anderen Prüfungsverfahren vorgelegt.

Wien, Okotber 2016

Theresia Knobloch